
Chapter 3 Shielding of Proton and Ion Accelerators

In this chapter the major considerations pertinent to the shielding of proton and ion accelerators is addressed. Particular emphasis is placed on the shielding of neutrons in view of their general dominance of the radiation fields. The shielding of muons at such accelerators is also described. A short review of the various Monte-Carlo programs commonly used in shielding calculations at proton and ion accelerators is presented. The properties of various shielding materials commonly used at accelerators are reviewed. The chapter concludes with a discussion of various features of neutron energy spectra found at proton accelerators.

I. Hadron (Neutron) Shielding for Low Energy Incident Protons

For this discussion, the "low energy" region extends up to approximately $E_0 = 100$ MeV. The basic treatment follows that of (Pa73).

$E_0 \leq 15$ MeV:

This region is especially complex because it is the region of significant nuclear structure effects including:

the resonances associated with the phenomena known as "compound nuclei" and

the presence of a large number of nuclear excited states up to 20 MeV excitation energy having a wide variety of nuclear structure quantum numbers and very narrow widths in energy.

The method most commonly used to calculate shielding thicknesses is that of **removal cross section theory**.

According to F. Clark (Cl71) there are three principles involved here:

- A. "The shield must be sufficiently thick and the neutrons so distributed in energy that only a narrow band of the most penetrating source neutrons give any appreciable ultimate contribution to the dose outside the shield."
- B. "There must be sufficient hydrogen in the shield, intimately mixed or in the final shield region, to assure a very short characteristic transport length from about 1 MeV to absorption at or near thermal energy."
- C. "The source energy distribution and shield material (nonhydrogeneous) properties must be such as to assure a short transport distance for slowing down from the most penetrating energies to 1 MeV."

It has been found that the transmission of dose equivalent, $H(t)$, as a function of shield thickness, t , is approximately given for these neutrons by

$$H(t) = \Phi_0 P G e^{-\Sigma_r t}, \quad (3.1)$$

where Φ_0 is the fluence before the shielding (calculated from neutron yield information), P is the fluence to dose equivalent conversion factor (where one may need to integrate over spectrum to get a true "average" value), G is a "geometry factor", t (cm) is the thickness. For parallel beams, $G = 1$ while for an isotropic point source, $G = 1/(4\pi r^2)$. Σ_r is the **macroscopic removal cross section**:

Chapter 3 Shielding of Proton and Ion Accelerators

$$\Sigma_r = \frac{0.602 \sigma_r \rho}{A} \text{ cm}^{-1}, \quad (3.2)$$

where σ_r = microscopic removal cross section in barns

ρ = density (g/cm³)

ρ = density (g/cm³)

A = mass number.

$$\text{For mixtures of } n \text{ materials, } \Sigma_r = \sum_{i=1}^n \left(\frac{\Sigma_{ri}}{\rho} \right) \rho_i \quad (3.3)$$

where ρ_i is the partial density of the i^{th} material. (In this formulation the overall density is equal to the sum of the partial densities.)

For $A > 8$,

$$\sigma_r \approx 0.21 A^{-0.58} \text{ barns} \quad (3.4)$$

for neutrons of approximately 8 MeV. Figure 3.1 taken from (Pa73) gives measured values of Σ_r for various compounds (in units of cm²/g, with the density factor removed).

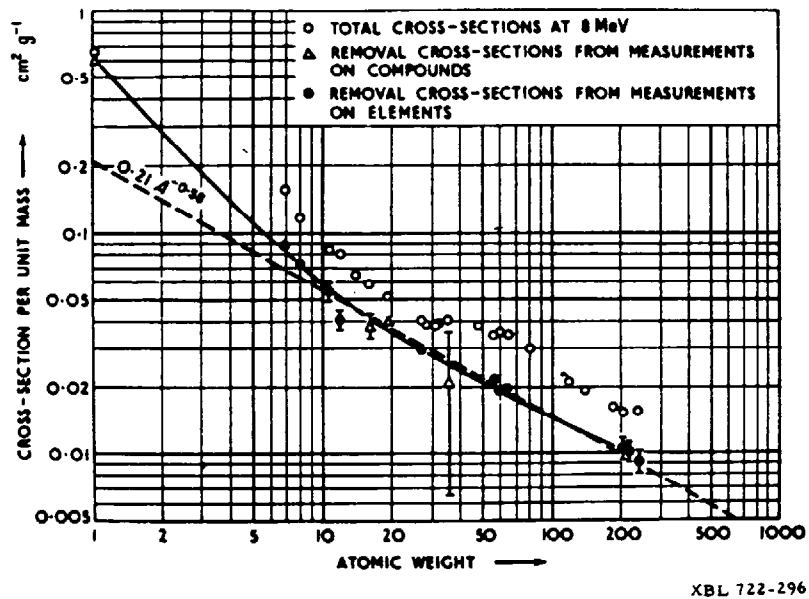


Fig. 3.1 Removal cross sections per unit atomic mass for fission neutrons as a function of mass number. Over the range $8 \leq A \leq 240$, the values are well fit by Eq. (3.4). [Reproduced from (Pa73) and references cited therein].

Table 3.1 taken from (Pa73) gives representative values for σ_r for some energies where this approach is applicable.

Table 3.1 Removal cross-section data, σ_{rem} (barns) for low energy neutrons. The typical accuracy is quoted to be $\pm 5\%$. [Reproduced from (Pa73) and references cited therein.]

Element	1 MeV	Fission spectrum	2.9 MeV	4 MeV	6.7 MeV	14.9 MeV
Carbon		0.90	1.58	1.05	0.83	0.50
Aluminum		1.31				
Iron	1.1	1.96	1.94	1.98	2.26	1.60
Copper		2.04				
Lead		3.28	3.70	3.44	3.77	2.95

The removal cross sections work rather well despite the fact that as more shielding is penetrated, neutrons of lower energy tend to dominate the spectrum over those in the few MeV region.

II. Limiting Attenuation at High Energy

This is perhaps the most important feature of neutron shielding at accelerators. As a function of energy, the neutron inelastic cross sections increase rapidly until about 25 MeV where they level off and then fall rapidly with energy in the region $25 < E_n < 100$ MeV to a value which becomes flat with energy. This fact was first noticed by Lindenbaum (Li61).

This fact makes high energy neutron beams attenuate approximately exponentially with an attenuation length, λ_{atten} , which is not very sensitive to energy.

Thus, in units of length,

$$\lambda_{\text{atten}} = \frac{1}{N\sigma_{\text{in}}} \quad (3.5)$$

where σ_{in} is the inelastic cross section (roughly equivalent to the so-called "absorption cross section", often denoted σ_a). This cross section specifically does not include elastic scattering and so is always smaller than the total cross section. N is the number of atoms of the absorbing material per unit volume determined as in Chapter 1 in association with Eq. (1.6). In a "simple-minded" approach, this cross section can be taken to be geometric and the nucleon radius is taken to be 1.2×10^{-13} cm. It then follows that one can multiply by the density to get:

$$\rho\lambda_{\text{atten}} = 38A^{1/3} \quad (\text{g/cm}^2). \quad (3.6)$$

Fig. 3.2 taken from (Pa73) illustrates the neutron inelastic cross sections for several materials up to a kinetic energy of 1.4 GeV.

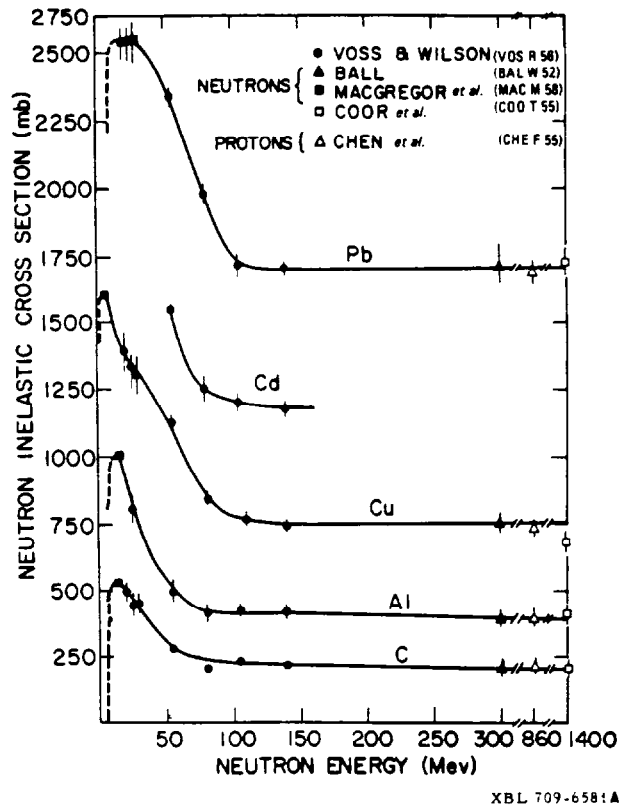


Fig. 3.2 Inelastic neutron cross sections as a function of energy in the range 0 to 1.4 GeV. [Reproduced from (Pa73) as adapted from (Li61).]

Results stated in (Pa73) are well represented by

$$\sigma_{in} = 43A^{0.69} \quad (\text{mb}), \quad (3.7)$$

which was initially verified by cosmic ray results.

The **interaction length**, λ_{inel} (g/cm^2), is thus given by:

$$\lambda_{inel} = \rho/N\sigma_{in} = 38.5 A^{0.31}(\text{g}/\text{cm}^2) \quad (3.8)$$

The geometric approximation was thus not inaccurate!

Figure 3.3 taken from (Pa73) shows the results for absorption cross sections.

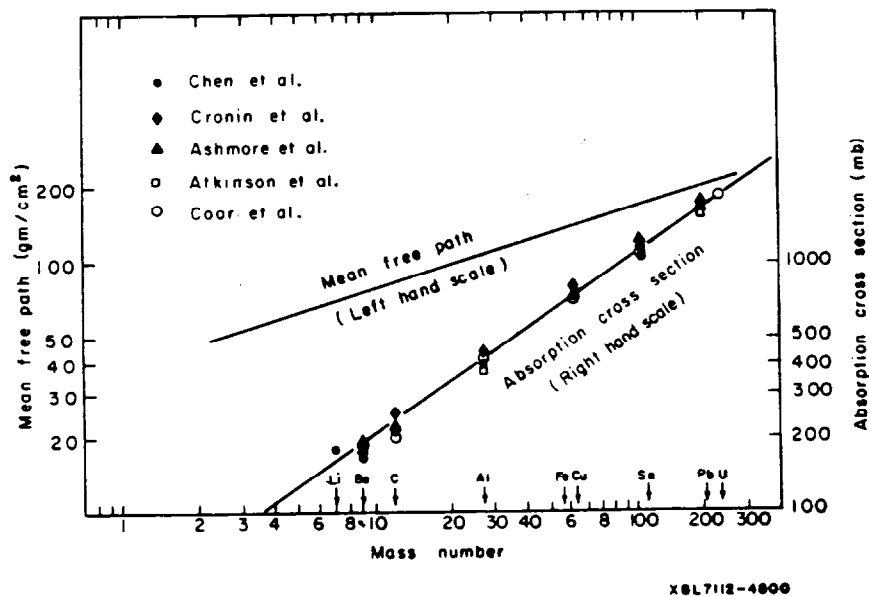


Fig. 3.3 Mean free path and atomic cross section as a function of mass number.
[Reproduced from (Pa73) and references cited therein.]

In general, the ratio of elastic cross section, σ_{el} to absorption (inelastic) cross section, σ_{in} , (σ_{el}/σ_{in}) approximates a value of 0.57. Thus the attenuation length appropriate for the total cross section σ_{tot} can be obtained by dividing the values of λ_{in} by 1.57. Reference (Sc90) has extensive tabulations of the value of σ_{in} (mb) for a variety of particles, energies, and materials in the high energy region as function of particle momenta up to 10 TeV/c.

The saturation of attenuation length for concrete as function of neutron energy is especially important. Figures 3.4 and 3.5 taken from (Th88) gives the results for both neutrons (Fig. 3.4) and protons (Fig. 3.5). An important feature of these results is the equivalence of the attenuation lengths for protons and neutrons at high energies.

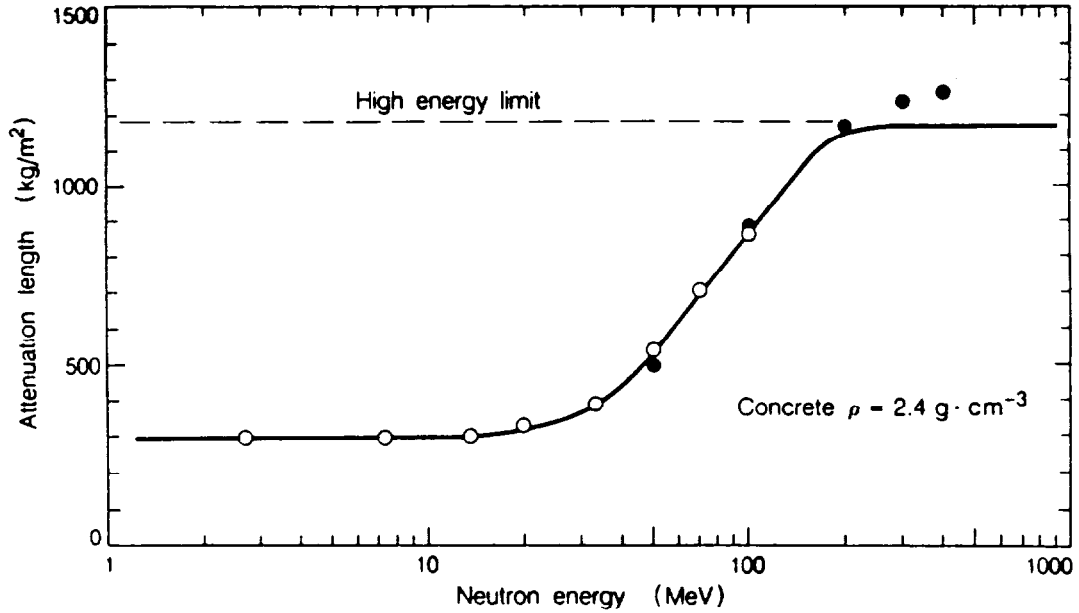


Fig. 3.4 The variation of the attenuation length λ for monoenergetic neutrons in concrete as a function of neutron energy. The solid line shows recommended values of λ and the dashed line shows the high energy limiting value of 1170 kg m^{-2} . [Reproduced from (Th88). The symbols on the figure are the results of calculations referred to in (Th88).]

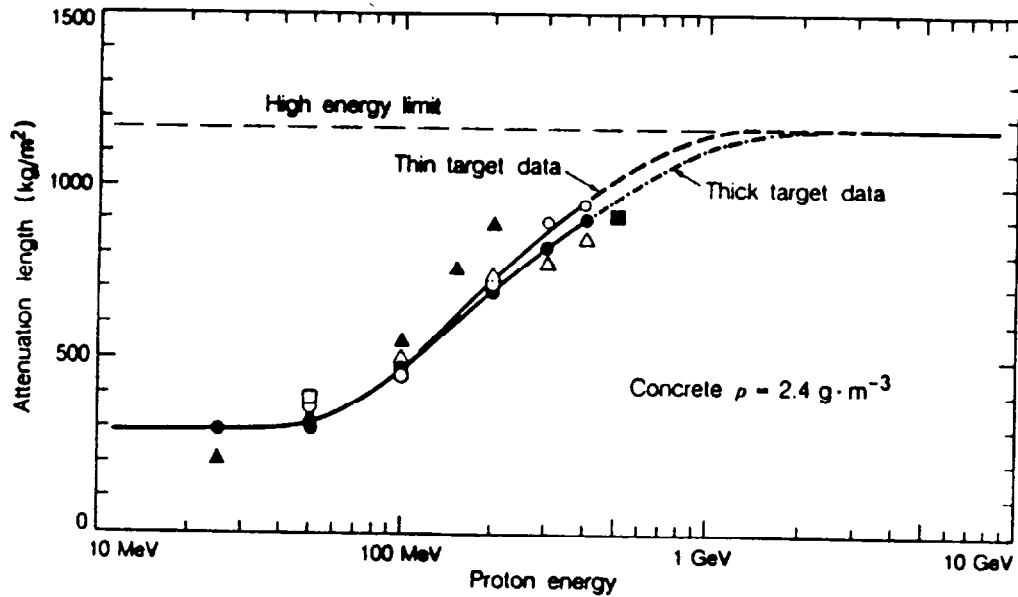


Fig. 3.5 Effective attenuation length λ in concrete as a function of proton energy. [Reproduced from (Th88). The symbols on the figure are the results of calculations referred to in (Th88).]

III. Intermediate and High Energy Shielding-the Hadronic Cascade

The hadronic cascade from a conceptual standpoint

The cascade is initiated at proton accelerators when the beam interacts with components to produce neutrons and other particles. It can also arise at electron accelerators since, as described in Chapters 1 and 2, high energy secondary hadrons are produced in such circumstances.

The collision of a high energy nucleon with a nucleus produces a large number of particles; pions, kaons, and other nucleons (production of "rare" particles other than these are seldom of importance with respect to shielding calculations) as well as fragments of the struck nucleus. Above 1 GeV and at forward angles, the pions, protons, and neutrons, can be nearly equal in number [see (Th88)]. The neutrons may be classified as either evaporation neutrons or cascade neutrons. Evaporation neutrons originate as decays from excited states of residual nuclei and average a few MeV in energy. These neutrons tend to be isotropically distributed. Cascade neutrons are emitted by direct impact and their spectrum extends in energy up to the incident energy with diminishing probability following a spectrum roughly characterized as " $1/E$ ".

As the proton kinetic energy increases, other particles, notably π^\pm and K^\pm , play roles in the cascade when their production becomes energetically possible. They are absorbed with absorption lengths comparable in magnitude to, but not identical with those of protons. These particles also decay into muons. Because of their long ionization ranges and lack of nuclear interactions, muons provide a pathway for energy to escape the cascade.

Nucleons with $E_0 > 150$ MeV propagate the cascade. This is clear from the attenuation length information as summarized in Fig. 3.2. Nucleons in the range $20 < E_n < 150$ MeV also transfer their energy predominantly by nuclear interactions but their energy gets distributed over many particles of all types energetically possible. The ones that are charged particles are ranged-out very quickly. The role played by the energy of approximately 150 MeV for hadronic cascades is similar in kind to that played by the critical energy for electromagnetic ones.

Neutral pions (π^0) are produced when the kinetic energy of the incident proton significantly exceeds the pion rest energy. The π^0 rest energy is 134.9 MeV, its meanlife $\tau = (8.4 \pm 0.6) \times 10^{-17}$ s and $c\tau = 25.2$ nm. The principal decay (99 % branching ratio) is into two γ -rays. An energetic π^0 thus "appears" as two forward-peaked photons each with half of the π^0 's total energy. The decay photons from π^0 decay readily initiate electromagnetic cascades along with the hadronic one. It is possible for the electromagnetic channel to feed back into the hadronic cascade because it too produces high energy hadrons. However this effect is generally of little importance and, for most shielding calculations, the electromagnetic component of a hadronic cascade can be ignored. The exceptions principally involve energy deposition calculations at forward angles (small values of θ). In fact, at hundreds of GeV, electromagnetic cascades dominate the energy deposition at forward angles. This feature can have important ramifications if one needs to consider radiation damage to equipment and the heat load on cryogenic systems.

In general, the neutrons are the principal drivers of the cascade because of the ionization energy loss for pions and for protons below 450 MeV where the ionization range becomes roughly equal to the interaction length. Also, any magnetic fields that are present which can deflect and disperse the charged particles present will not, of course, affect the neutrons. Furthermore, neutrons can be produced at large values of θ compared with the forward-peaked pions.

Chapter 3 Shielding of Proton and Ion Accelerators

These phenomena, in general, apply also to ions heavier than the proton with suitable corrections (especially at low energies) for nuclear structure effects. Scaling of proton results for heavier ions will, in general, roughly be according to the specific energy (MeV/amu).

Figure 3.6 taken from (Pa73) is a schematic flow chart of the hadronic cascade process.

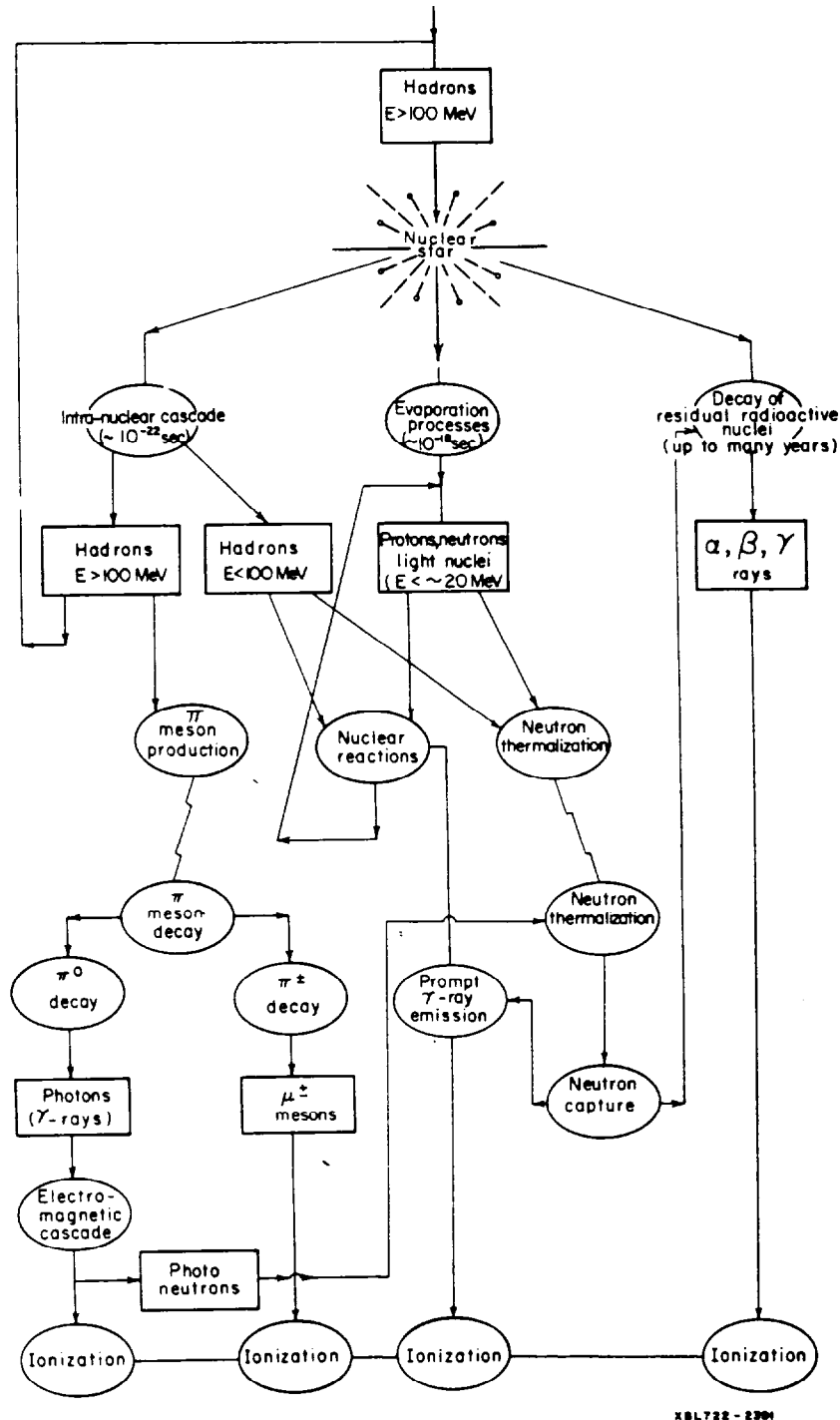


Fig. 3.6 Schematic representation of the development of the nuclear cascade. [Reproduced from (Pa73).]

A simple one-dimensional cascade model

Thomas and Stevenson (Th88) reviewed the simple one-dimensional model of a cascade by Lindenbaum (Li61)) which gives instructive results and supplies some "intuition" into the nature of the hadronic cascade. Figure 3.7 taken from (Th88) defines the geometry.

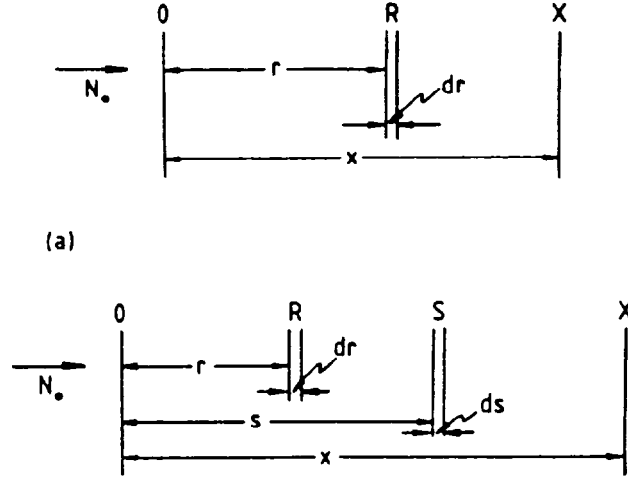


Fig. 3.7 a) Single collision geometry for Lindenbaum approximation. b) Two collision geometry for Lindenbaum approximation. [Reproduced from (Th88).]

Suppose one initially has N_0 incident high energy nucleons. After an individual collision, one of them continues in its original direction at a reduced energy but with the same attenuation length, λ , (approximately true at high energies due to the limiting effect discussed previously)

or

will generate one or more secondary particles also with the same λ , until it has undergone a number of collisions, n , to be degraded to $E \approx 150$ MeV (below which energy the inelastic cross sections greatly increase). At this point it is said to be removed from the cascade.

For simplicity, assume that n is an integer (in reality it has a statistical distribution).

Thus, referring to the figure, the number, v_1 that reach $x = z$ having made no collisions is

$$v_1 = N_0 \exp(-z/\lambda). \quad (3.9)$$

Suppose that there is one collision between 0 and z . The number that reach z is given by the product of the number that reach elemental coordinate dr multiplied by the probability of subsequently reaching z , times the probability of interacting in dr (dr/λ), times the multiplicity, m_1 , in the first interaction. Integrating over dr :

$$\int_0^z [N_0 \exp(-r/\lambda)] [\exp(-(z-r)/\lambda)] \left[m_1 \frac{dr}{\lambda} \right] = (N_0 m_1 \frac{z}{\lambda}) \exp(-z/\lambda) = v_2. \quad (3.10)$$

Now suppose there are two collisions. The number that reach z is the product of those that reach s having made one collision, multiplied by the probability of subsequently reaching z , times the multiplicity in the second interaction m_2 , times the probability of interacting in ds :

$$\int_0^z \left[N_0 m_1 \frac{s}{\lambda} \exp(-s/\lambda) \right] \left[\exp[-(z-s)/\lambda] \right] \left[m_2 \frac{ds}{\lambda} \right]$$

$$= (N_0 m_1 m_2 \frac{1}{\lambda^2}) \exp(-z/\lambda) \int_0^z s ds = (N_0 m_1 m_2 \frac{z^2}{2\lambda^2}) \exp(-z/\lambda) = v_3 \quad (3.11)$$

Therefore, with n defined as above, one can write:

$$N_n(x) = N_0 \beta_n(z/\lambda) \exp(-z/\lambda) \quad (3.12)$$

where β is a "buildup" factor,

$$\text{for } n = 1 \quad N_1 = v_1 \quad \beta_1 = 1$$

$$\text{for } n = 2 \quad N_2 = v_1 + v_2 \quad \beta_2 = 1 + (m_1 z/\lambda)$$

$$\text{for } n = 3 \quad N_3 = v_1 + v_2 + v_3 \quad \beta_3 = 1 + (m_1 z/\lambda) + (m_1 m_2 z^2 / 2\lambda^2).$$

Thus this buildup factor is a monotonically increasing function of z .

If $m_1 = m_2 = \dots = m$ (i.e., the assumption that the multiplicity stays the same for all interactions in this simple model) and $mz/\lambda \gg n$, the absorption is approximately exponential with a mean free path, λ_{cas} , given by:

$$\lambda_{cas} = \lambda + \Delta\lambda, \quad \Delta\lambda = n\lambda/mz. \quad (3.13)$$

This correction becomes small as mz/λ increases, so that the true λ_{cas} is not attained until large depths are reached. Figure 3.8 taken from (Th88) plots the number of particles after three generations as a function of x/λ ($m = 2$ and $n = 3$). For this condition, the exponential region is not achieved until $z/\lambda \approx 10$. In concrete, this represents a depth of $\approx 1200 \text{ g/cm}^2$. Figure 3.9, also taken from (Th88), compares a measurement and Monte-Carlo calculation which are in remarkably good agreement with a simple one-dimensional model similar to this one for a particular special case.

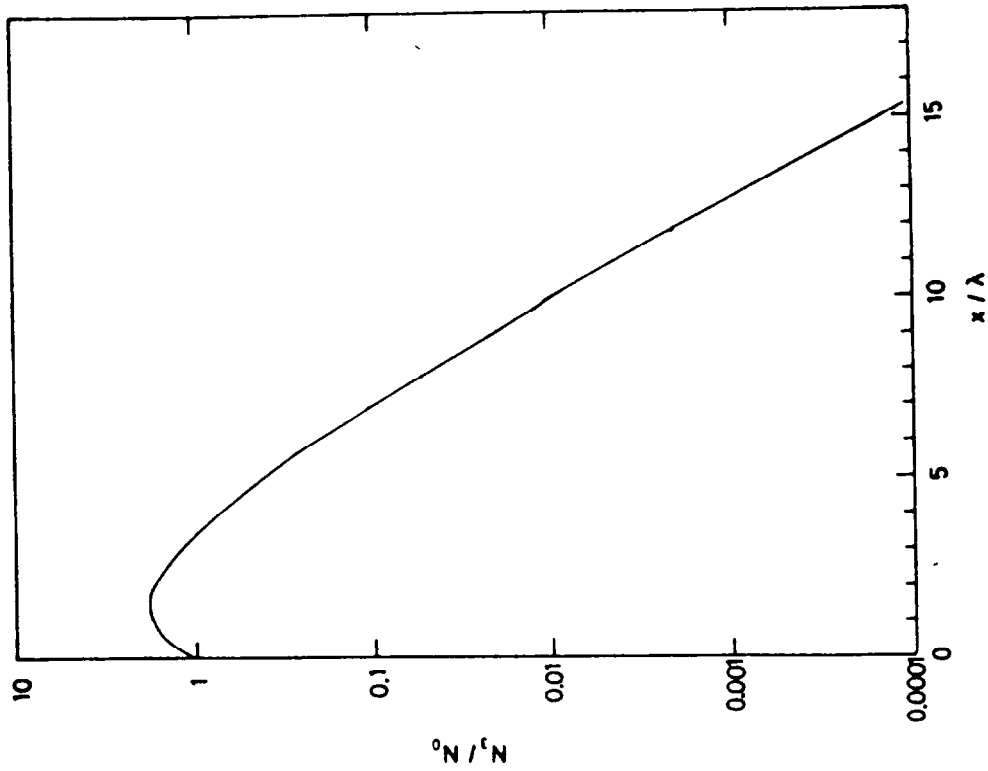


Fig. 3.9 The laterally integrated star density in nuclear emulsions produced by a 19.2 GeV/c proton beam incident on an iron slab as a function of depth in the slab. The Monte-Carlo calculations of Ranft are compared with measurements of Citron and an approximation of Passow. [Reproduced from (Th88 and references cited therein.)]

Fig. 3.8

Development of a one-dimensional cascade in the Lindenbaum approximation with $n = 3$ and $m = 2$. [Reproduced from (Th88).]

Such analytical approaches are constructive qualitatively but have severe limitations, among which are:

- restriction to one dimension
- neglect of ionization energy losses
- neglect of elastic and multiple Coulomb scattering
- assumption that all secondary particles go forward
- assumption that multiplicities are not dependent on energy and particle type
- assumption that λ is a constant for all particles at all energies
- neglect of radiative effects
- neglect of escape of energy into the muon and electromagnetic cascade channels

THUS IT IS CLEAR THAT BETTER METHODS ARE NEEDED!

Semiempirical methods: The Moyer model for point source

References (Pa73), (IC78), (Sc90), (Ro76), (St82), (Th84), (McC87), (Te83), (Te85), (McC85), (Co82), and (Co85) all bear on the development of this model which is based, predominantly, on an exponential approximation with constants fitted to actual data spanning the range of proton beam energies from 7.4 to 800 GeV. The summary of this method here is largely taken from (Pa73) and (Sc90). It is called the "Moyer Model" in honor of the late Burton J. Moyer who developed it at LBL to solve particular shielding problems predating the development of large, fast computers and advanced Monte-Carlo techniques.

The starting point is Fig. 3.10 taken from (Pa73) which describes a "point" target:

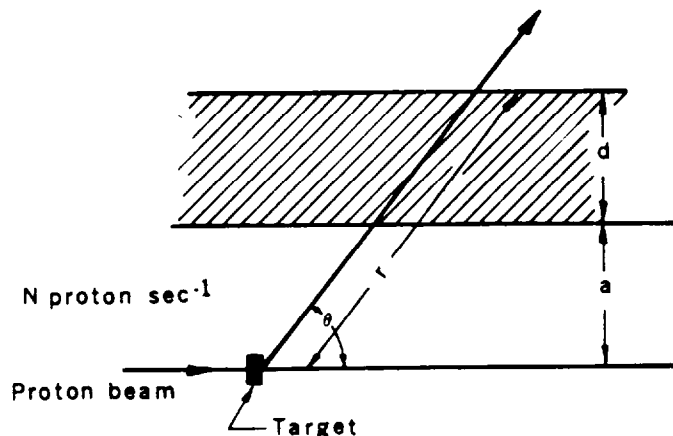


Fig. 3.10 Target and shielding geometry which defines quantities used in the point source Moyer model.

The Moyer model for a point source is developed as follows. The number of neutrons, dN/dE which are emitted into a given element of solid angle $d\Omega$ at angle θ relative to a target struck by N_p protons/sec in an energy interval $E + dE$ is given by:

$$\frac{dN}{dE} = N_p \left(\frac{d^2Y}{dEd\Omega} \right) d\Omega B(E) \exp \left[\frac{-d \csc(\theta)}{\lambda(E)} \right] \quad (3.14)$$

where $B(E)$ is a "buildup factor" and the exponential attenuates the radiation field as it passes through the shield thickness, d , at the "slant angle", θ . The role of the double differential of the yield is obvious. In the above, the flux density at distance r can be obtained by including the factor:

$$\frac{d\Omega}{dA} = \frac{1}{r^2} = \frac{1}{(a+d)^2 \csc^2(\theta)}. \quad (3.15)$$

The integral flux density, ϕ , at the point where the ray emerges from the shield is given by

$$\phi = \frac{1}{r^2} \int_{E_{\min}}^{E_{\max}} dE N_p \left(\frac{d^2Y}{dEd\Omega} \right) B(E) \exp \left[\frac{-d \csc(\theta)}{\lambda(E)} \right]. \quad (3.16)$$

Moyer introduced the following simplifying assumptions for this model. They are as follows:

- A. $\lambda(E) = \lambda = \text{constant}$ for $E \geq 150 \text{ MeV}$ and $\lambda(E) = 0$ for $E < 150 \text{ MeV}$. This is a simplified rendering of the leveling-off of the inelastic cross section at high energy.

$$\phi(E_n > 150 \text{ MeV}) = N_p \frac{1}{r^2} \exp \left[\frac{-d \csc(\theta)}{\lambda} \right] \int_{150 \text{ MeV}}^{E_{\max}} dE \left(\frac{d^2Y}{dEd\Omega} \right) B(E). \quad (3.17)$$

- B. The neutrons emitted at angle θ can be represented by a simple function $f(\theta)$ multiplied by a multiplicity factor $M(E_{\max})$ that depends only on the incident energy, thus:

$$\phi(E_n > 150 \text{ MeV}) = N_p \frac{1}{r^2} \exp \left[\frac{-d \csc(\theta)}{\lambda} \right] M(E_{\max}) f(\theta) = N_p \frac{1}{r^2} \exp \left[\frac{-d \csc(\theta)}{\lambda} \right] g(E_{\max}, \theta) \quad (3.18)$$

where $g(E_{\max}, \theta)$ is an angular distribution function constant for given E_{\max} and given target.

- C. The fluence to dose equivalent conversion factor for neutrons with energy $> 150 \text{ MeV}$, P_{150} , is not strongly dependent on energy (see Fig. 1.6). Thus the dose equivalent just outside of the shield due to neutrons $> 150 \text{ MeV}$ is given by:

$$H(E_n > 150 \text{ MeV}) = P_{150} \phi(E_n > 150 \text{ MeV}).$$

The total dose equivalent, H , then is given by

$$H = kH(E_n > 150 \text{ MeV}) \text{ where } k \geq 1. \quad (3.19)$$

This implicitly assumes that the low-energy neutrons are in equilibrium with those > 150 MeV so that the spectrum no longer changes with depth. This is a valid assumption for a shield more than a few mean free paths thick.

Thus, Moyer's assumptions lead to:

$$H = \frac{kP_{150}N_p g(E_{\max}, \theta)}{(a + d)^2 \csc^2(\theta)} \exp\left[\frac{-d \csc(\theta)}{\lambda}\right]. \quad (3.20)$$

(Sc90) has generalized the results for the geometry shown in Fig. 3.11 t with multiple materials in the shield.

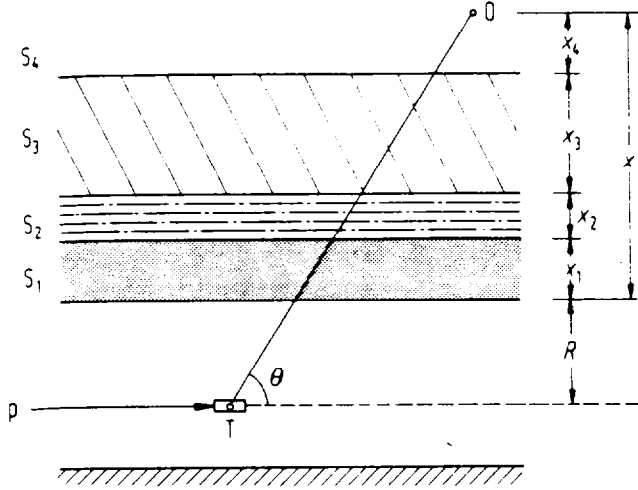


Fig. 3.11 Sketch of the geometry for the empirical Moyer Model. The proton beam, p , impinges on the target, T . The shield materials S_1 - S_4 could be, for example, iron, concrete, earth and air respectively. R is the internal radius of the tunnel, assumed to offer no attenuation. The observer O is situated at a radial thickness of x equal to the sum of x_1 to x_4 . [Reproduced from (Sc90).]

The parameter ζ is introduced to take care of the multiple (n) shielding components:

$$\zeta = \sum_{i=1}^n \frac{x_i}{\lambda_i} \quad (3.21)$$

where the sum is over the i layers of shielding.

Recent work, notably (St82) and (Th84), has determined that the data indicate that $f(\theta)$ is given by:

$$f(\theta) = \exp(-\beta\theta), \quad (3.22)$$

and that, in fact, $\beta \approx 2.3 \text{ rad}^{-1}$ (for $E_n > 150 \text{ MeV}$).

Thus;

$$H = \frac{H_0(E_p) \exp(-\beta\theta) \exp\{-\zeta \csc(\theta)\}}{(r \csc(\theta))^2} \quad (3.23)$$

in which $r = R + \sum_{i=1}^n x_i$ and

where $H_0(E_p)\exp(-\beta\theta)$ is determined from the yield data and empirical measurements.¹ $H_0(E_p)$ is best fit as a power law; $H_0(E_p) = kE^n$. From such results (per incident proton):

$$\begin{aligned} H_0(E_p) &= [(2.84 \pm 0.14) \times 10^{-13}] E_p^{(0.80 \pm 0.10)} \text{ Sv m}^2, \\ &= 2.84 \times 10^{-8} E_p^{0.8} \text{ mrem m}^2 = 2.8 \times 10^{-4} E_p^{0.8} \text{ mrem cm}^2 \end{aligned} \quad (3.24)$$

with E_p in GeV (per proton). These results are derived for relatively "thick" targets (like accelerator magnets) in tunnel geometries. (Sc90), based on Monte-Carlo results gives values for "thin" targets of $k = 2.0 \times 10^{-13}$ (Sv) and $n = 0.5$. A beam pipe would be an example of a "thin" target. The differences thus reflect buildup in the shower. For thick lateral shields close to the beam where the cascade immediately becomes fully developed, $k = (6.9 \pm 0.1) \times 10^{-15}$ (Sv) independent of target material [(Sc90) and (St87)].

Similarly, recommended values of λ are;

$$\begin{aligned} \text{concrete:} \quad & 1170 \pm 20 \text{ kg/m}^2 = 117 \text{ g/cm}^2 \\ \text{others:} \quad & 428A^{1/3} \text{ kg/m}^2 = 42.8A^{1/3} \text{ g/cm}^2. \end{aligned}$$

These values are 15-30% larger than the "nuclear interaction lengths" and are reflective of the shower phenomena discussed above.

If one sets the partial derivative $\frac{\partial H}{\partial \theta} = \text{zero}$, one can derive the following equation for

determining the value of $\theta = \theta'$ at which the maximum dose equivalent occurs. Generally this equation can be solved by successive approximation methods.

$$\zeta \cos \theta' - \beta \sin^2(\theta') + 2 \cos(\theta') \sin(\theta') = 0. \quad (3.25)$$

One can substitute into the above equation to get the maximum dose equivalent at a given radial depth. According to (McC87), over a wide range of values of ζ , the following holds:

$$H_{\max} = 1.66 \times 10^{-14} E_p^{0.8} \exp(-\zeta) \frac{\zeta^{0.245}}{r^2} \text{ Sv (r in m) (per proton)}. \quad (3.26)$$

¹In this equation, the symbol r denotes the distance from the beam axis to the location of interest along a line perpendicular to the beam axis while in Fig. 3.10, the symbol r denotes the actual distance from the point of interaction to the location of concern.

For values of $\zeta > 2$, the following is equally accurate:

$$H_{\max} = 1.26 \times 10^{-14} E_p^{0.8} \frac{\exp(-1.023\zeta)}{r^2} \text{ Sv (r in m) (per proton).} \quad (3.27)$$

The Moyer Model for line sources

Assume a uniform source of one proton interacting per unit length. Then, the dose equivalent from the individual increments along the line source contribute to the total at any given point, P, external to the shield. Fig. 3.12 shows the integration variables.

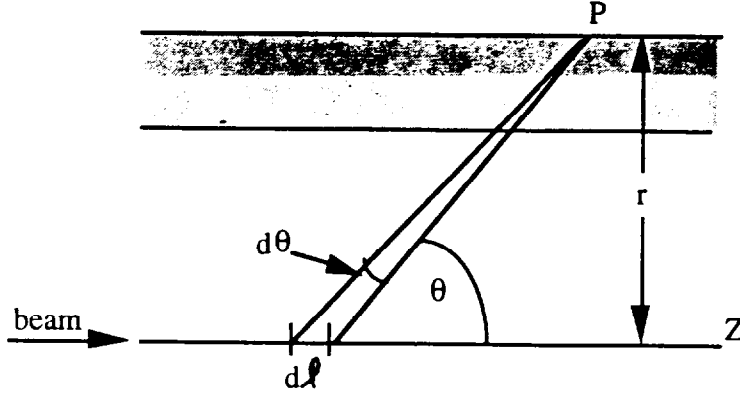


Fig. 3.12 Variables of integration of Moyer point source result to obtain Moyer line source results.

One can integrate the elements dl of a line source at given perpendicular distance r as follows, making the change of variable of integration from the line integral the integral over angle θ ($dl = r \csc^2 \theta d\theta$);

$$H = H_o(E_p) \int_{-\infty}^{\infty} dl \frac{\exp(-\beta\theta) \exp\{-\zeta \csc(\theta)\}}{r^2 \csc^2(\theta)} =$$

$$H_o(E_p) \int_0^{\pi} d\theta r \csc^2(\theta) \frac{\exp(-\beta\theta) \exp\{-\zeta \csc(\theta)\}}{r^2 \csc^2(\theta)} =$$

$$\frac{H_o(E_p)}{r} \int_0^{\pi} d\theta \exp(-\beta\theta) \exp\{-\zeta \csc(\theta)\} = \frac{H_o(E_p)}{r} M(\beta, \zeta) \quad (3.28)$$

(per interacting proton per unit length).

Chapter 3 Shielding of Proton and Ion Accelerators

The integral in the above, $M(\beta, \zeta)$, is the **Moyer integral**. The values of this integral have been tabulated in (Ro76).

In view of the above results, $M(2.3, \zeta)$ has obvious special significance and is tabulated extensively in (Sc90). Tesch (Te83)), has made an important contribution in that he determined an approximation to this integral which others have come to call the "Tesch approximation":

$$M_T(2.3, \zeta) = 0.065 \exp(-1.09\zeta). \quad (3.29)$$

For "intermediate" values of ζ , $M_T(2.3, \zeta)$ can be used instead of $M(2.3, \zeta)$ to simplify calculations. Table 3.2 adapted from (Sc90) gives the ratio $M_T(2.3, \zeta)/M(2.3, \zeta)$ as a function of ζ .

Table 3.2 Values of the Ratio $M_T(2.3, z)/M(2.3, z)$ as a function of z .

ζ	$M_T(2.3, \zeta)/M(2.3, \zeta)$
0.2	0.27
1.0	0.53
2.0	0.75
3.0	0.90
4.0	1.00
5.0	1.06
6.0	1.09
7.0	1.10
8.0	1.10
9.0	1.08
10.0	1.06
11.0	1.02
12.0	0.99
13.0	0.95
14.0	0.91
15.0	0.86
16.0	0.82
17.0	0.78
18.0	0.73
19.0	0.69
20.0	0.65

Of course, few so-called "line sources" are actually infinite in length. Thus, the integration would need to be performed over only a finite angular range. Moreover, in practice only a limited angular range (and hence length) contributes significantly to the Moyer integral. Tables 3.3 and 3.4 taken from (Sc90) give angular integration limits (in degrees) corresponding to 90 % of the $M(2.3, \zeta)$ as a function of ζ (Table 3.3) and the distances along the z axis corresponding to 90 % of $M(2.3, \zeta)$ as a function of the radial distance and ζ (Table 3.4).

Chapter 3 Shielding of Proton and Ion Accelerators

Table 3.3 Angular integration limits in degrees which contain 90% of the Moyer Integral $M(2.3, \zeta)$. [Reproduced from (Sc90).]

Depth(ζ)	Lower Limit	Upper Limit	Depth(ζ)	Lower Limit	Upper Limit
2.5	31.52	106.58	11.5	56.65	106.42
3.0	34.35	107.15	12.0	57.25	106.29
3.5	36.19	107.47	12.5	57.84	106.16
4.0	39.00	107.64	13.0	58.45	106.04
4.5	40.91	107.72	13.5	59.09	105.91
5.0	42.67	107.73	14.0	59.74	105.78
5.5	44.10	107.71	14.5	60.25	105.66
6.0	45.77	107.66	15.0	60.66	105.54
6.5	47.22	107.57	15.5	61.07	105.41
7.0	48.51	107.48	16.0	61.49	105.29
7.5	49.58	107.38	16.5	61.91	105.17
8.0	50.68	107.28	17.0	62.34	105.04
8.5	51.86	107.17	17.5	62.77	104.91
9.0	52.70	107.04	18.0	63.22	104.80
9.5	53.51	106.92	18.5	63.67	104.67
10.0	54.34	106.79	19.0	64.08	104.54
10.5	55.21	106.67	19.5	64.36	104.43
11.0	56.07	106.54	20.0	64.63	104.30

Table 3.4 Distances corresponding to 90% limits in Moyer Integrals. [Reproduced from (Sc90).]

Radial distance m	Shield thickness		Upstream limit z_1 m	Downstream limit z_2 m	Total length $z_2 - z_1$ m
	m	ζ			
1.5	0.5	1.0	-4.2	0.3	4.5
2.0	1.0	2.0	-3.7	0.6	4.3
3.5	2.5	5.0	-3.8	1.1	4.9
6.0	5.0	10.0	-4.3	1.8	6.1
8.5	7.5	15.0	-4.8	2.4	7.2
11.0	10.0	20.0	-5.2	2.8	8.0

The Moyer Model generally does not work at forward angles. For these situations, the Boltzmann equation must be solved. Monte-Carlo calculations are often the best approximation to such solutions. It should be pointed out that (McC85) demonstrates that the Moyer Model approach works for moderately energetic heavy ions. It has been found that the Moyer Model approach works well even into the intermediate energy region $200 < E_0 < 1000$ MeV. This may be interpreted as due to the relatively smooth dependence of neutron yield upon incident proton kinetic energy.

Review of Popular Monte-Carlo Codes [taken from (NC96) and (Sc90).]

HETC

This code, developed over many years under the leadership of R. G. Alsmiller by the Neutron Physics (now Engineering Physics) Division of the Oak Ridge National Laboratory, is the benchmark hadron shielding code. It has been upgraded many times and can, in suitably augmented versions, follow particles from the 20 TeV region down to thermal energies. It is an extremely flexible code but has the important disadvantage that the events are written to tape. It is the responsibility of the user to write a program to analyze the results. In terms of CPU-time HETC is also relatively slow so that calculations to be done should be carefully selected. It is seen to be preferable to use selected HETC runs to "calibrate" some faster, but less accurate code. It is best described by Armstrong (Ref. 28) and Gabriel (29). It now uses the same event generator that FLUKA uses (see below). A simple example of an HETC calculation is given in Fig. 3.13 taken from (Al75) for the case of 200 MeV protons incident on "thin" and "thick" aluminum targets. It plots r^2H as a function of angle for several intervals of θ in a concrete shield.

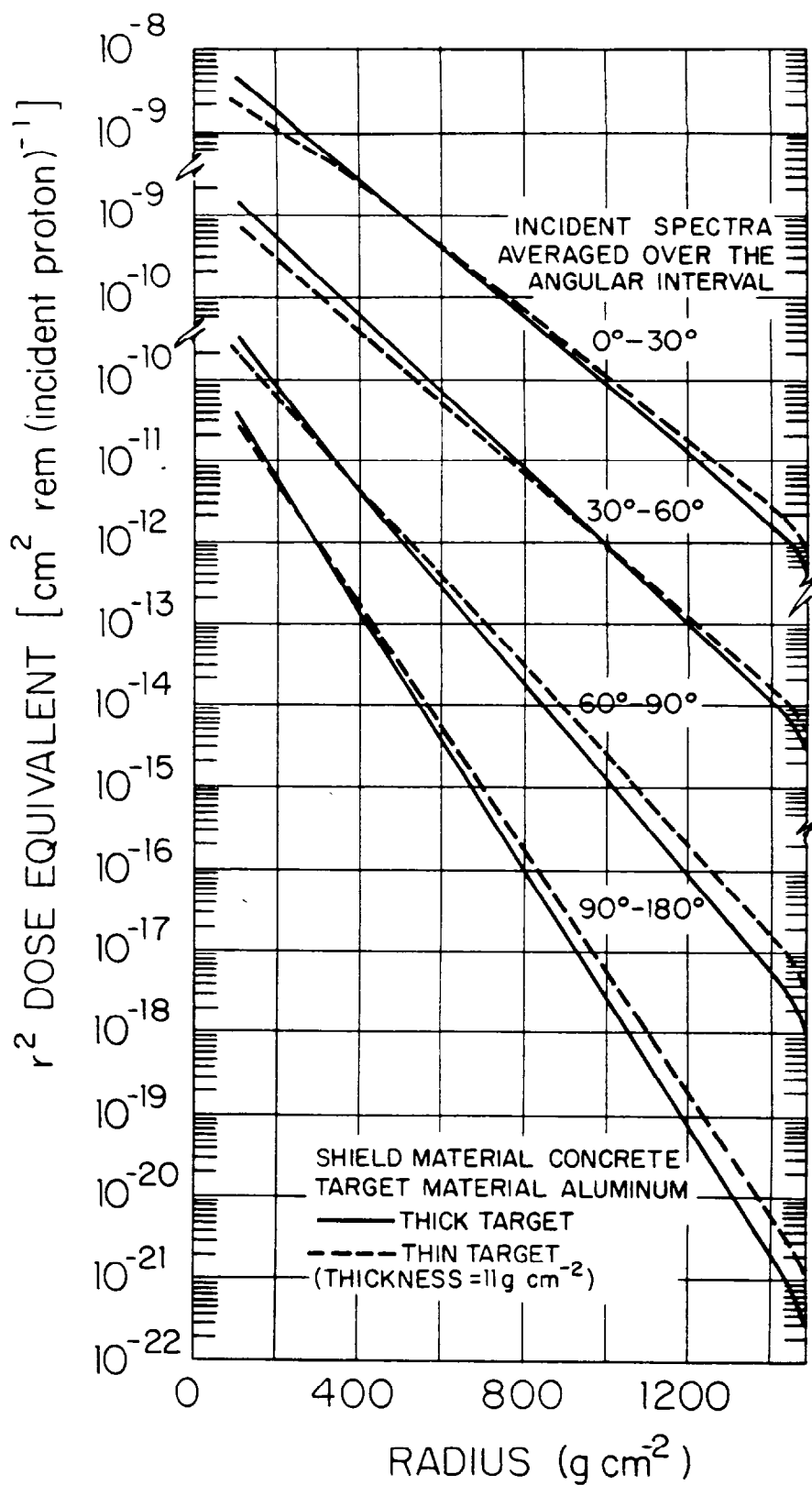


Fig. 3.13 Calculations of r^2H as a function of concrete shield thickness for several intervals of θ for 200 MeV protons incident on an aluminum target. [Reproduced from (A175).]

FLUKA

FLUKA is a module program for computing hadronic and electromagnetic cascades written by J. Ranft of CERN and Leipzig. It can provide flexible multi-region multi-medium geometries and can use a variety of particle production models. It uses weighted Monte-Carlo techniques for special purposes. A recent version, FLUKA82, represents a full analog simulation of the cascade. The most up-to-date production mechanisms of any of the codes and, uncommon among this type of code, quantum number, momentum, and energy conservation are required as a constraint for all collisions. The production models used are scaled to experimental results. Internally, more than 100 hadron resonances are included in the models. Externally, nucleons, pions, kaons, some hyperons, and all their anti-particles are taken into account. Muons (and neutrinos) are not followed. Electromagnetic showers resulting from π^0 production can be fed directly into EGS4. Particles are not followed below 50 MeV kinetic energy. However, this code can be coupled with the standard low-energy photon and neutron code MORSE (Em75) to follow neutrons down to thermal energies. A recent version is described in (Aa86). The geometries come in the form of calls to packages of "combinatorial geometries" which are quite similar to those originally developed at ORNL for MORSE.

CASIM

A. Van Ginneken at Fermilab has developed this program (Va75). It was designed to simulate the average behavior of hadrons in the region 10 to 1000 GeV but has recently been extended to 20 TeV (Va87). It uses inclusive production distributions directly in order to obtain the particles to follow. It uses the Hagedorn-Ranft thermodynamic model. Only one or two high energy particles are created in each collision and these carry a weight related to their probability of production and the energy carried with them. Path length stretching and particle splitting have been introduced. Electromagnetic showers resulting from π^0 production are handled using AEGIS. Simple "standardized" geometries are available. However, the user generally writes a FORTRAN subroutine to set up the geometry of interest. This subroutine consists of "IF" statements used to deduce the location of the particle in space or in magnetic fields. The program readily allows magnetic fields to be used. A muon version called CASIMU (now MUSIM) has been written (Va87). The accuracy of the hadron version has been verified for energies up to 800 GeV (Co82) and the muon version has been verified up to 800 GeV [production and transport in complicated shields, (Co89b)] and 500 GeV [transport in an earth shield (Co89a)]. Normally, CASIM is not set up to follow particles with momenta less than 300 MeV/c, which corresponds to a kinetic energy of 47 MeV for nucleons. All low energy phenomena, then, is obtained by matching energy spectra and fluence at this energy with results of codes capable of tracking lower energy particles (e.g., HETC).

MARS

This program was developed under the leadership of N. Mokhov at the Institute for High Energy Physics at Serpukhov, Russia (Ka84). The current version is denoted MARS10. It is somewhat similar to CASIM in a number of ways but uses a more modern production model; an additive quark model of hadron-nucleus collisions for events having higher momentum transfers while it uses a phenomenological model for the lower energy particle production. It, too, allows multimedia geometries. It now uses AEGIS (see Chapter 2) to follow the electromagnetic cascades. In its present version, it is "rated" to run at 30 TeV, and with crude estimation techniques, even at 10^4 TeV for studies related to the deep underwater muon and neutrino detector (DUMAND) experiment.

Chapter 3 Shielding of Proton and Ion Accelerators

The three high energy codes (FLUKA, CASIM, AND MARS) have been compared in (Mo86). Star and energy deposition densities were calculated for several selected cases and demonstrated to be in generally good agreement with each other, and more importantly, with experiment. An interesting result of this comparison is that a determination of the Moyer Model energy scaling parameter, n , (in E^n) over the range from $70 < E < 2 \times 10^4$ GeV of $n = 0.81$ was made. Using the now obsolete CYBER-875 as a reference computer, MARS and CASIM are of comparable speeds with MARS being somewhat faster for comparable calculations. FLUKA is distinctively slower, but its more exact modeling is likely to be better for problems where studies of the statistical fluctuations are important.

General comments on Monte-Carlo star-to-dose conversions

All of the above codes, in general, calculate **star densities**. This quantity is more correctly called the density of inelastic interactions (stars/cm³). The term "star" comes from historic cosmic ray work in which the high energy interaction events, with their large multiplicities, looked like "pointed stars". The conversion factor from star densities to dose equivalent is rather important and has recently been calculated by Stevenson [in (Sc90)]. While this conversion factor is somewhat dependent upon the position in the shield, after reasonable shield thicknesses (i.e., sufficient to establish "equilibrium" spectra), a constant value may be used. These values are given in Table 3.5 taken from (Sc90). This table also gives the **star fluence** obtained by multiplying by the nuclear interaction length. The star fluence roughly corresponds to the fluence of hadrons having energies above that where the cross section "levels off". For concrete a value of 4.9×10^{-8} Sv cm³/star is obtained.² As one can see, the energy dependence is rather small.

Table 3.5 Coefficients to convert star densities S^* and star fluence ϕ^* into dose equivalent. A star density is transformed into star fluence by the relation $\phi^* = S^* \lambda'$ where λ' is the nuclear interaction length. [Reproduced from (Sc90).]

Proton energy	Target material	Conversion coefficient Sv cm ³ /star All figures $\cdot 10^{-8}$	λ' cm	Conversion coefficient Sv cm ² /star All figures $\cdot 10^{-9}$
10 GeV	Iron	2.04 ± 0.06	17.1	1.19 ± 0.04
100 GeV	Iron	2.15 ± 0.08	17.8	1.21 ± 0.05
1 TeV	Iron	2.12 ± 0.08	17.2	1.23 ± 0.05
Mean	Iron	2.10 ± 0.04		
100 GeV	Aluminium	4.62 ± 0.17	38.6	1.20 ± 0.04
100 GeV	Tungsten	1.19 ± 0.05	9.25	1.29 ± 0.05
Mean	All			1.22 ± 0.02

²The version of this table appearing in (Sc90) contains an error in that the 10^{-9} multiplier applied to the values in the right-most column is incorrectly given in (c90) as 10^{-4} . This was confirmed in a private communication with G. R. Stevenson.

Ref. (Sc90) contains a comprehensive set of Monte-Carlo results. The most popular way to display these results is to give contour plots of star density as function of longitudinal coordinate, Z , and radial coordinate, r , assuming cylindrical symmetry. Results for solid concrete and iron cylinders taken from (Sc90) are reproduced here, respectively, in Figs. 3.14 and 3.15. The dimensions used in the geometries are scaled in size with the proton energy. Table 3.6 adapted from (Sc90) lists the calculations in that reference which are given for Figs. 3.14 and 3.15.

Table 3.6 FLUKA Monte-Carlo calculations for solid concrete and iron beam dumps irradiated with high energy protons. [Adapted from (Sc90).]

Material	Incident Proton Momentum (GeV/c)	Dimensions of Cylinder	
		Z (cm)	R (cm)
Concrete	1	250	50
	10	500	100
	10^2	1250	250
	10^3	1250	250
	10^4	1250	250
Iron	1	200	50
	10	300	50
	10^2	500	150
	10^3	500	150
	10^4	500	150

Chapter 3 Shielding of Proton and Ion Accelerators

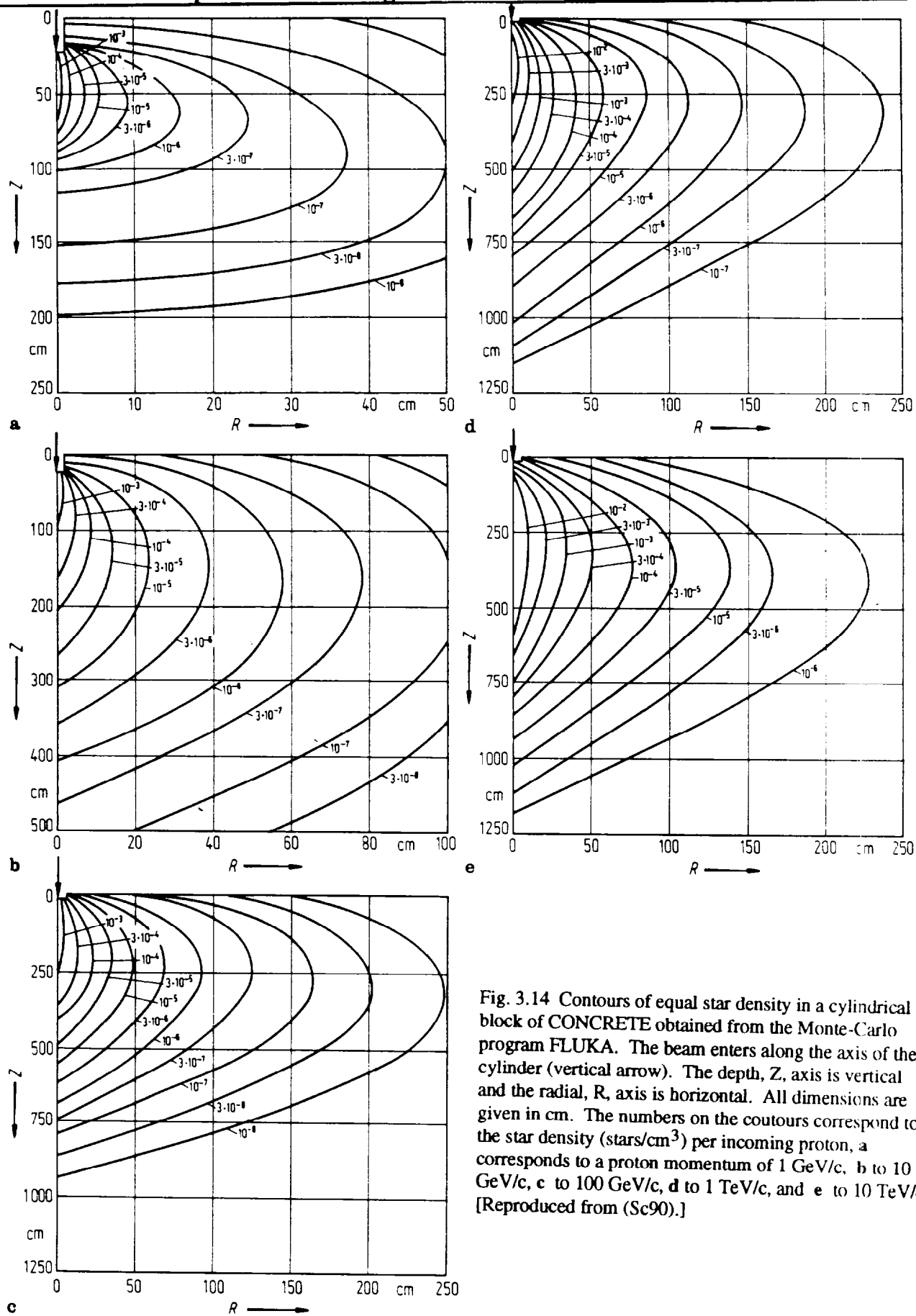


Fig. 3.14 Contours of equal star density in a cylindrical block of CONCRETE obtained from the Monte-Carlo program FLUKA. The beam enters along the axis of the cylinder (vertical arrow). The depth, Z , axis is vertical and the radial, R , axis is horizontal. All dimensions are given in cm. The numbers on the contours correspond to the star density (stars/cm³) per incoming proton, a corresponds to a proton momentum of 1 GeV/c, b to 10 GeV/c, c to 100 GeV/c, d to 1 TeV/c, and e to 10 TeV/c. [Reproduced from (Sc90).]

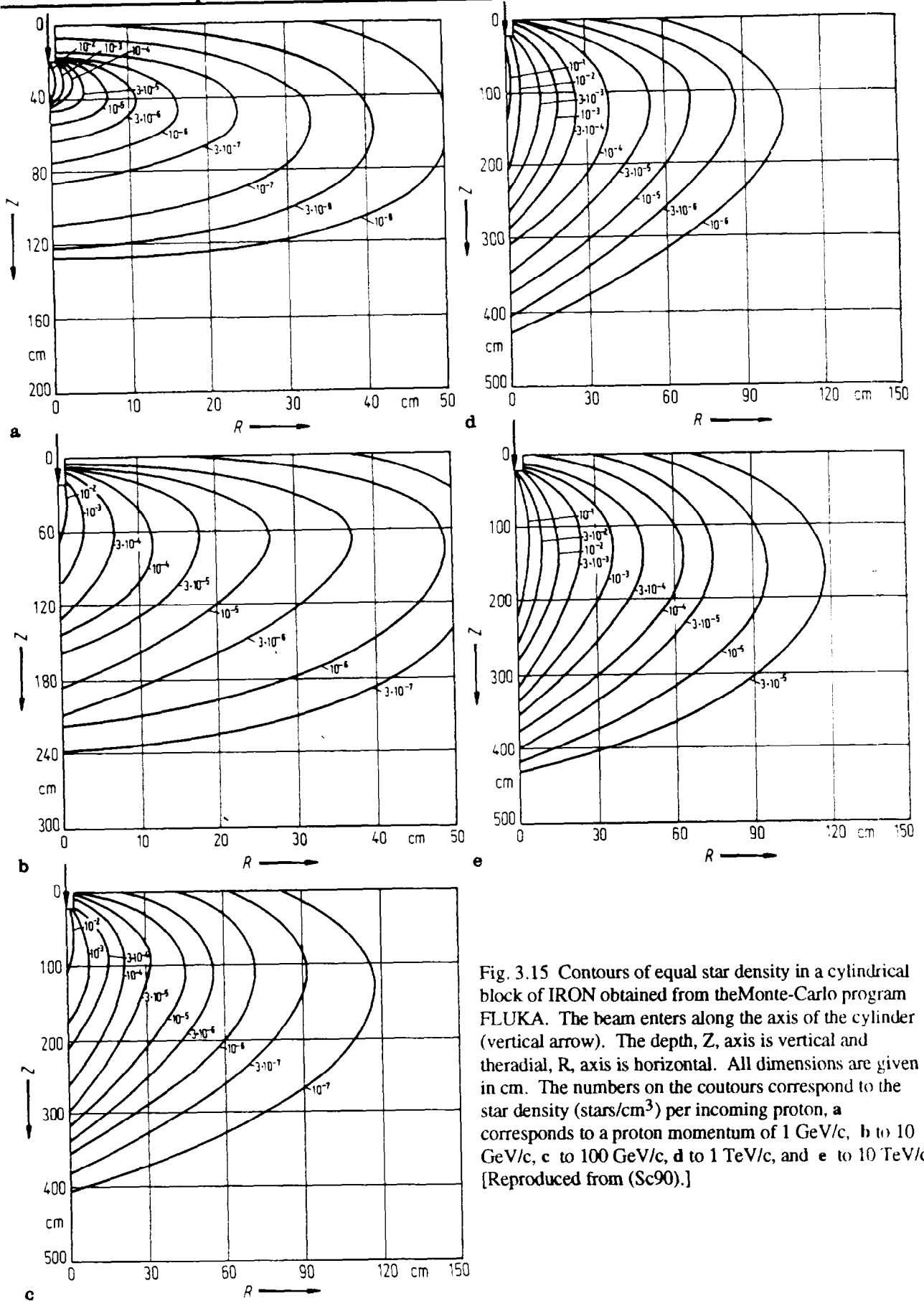


Fig. 3.15 Contours of equal star density in a cylindrical block of IRON obtained from the Monte-Carlo program FLUKA. The beam enters along the axis of the cylinder (vertical arrow). The depth, Z , axis is vertical and the radial, R , axis is horizontal. All dimensions are given in cm. The numbers on the contours correspond to the star density (stars/cm³) per incoming proton, **a** corresponds to a proton momentum of 1 GeV/c, **b** to 10 GeV/c, **c** to 100 GeV/c, **d** to 1 TeV/c, and **e** to 10 TeV/c. [Reproduced from (Sc90).]

(Sc90) also gives results for the important calculations of equal star densities and dose equivalents due to protons incident on a target inside of a magnet located in a tunnel. (Cylindrical symmetry is used.) Table 3.7 taken from (Sc90) gives the dimensions used for the various momenta considered. Fig. 3.16 taken from (Sc90) shows the situation schematically. The magnet consists of iron and is centered in a concrete tunnel. Around the small target is an iron vacuum tube. The results of the FLUKA calculations (contour plots of equal star density) at 10 GeV/c, 100 GeV/c, and 10 TeV/c are presented in Fig 3.17 taken from (Sc90).

**Table 3.7 Dimensions used in Fig. 3.16 for various momenta.
[Reproduced from (Sc90).]**

	Momentum		
	10 GeV/c	100 GeV/c	10 TeV/c
R_t : Radius of target (beryllium) [cm]	2	2	2
R_1 : Inner radius of vacuum pipe [cm]	4.9	4.9	4.9
R_2 : Outer radius of vacuum pipe = radius of magnet bore [cm]	5.0	5.0	5.0
R_3 : Outer radius of magnet (iron) [cm]	25	25	25
R_4 : Inner radius of tunnel [cm]	150	150	150
R_5 : Outer radius of tunnel [cm]	250	250	250
X_0 : Start of tunnel [m]	0	0	0
x_1 : Upstream end of magnet [m]	10	10	100
x_{t_1} : Target position [m]	11.0	11.0	101.0
x_{t_2} : Target position [m]	11.1	11.1	101.1
x_2 : Downstream end of magnet [m]	20	20	200
x_3 : End of tunnel [m]	100	100	1000
Figure number	2.43 a	2.43 b	2.43 c

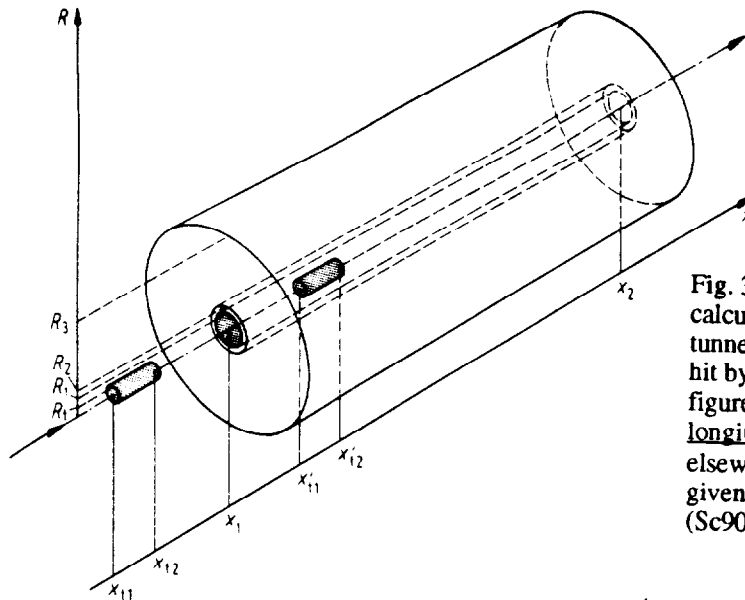


Fig. 3.16 Geometry for the Monte-Carlo calculations of star densities in a concrete tunnel when a beryllium target in a magnet is hit by a proton beam. Note that in this figure, the coordinate labeled "x" is the longitudinal coordinate labeled "z" elsewhere. The resultant calculations are given in Fig. 3.17. [Reproduced from (Sc90).]

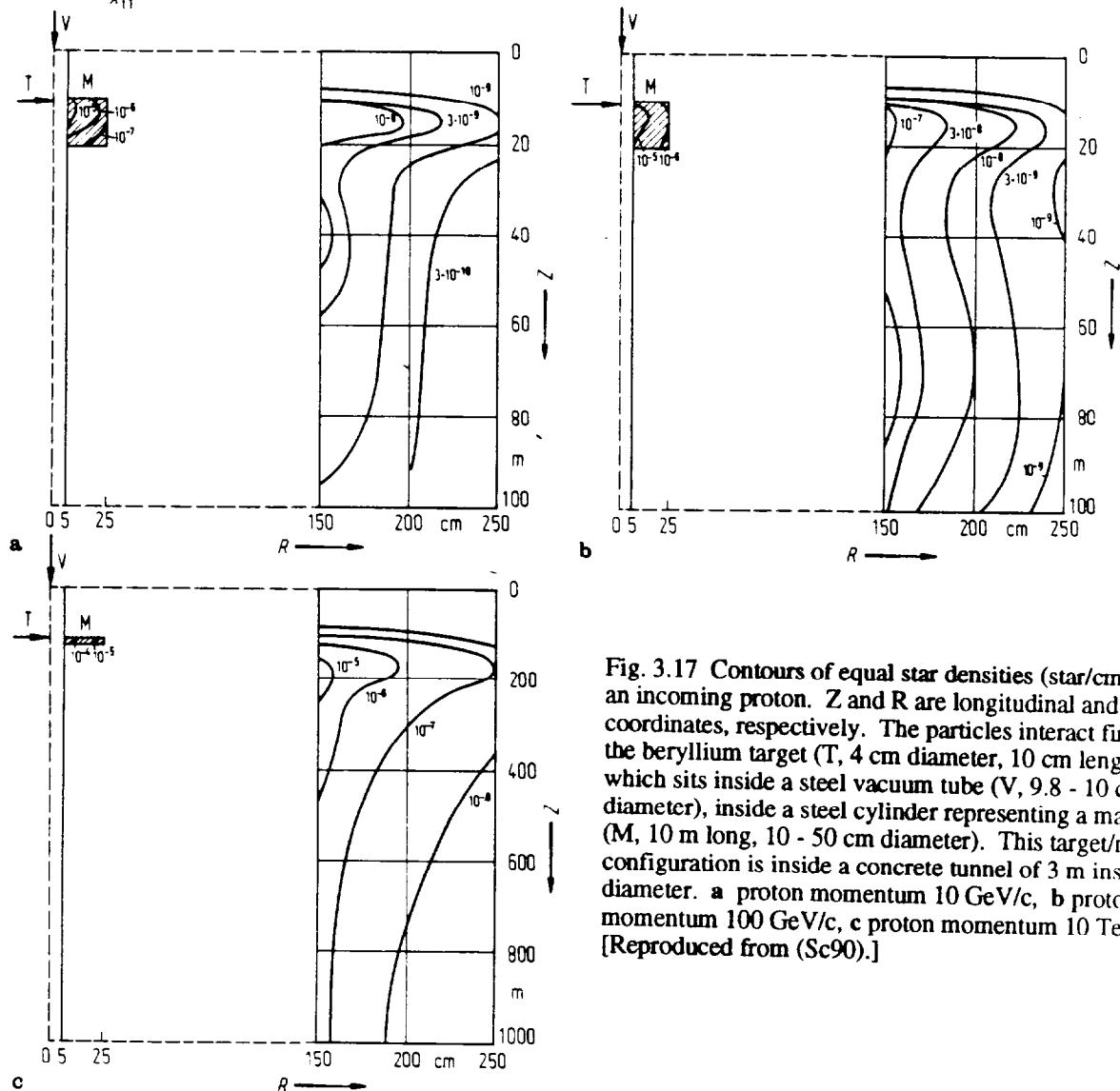


Fig. 3.17 Contours of equal star densities (star/cm³) for an incoming proton. Z and R are longitudinal and radial coordinates, respectively. The particles interact first in the beryllium target (T, 4 cm diameter, 10 cm length) which sits inside a steel vacuum tube (V, 9.8 - 10 cm diameter), inside a steel cylinder representing a magnet (M, 10 m long, 10 - 50 cm diameter). This target/magnet configuration is inside a concrete tunnel of 3 m inside diameter. a proton momentum 10 GeV/c, b proton momentum 100 GeV/c, c proton momentum 10 TeV/c. [Reproduced from (Sc90).]

A comparison of FLUKA and CASIM in terms of the maximum dose equivalent per proton as a function of radius for different energies is given in Fig. 3.18 taken from (Sc90). The solid curve is essentially the Moyer Model.

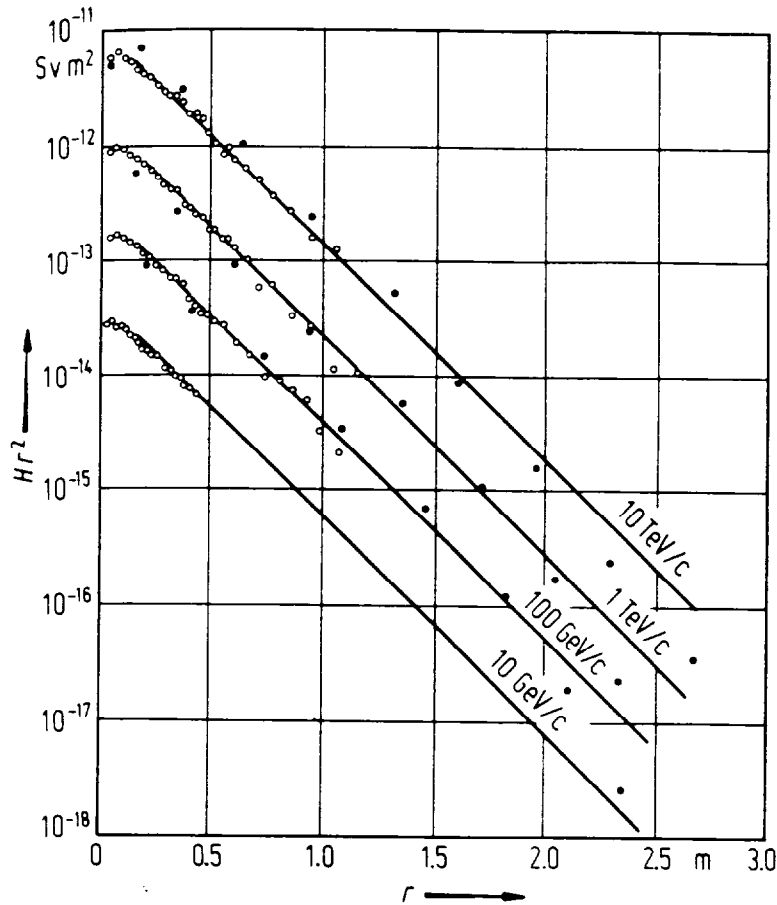


Fig. 3.18 Variation of the dose equivalent per proton at the position of the longitudinal maximum multiplied by the square of the radius Hr^2 vs radius off-axis for proton induced cascades in iron of density 7.2 g cm^{-3} . Open circles are the FLUKA calculations; full circles indicate the CASIM calculations. The solid lines are derived from the empirical parametrizations. [Reproduced from (Sc90).]

Longitudinally, FLUKA and CASIM results in iron and concrete shields are compared in Figs. 3.19 and 3.20, respectively, taken from (Sc90).

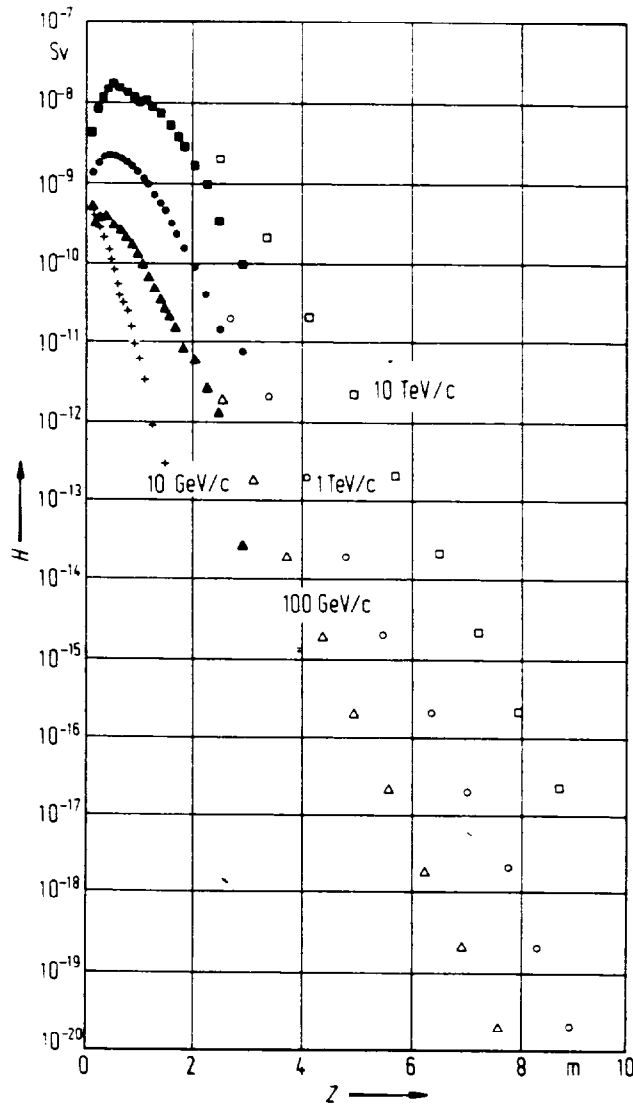


Fig. 3.19 Variations of the dose equivalent per proton H on the longitudinal axis vs. depth Z in the shield for proton-induced cascades in IRON of density 7.2 g cm^{-3} . The solid symbols represent FLUKA calculations for incident proton momenta of 10 GeV/c, 100 GeV/c, 1 TeV/c, and 10 TeV/c. The open symbols correspond to CASIM calculations at the marked proton momenta. There are no CASIM results for 10 GeV/c. [Reproduced from (Sc90).]

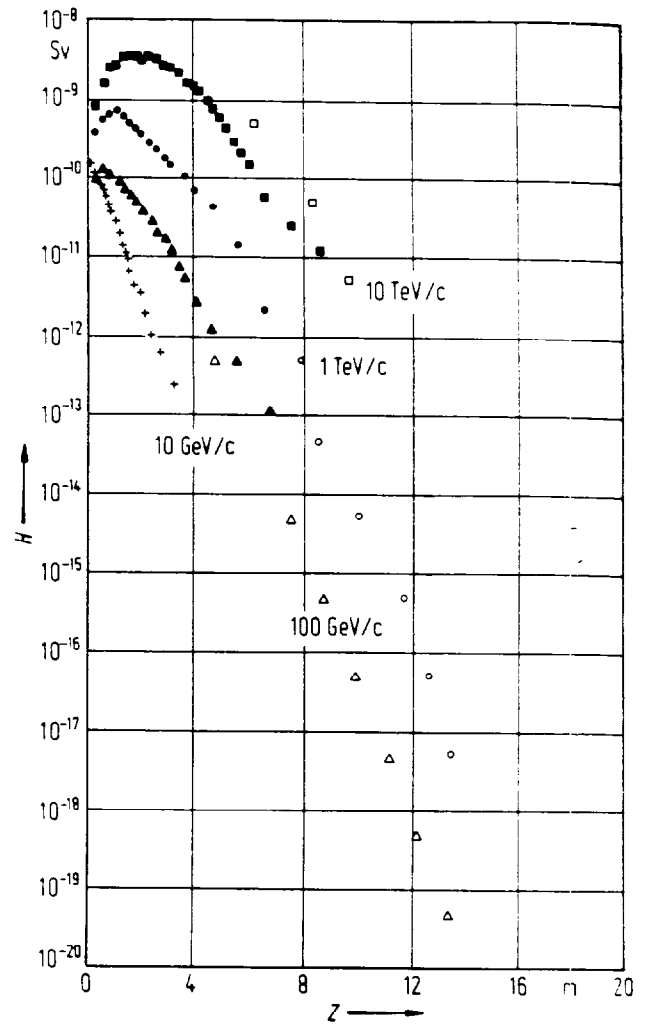


Fig. 3.20 Variations of the dose equivalent per proton H on the longitudinal axis vs. depth Z in the shield for proton-induced cascades in CONCRETE of density 2.4 g cm^{-3} . The solid symbols represent FLUKA calculations for incident proton momenta of 10 GeV/c, 100 GeV/c, 1 TeV/c, and 10 TeV/c. The open symbols correspond to CASIM calculations at the marked proton momenta. There are no CASIM results for 10 GeV/c. [Reproduced from (Sc90).]

Shielding Against Muons at Proton Accelerators

Muon production has been discussed previously in Chapter 1. At the higher energies, there are significant complications in that muon creation mechanisms in addition to pion and kaon production and subsequent decay are possible. However, the muons from pion and kaon decay generally, but not universally, represent the most important consideration in practical shielding calculations. In Monte-Carlo calculations, it is straightforward to "create" muons and follow them through the shielding medium. The previous discussion of Monte-Carlo programs discusses this topic.

Muon transport is well understood. Because of the lack of strong interactions, their absorption cross sections in shielding materials are negligible. The energy loss is dominated by ionization and excitation of atomic electrons. Coulomb scattering alters their paths. Because of their higher masses, radiative energy losses do not become important until their energies reach approximately 100 GeV. Other energy loss mechanisms also become important at the higher energies. The range-energy relations for muons were discussed in Chapter 1.

The effect of beam loss mechanisms on dose at proton and ion accelerators is, however, considerably different than in the electron situation. The particle energy downgrades quickly in hadronic showers so the most penetrating muons must originate in the first few generations of the process. These energetic muons are not "smeared out" in a large volume of phase space as are the neutrons. However, geometric effects or deflections by magnetic fields encountered near the point of production can affect the muon fluence at large distances. Thus, the presence of large "empty" spaces (vacuum or air) near the point of interaction provide opportunity for the pions or kaons to decay into muons before they can be removed by nuclear interactions in solid materials. This is particularly important for the typical situation of a target used to produce secondary beams followed (downstream) by an air or vacuum gap (the space for decay into muons) and then a beam dump. If magnetic fields are present, the muon fluence generally peaks in the bend plane.

As discussed before, muon calculations are extremely difficult except when using Monte-Carlo calculations because of the sensitivity to details of the geometry which determine the pion and kaon flight paths and influence the muon populations. (Sc90), however, contains useful information about the production of muons that one can use to make crude estimates. There are some features, discussed in (Sc90) and elsewhere, which are important.

Multiple scattering is an important effect in muon transport. There are several types of scattering that occur. The most important of these is due to elastic Coulomb scattering from the nuclei. An appropriate Gaussian approximation of such scattering for all charged particles carrying electronic charge z ($z=1$ for muons) having mean width θ_0 in space projected onto the plane of the initial direction of the particle is as follows:

$$\theta_0 = \frac{14.1 \text{ (MeV/c)} z}{p\beta} \sqrt{L/X_0} \left[1 + \frac{1}{9} (L/X_0) \right] \text{ radians} \quad (3.30)$$

where X_0 is the the radiation length defined as in Chapters 1 and 2, p is momentum in MeV/c and L is the shield thickness in the same units as the radiation length. The distribution is fit by the following function:

$$f(\theta)d\theta = \left(\frac{d\theta}{\theta_0 \sqrt{2\pi}} \right) \exp \left\{ -\frac{\theta^2}{2\theta_0^2} \right\}. \quad (3.31)$$

Chapter 3 Shielding of Proton and Ion Accelerators

Generally the most copious source of muons are those due to the decay of pions and kaons. There are several important facts about such muons which are summarized below.

- A. The decay lengths (mean length for π or K to decay), Λ , are:

$$\Lambda_{\pi} = 55.9p \text{ (meters), where } p \text{ is the pion momentum in GeV/c,}$$

$$\Lambda_K = 7.51p \text{ (meters), where } p \text{ is the kaon momentum in GeV/c.}$$

The decay length can be used to estimate the total number of muons present. For example, a beam of 10^7 pions at 20 GeV/c will decay in a distance of 50 meters into $10^7 \times [50 \text{ meters}] / [56 \times 20 \text{ meters decay length}] = 5 \times 10^5$ muons. [This uses the fact that the path length (50 meters) is small compared with the mean decay length of 1120 meters. If the path length, x , was comparable to the decay length, Λ , the intensity of 10^7 would be multiplied by the exponential factor $\{1 - \exp(x/\Lambda)\}$.]

- B. If $\beta \approx 1$, relativistic kinematics determines that the ratio, k_i , of the minimum momentum of the daughter muon (p_{\min}) to the momentum of the parent pion or kaon (p_i) is given by:

$$k_i = p_{\min}/p_{\text{parent}} = (m_{\mu}/m_{\text{parent}})^2. \quad (3.32)$$

The result is that k_i has a value of 0.57 for muons with pion parents and 0.046 for muons with kaon parents. Thus if, say, a beam transport system restricts the momentum of pions to some minimum value, then a minimum value given by the above is placed on the muon momentum at the time of decay.

- C. Since in the center of mass frame of reference the decay is isotropic, and there is a one-to-one relationship between the muon momentum and the angle of emission, for muon momenta $\gg m_{\text{parent}}$ (in units where $c = 1$) the momentum spectrum of the muons can be expressed as $dN/dp = 1/[p_{\text{parent}}(1-k_i)]$. This means that the spectrum of daughter muons uniformly extends from the momentum of the parent down to the minimum established in Eq. (3.32).
- D. Relativistic kinematics also gives the result that the maximum angle, in the laboratory frame of reference, between the momentum vector of the muon and that of the parent particle is given by:

$$\tan \theta_{\max} = (m_{\text{parent}}^2 - m_{\mu}^2)/2p_{\text{parent}}m_{\mu}. \quad (3.33)$$

For muons originating from pion decay, θ_{\max} is at most several milliradians. However, for muons originating from the decay of 5 GeV kaons, θ_{\max} is a relatively large 12° . Thus $\pi \rightarrow \mu$ decays can be assumed to be collinear while $K \rightarrow \mu$ decays have significant divergence at the lower energies.

(Sc90) gives calculated values of angular distributions of muon spectra with an absolute normalization from pion and kaon decays for one meter decay paths. For other decay paths which are short compared with the decay length, one can simply scale by the length of the actual decay path. Results are given in Fig. 3.21.

Decays of other particles can be important sources of muons at higher energies. Especially notable are those from charm (D) and bottom (B) meson decays (Sc90). The muons from these sources are often called "direct" muons due to the short lifetimes and decay lengths involved. The masses of these parent particles and their meanlives, τ , are as follows:

$$m(D^\pm) = 1869.3 \pm 0.5 \text{ MeV}, \tau = (10.66 \pm 0.23) \times 10^{-13} \text{ s}, c\tau = 320 \text{ } \mu\text{m}$$

$$m(B^\pm) = 5278.6 \pm 2.0 \text{ MeV}, \tau = (12.9 \pm 0.5) \times 10^{-13} \text{ s}, c\tau = 387 \text{ } \mu\text{m}.$$

Figures 3.22, and 3.23 taken from (Sc90) give results for muons originating from these decays. The results in Fig. 3.21 are for one meter decay paths. One must take care in reading Figs. 3.21 - 3.23. In these figures are presented cumulative spectra. That is, the ordinate is the yield of muons per unit solid angle having energy greater than the value of the abscissa. The abscissa is the ratio of muon energy to the proton energy.

An approximate method for calculating muon flux densities at proton accelerators has been developed by (Su92) and is based upon a semi-empirical fit to existing muon production data. The first result from Sullivan's work is an equation for the flux density of muons per meter of decay path as a function of shield thickness found along the proton beam axis (that is, on the straight-ahead maximum of the muons):

$$\phi = 0.085 \frac{E x}{X^2} \exp \{ - \alpha t / E \}, \quad (3.34)$$

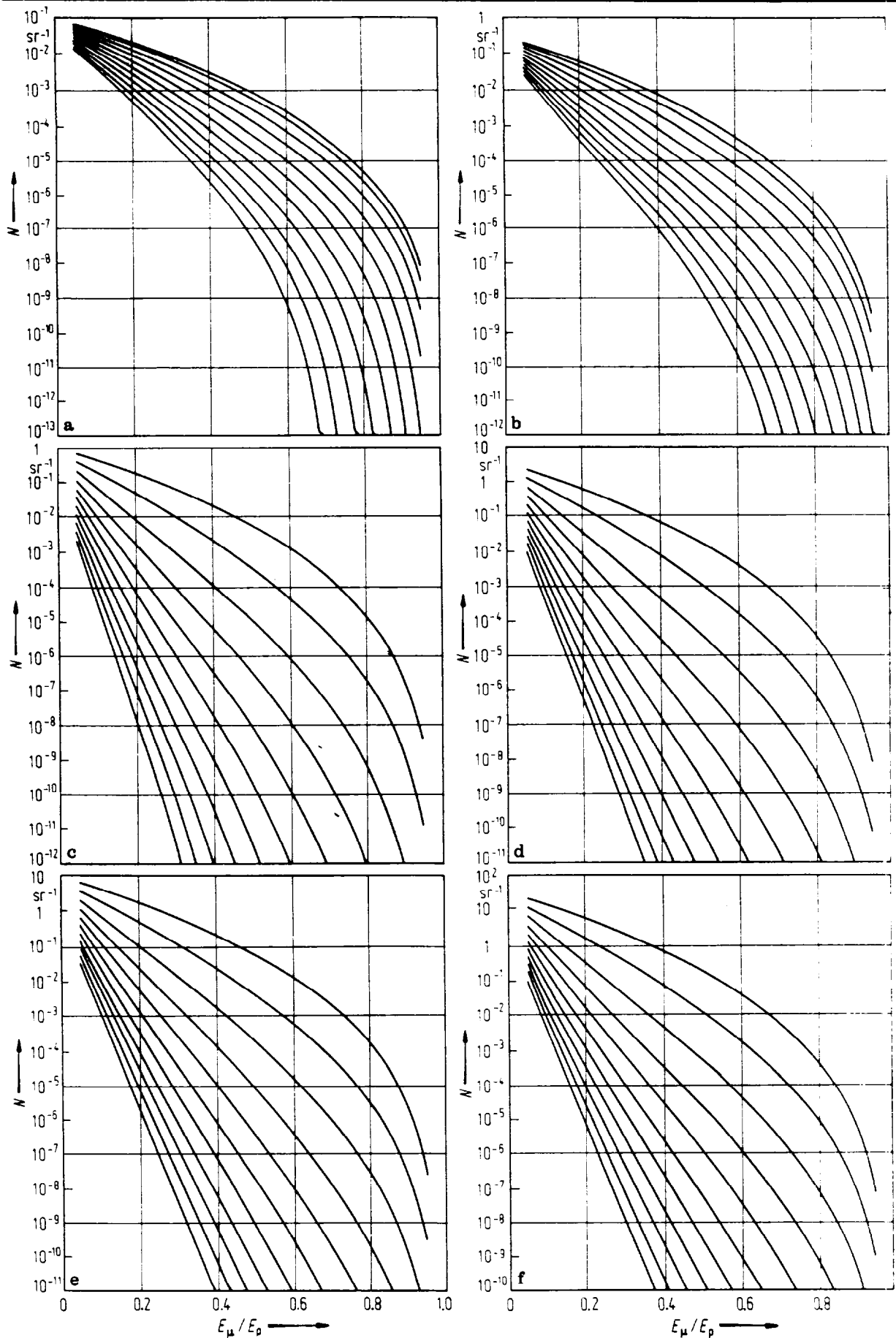
where ϕ is the flux density (muons/m²) per interacting proton, E is the proton beam energy (GeV), X is the distance of the point of concern to the point of interaction (meters), x is the average path length (i.e., the decay path) of the pions and kaons prior to interaction, and α is an effective average energy loss rate (GeV/meter) for the muons in a shield of thickness t (meters). x can be taken to be the actual physical length of the decay path or, for a beam dump situation, according to Sullivan, it can reasonably be taken to have the value of 1.8 times the hadron nuclear interaction mean free path for the material comprising the beam dump. Values of α have been tabulated by Sullivan and for typical shielding materials have the following values:

$$\begin{aligned} \alpha_{\text{concrete}} &= 9.0 \text{ GeV/meter (for } \rho = 2.35 \text{ g cm}^{-3}\text{)} \\ \alpha_{\text{water}} &= 4.0 \text{ GeV/meter (for } \rho = 1.0 \text{ g cm}^{-3}\text{)} \\ \alpha_{\text{iron}} &= 23.0 \text{ GeV/meter (for } \rho = 7.4 \text{ g cm}^{-3}\text{)} \\ \alpha_{\text{lead}} &= 29.0 \text{ GeV/meter (for } \rho = 11.3 \text{ g cm}^{-3}\text{)}. \end{aligned}$$

The value for concrete can be used for earth if one adjusts it to the correct density. It is obvious that the argument of the exponential in Eq. (3.34) can be expanded as the sum over the materials comprising a composite shield. Sullivan has also given a prescription for calculating the full width at half maximum (FWHM) of the muon distribution at the boundary of such a shield. This is given by:

$$\text{FWHM} = 4.6 \frac{X}{\sqrt{E \alpha t}} \text{ (meters)}. \quad (3.35)$$

Chapter 3 Shielding of Proton and Ion Accelerators



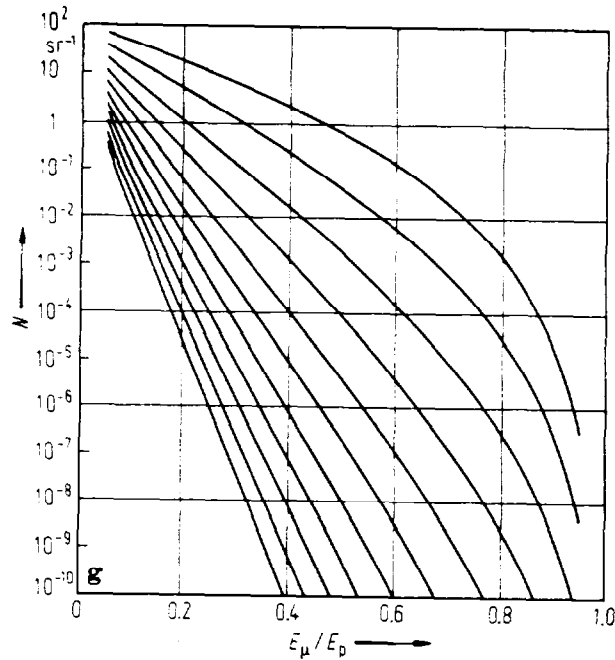


Fig. 3.21 Muons from the decay of pions and kaons of both charges produced in proton-Fe collisions at various energies of the incident proton. The distance available for decay is assumed to be 1 meter. The abscissa, E_μ/E_p is the muon energy expressed as a fraction of the incident proton energy. The ordinate, N , is the number of muons per unit solid angle having an energy greater than E_μ , expressed in sr^{-1} . The uppermost curve in each case is for production angle $\theta = 0$; the other curves represent the production at other angles in increments of $\Delta\theta$, listed below for the different proton energies E_p . **a** $E_p = 10 \text{ GeV}$; $\Delta\theta = 30$ milliradians, **b** $E_p = 30 \text{ GeV}$; $\Delta\theta = 15$ milliradians, **c** $E_p = 100 \text{ GeV}$; $\Delta\theta = 15$ milliradians, **d** $E_p = 300 \text{ GeV}$; $\Delta\theta = 5$ milliradians, **e** $E_p = 1000 \text{ GeV}$; $\Delta\theta = 1.5$ milliradians, **f** $E_p = 3000 \text{ GeV}$; $\Delta\theta = 0.5$ milliradians, **g** $E_p = 10,000 \text{ GeV}$; $\Delta\theta = 0.15$ milliradians. [Reproduced from (Sc90).]

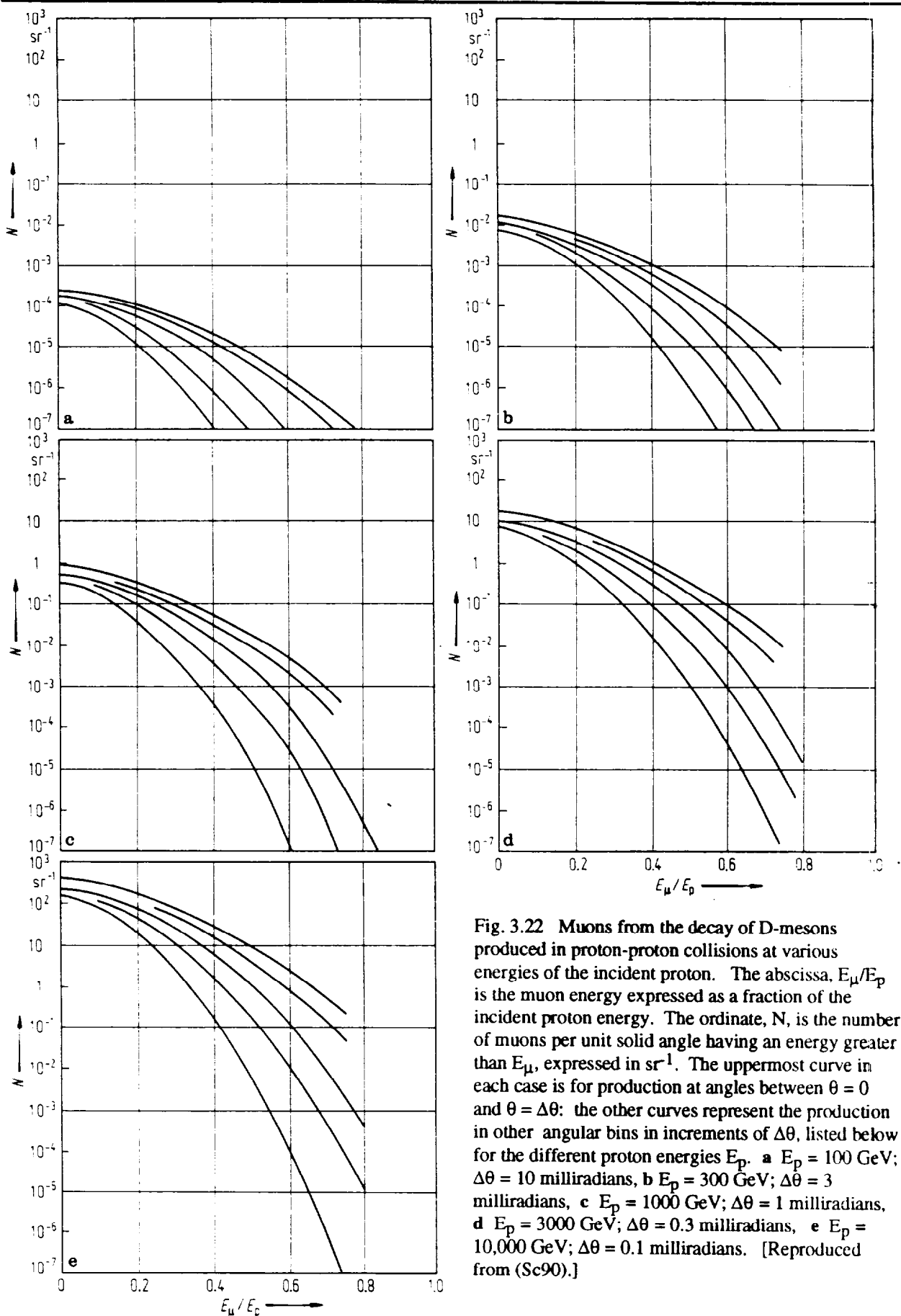


Fig. 3.22 Muons from the decay of D-mesons produced in proton-proton collisions at various energies of the incident proton. The abscissa, E_μ/E_p is the muon energy expressed as a fraction of the incident proton energy. The ordinate, N , is the number of muons per unit solid angle having an energy greater than E_μ , expressed in sr^{-1} . The uppermost curve in each case is for production at angles between $\theta = 0$ and $\theta = \Delta\theta$; the other curves represent the production in other angular bins in increments of $\Delta\theta$, listed below for the different proton energies E_p . **a** $E_p = 100$ GeV; $\Delta\theta = 10$ milliradians, **b** $E_p = 300$ GeV; $\Delta\theta = 3$ milliradians, **c** $E_p = 1000$ GeV; $\Delta\theta = 1$ milliradians, **d** $E_p = 3000$ GeV; $\Delta\theta = 0.3$ milliradians, **e** $E_p = 10,000$ GeV; $\Delta\theta = 0.1$ milliradians. [Reproduced from (Sc90).]

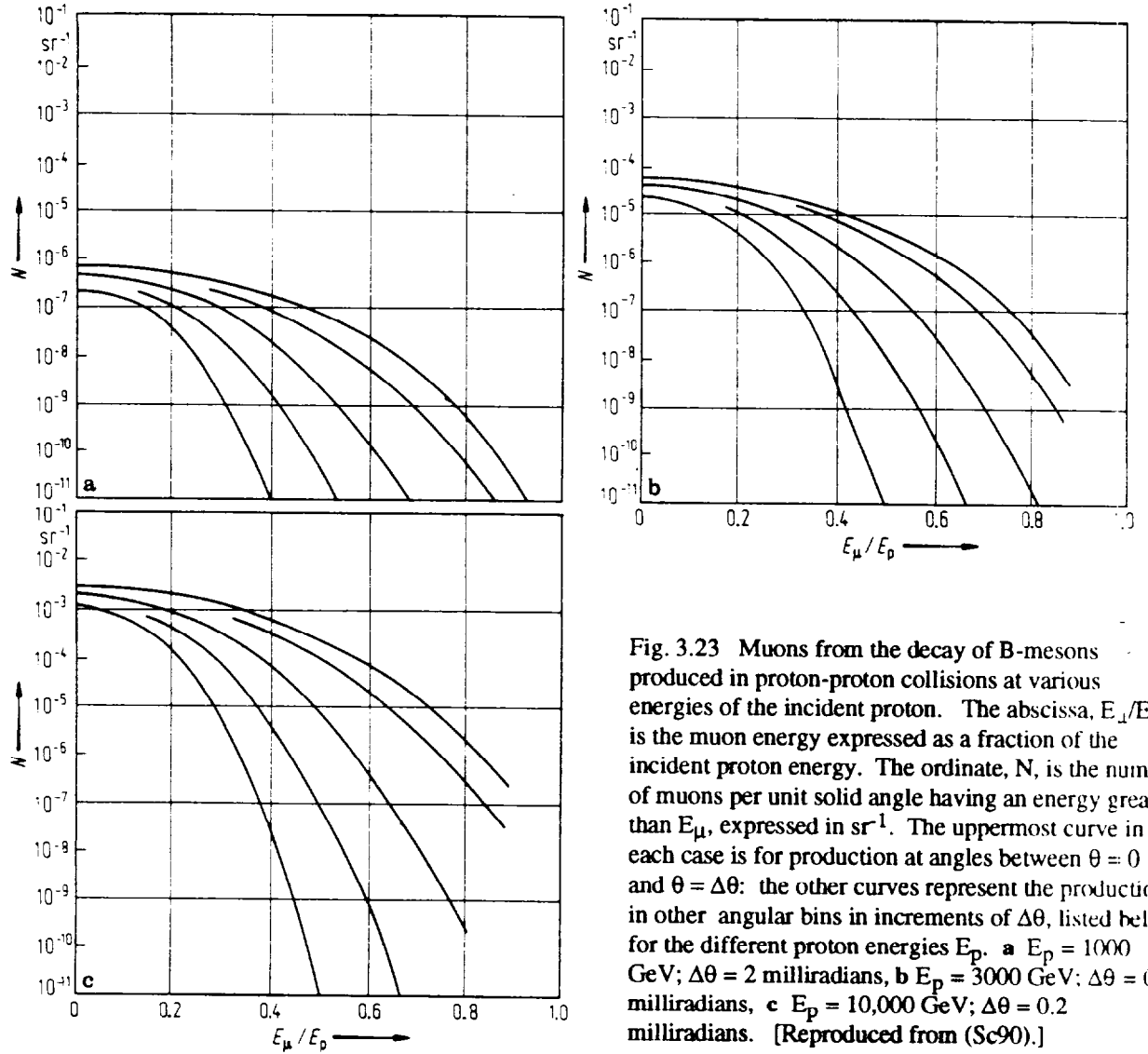


Fig. 3.23 Muons from the decay of B-mesons produced in proton-proton collisions at various energies of the incident proton. The abscissa, E_μ/E_p is the muon energy expressed as a fraction of the incident proton energy. The ordinate, N , is the number of muons per unit solid angle having an energy greater than E_μ , expressed in sr^{-1} . The uppermost curve in each case is for production at angles between $\theta = 0$ and $\theta = \Delta\theta$; the other curves represent the production in other angular bins in increments of $\Delta\theta$, listed below for the different proton energies E_p . **a** $E_p = 1000$ GeV; $\Delta\theta = 2$ milliradians, **b** $E_p = 3000$ GeV; $\Delta\theta = 0.6$ milliradians, **c** $E_p = 10,000$ GeV; $\Delta\theta = 0.2$ milliradians. [Reproduced from (Sc90).]

IV. Shielding Materials and Neutron Energy Spectra

Shielding Materials [largely taken from (NC96) and (Th88)]

Given the size of many modern accelerators, economic considerations often dominate shielding designs by requiring the use of relatively inexpensive, but less efficient shields. In all cases, good engineering practices concerning structural properties, appropriate floor loading allowances, and fire protection considerations must be appropriately taken into account to provide an acceptable degree of conventional safety.

In general, low atomic number materials are best used for targets, collimators, and beam stops at electron accelerators to reduce photon production, while high atomic number materials are preferred at proton and heavy ion accelerators for these components to reduce neutron production. However, at ion energies above 5 MeV neutrons are produced in most materials. Some materials have superior heat transfer characteristics which enhances reliability and thus can reduce personal exposures incurred in maintenance activities.

-earth

Earth has many admirable qualities as a shield material besides its economy. The water it contains enhances the effectiveness of the neutron attenuation, yet it is composed of sufficiently high atomic number elements to be effective against photons. Representative ranges of soil water content (per cent of dry weight) are: sand (0-10), sandy loam (5-20), loam (8-25), silty loam (10-30), dry loam (14-30), and clay (15-30). Dry earth has a typical elemental composition as given in Table 3.8 taken from (Ch84).

Earth is generally a "crackless" shield, not prone to neutron leakage by "streaming". The density of earth varies widely, from as low as $1.7 \text{ g}\cdot\text{cm}^{-3}$ to as much as $2.25 \text{ g}\cdot\text{cm}^{-3}$ depending upon soil type and water content. Given this variation, specific knowledge of soil characteristics at the accelerator site are needed to do effective shielding designs. Definitive measurements of the water content are also most useful if the shielding of neutrons is the intent and only small safety factors are being used.

Table 3.8 Elemental Composition, Dry-Weight Percent Basis, of Representative Soils. [Reproduced from (Ch84).]

Element	Global Average (%)
O	43.77
Si	28.1
Al	8.24
Fe	5.09
Mn	0.07 ± 0.06
Ti	0.45 ± 0.43
Ca	3.65
Mg	2.11
K	2.64
Na	2.84

-concrete

Concrete has obvious advantages in that it can either be poured in place permanently or be cast into modular blocks. Sometimes concrete is used to shield targets, beam stops, etc. in a manner that allows their ready access if the need for maintenance arises. The use of concrete blocks generally requires the overlapping of the blocks to avoid streaming through the cracks.

It is sometimes efficient to use a heavy material as part of the aggregate in the concrete recipe. This can increase the density of the material as well as its average atomic number. The latter, of course, increases the effectiveness against photons. Table 3.9 adapted from (Ch84) gives some partial densities of various concretes used in shielding. When shielding neutrons, the water content is quite important because it incorporates almost all of the hydrogen. Under "extreme" low-humidity conditions, the water content of concrete can decrease with time, to as little as 50 % of the initial value over a 20 year period.

Table 3.9 Partial Densities of Representative Concretes After Curing. [Adapted from (Ch894).]

Type: Additive	Ordinary	Magnetite (FeO, Fe ₂ O ₃)	Barytes BaSO ₄	Magnetite & Fe
Density (g/cm ³)	2.34	3.53	3.35	4.64
H	0.013	0.011	0.012	0.011
O	1.165	1.168	1.043	0.638
Si	0.737	0.091	0.035	0.073
Ca	0.194	0.251	0.168	0.258
Na	0.040			
Mg	0.006	0.033	0.004	0.017
Al	0.107	0.083	0.014	0.048
S	0.003	0.005	0.361	
K	0.045		0.159	
Fe	0.029	1.676		3.512
Ti		0.192		0.074
Cr		0.006		
Mn		0.007		
V		0.011		0.003
Ba			1.551	

[Local densities of "ordinary" concrete vary considerably, up to 2.5 g/cm³.]

-other hydrogenous materials

Polyethylene and other materials subject to boration: (CH₂)_n is a very effective neutron shield because of its hydrogen content (14% by weight) and its density (0.92 g·cm⁻³). The addition of boron can reduce the buildup of 2.2 MeV photons released in the thermal neutron capture by hydrogen by instead capturing the thermal neutrons in the boron, where the decay reaction produces an easily attenuated α-particle plus a more readily attenuated 0.48 MeV photon.

Commercially, polyethylene is available including additives of boron (up to 32%), lithium (up to 10 %) and lead (up to 80 %) in various forms such as planer sheets, spheres, and cylinders.

Chapter 3 Shielding of Proton and Ion Accelerators

These materials can be useful, if it is necessary, to economize on space and also to accomplish shielding of photons and neutrons simultaneously.

Pure polyethylene is flammable, but some of the commercial products available contain self-extinguishing additives. Some of these materials are available in powder form, for molding into a desired shape by the user. Besides polyethylene, boron has been added to other materials to form effective thermal neutron shields. These include other plastics, putties, clays, and glasses to accomplish specific shielding objectives.

The three materials water, wood, and paraffin are superficially attractive neutron shields because of their very high hydrogen contents.

Water, of course, tends to rust out its containers and there is the omnipresent question as to whether the shield has gone "down the drain". Exposed to thermal neutrons, it also emits the 2.2 MeV capture γ -ray from hydrogen. Boration is more difficult because of the relative insolubility of boron salts in water.

Wood was found in the early years of operation at the Bevatron to be as effective as concrete for shielding intermediate energy neutrons per unit length. Thus it is essential that the neutron energy spectrum to be attenuated is known. In the past, wood has been discouraged as a shielding material because of its flammability. Recently, chemically treated wood that is nearly completely fireproof has become available, but it is not clear that the flammability problem has been solved with complete satisfaction. For example, questions have been raised by reports of a reduction in structural strength of such treated wood products.

Paraffin historically has been used for neutron shielding but has been spurned in recent years because of the fire hazard. Under some conditions it can be used if it is packaged in metal containers. Recently, paraffin treated with fire retardant additives has become available. It is still subject to "plastic" flow problems.

-iron

A relatively high density in conjunction with its low cost make iron an attractive shielding material. Caution is required because the density can vary widely from a low of 7.0 for low grade cast iron to a high value of 7.8 g·cm⁻³ for some steels. (The "textbook" value of 7.9 g·cm⁻³ is almost never attained in the bulk quantities necessary for radiation shielding).

Because of its nonmagnetic properties, stainless steel is often used as part of accelerator components. Because of concerns about radioactivation, a knowledge of the elemental composition of various alloys can sometimes be of interest.

Iron has a very important deficiency as a neutron shield; this will be discussed a bit later.

-high atomic number materials

The materials in this category are valuable because of their high atomic number, especially where the shielding of photons is important. The most obvious material in this category is lead. It has high density (11.3 g·cm⁻³) and is resistant to corrosion. Pure lead, as is well-known, has major drawbacks because of its poor structural characteristics and low melting point (327.4 °C). It is usually best used when it can be laminated to some other, more structurally stable, material. Some alloys represent improvements on the structural properties.

It is often available as an additive to other materials in order to improve their capacity for shielding photons. Fabric blankets containing shredded lead can be effectively used to shield radioactivated components to minimize exposures associated with accelerator maintenance activities. The high chemical toxicity of lead requires care in its fabrication and handling to properly protect personnel.

Tungsten is an excellent, but relatively expensive, shielding material. Its high density ($19.3 \text{ g}\cdot\text{cm}^{-3}$) and high melting temperature (3410°C) make it extremely useful as a component in photon shields and in beam collimators.

Uranium is a somewhat attractive shielding material, most often in its "depleted" form in which ^{235}U is removed from the dominant ^{238}U down to some residual fraction (usually 0.2 %) much lower than the natural value of 0.72 %. Its high density ($19.0 \text{ g}\cdot\text{cm}^{-3}$) and relatively high melting point (1133°C) are positive attributes, especially in places where space efficiency is a concern. It is obviously not a good choice of material in environments having a high neutron flux density. In the depleted form, it is relatively safe, but if combined with hydrogenous materials, criticality should be considered for the specific material and geometric arrangement to be employed. Even in the absence of hydrogen, thermal neutrons under certain conditions can result in the possibility of criticality.

Major drawbacks are the material properties. It has a large anisotropic thermal expansion coefficient and also readily oxidizes when exposed to air (especially humid air). The oxide is readily removable and presents a significant internal exposure hazard. Prevention of oxidation by sealing it with epoxy or paint meets with only limited success due eventual embrittlement and chipping accelerated by radiation damage. Sealed containers filled with dry air seems to be the best storage solution to limit oxide formation. Small chips of this element are also pyrophoric, complicating machining-type processes by posing yet another safety hazard.

-beryllium, aluminum, and zirconium

These three materials find considerable usage as accelerator components because of various properties. Beryllium is often used as a target material in intense beams because of its resistance to thermal effects (especially when in the form of the oxide, BeO). It has been used at high energy accelerators in relatively large quantities as a "filter" to enrich one particle type at the expense of another. A serious concern is the extreme chemical toxicity of the metal and its compounds, which makes it difficult to fabricate. Aluminum is used as an accelerator component because of its nonmagnetic properties and its resistance to corrosion. It is not an effective shield against neutrons. Zirconium has a very small thermal neutron capture cross section and very good thermal properties. It is therefore not a good neutron absorber but has been found to be useful in beam-handling component material in some situations.

Measured Neutron Energy Spectra Outside of Shields

In the most simple approximation, outside of thick shields of soil or concrete that contain some hydrogen content (usually in the form of H_2O), accelerator neutron shields can most generally said to be a "1/E" spectrum with the energies extending from those of thermal neutrons ($\langle E_n \rangle = 0.025 \text{ eV}$) up to the energy of the incident protons. In this approximation, the spectrum is given as:

$$\frac{d\phi(E)}{dE} = k \frac{1}{E} \quad (3.36)$$

where k is a normalizing constant.

N. Rohrig (Ro83) observed from this that it is more convenient to plot such spectra as flux per logarithmic energy interval by simply plotting $E\phi(E)$;

$$\frac{d\phi(E)}{d[\ln(E)]} = E\phi(E) . \quad (3.37)$$

In the terminology of textbooks on "neutron physics" (i.e., a terminology that is somewhat obscure to particle and nuclear physicists), this is also called a "lethargy" plot. This, effectively, suppresses the $1/E$ dependence seen in typical neutron energy spectra.

Detailed features of the geometry involved can produce peaks in the neutron energy spectrum. Some of these features have been discussed in (Pa73), (Nc96), (Th88), (El86), and (Co88). These peaks are typically encountered in the few MeV region. Figures 3.24, 3.25, and 3.26 are plots of neutron spectra and sketches of the shielding geometry involved taken from (Co88). These are typical of the spectra found at high energy proton accelerators. These results were obtained using the Bonner sphere technique discussed in more detail in Chapter 6. Spectrum C is particularly interesting because its shape was demonstrated to be essentially independent of proton energy over the range of 150 to 900 GeV (McC88).

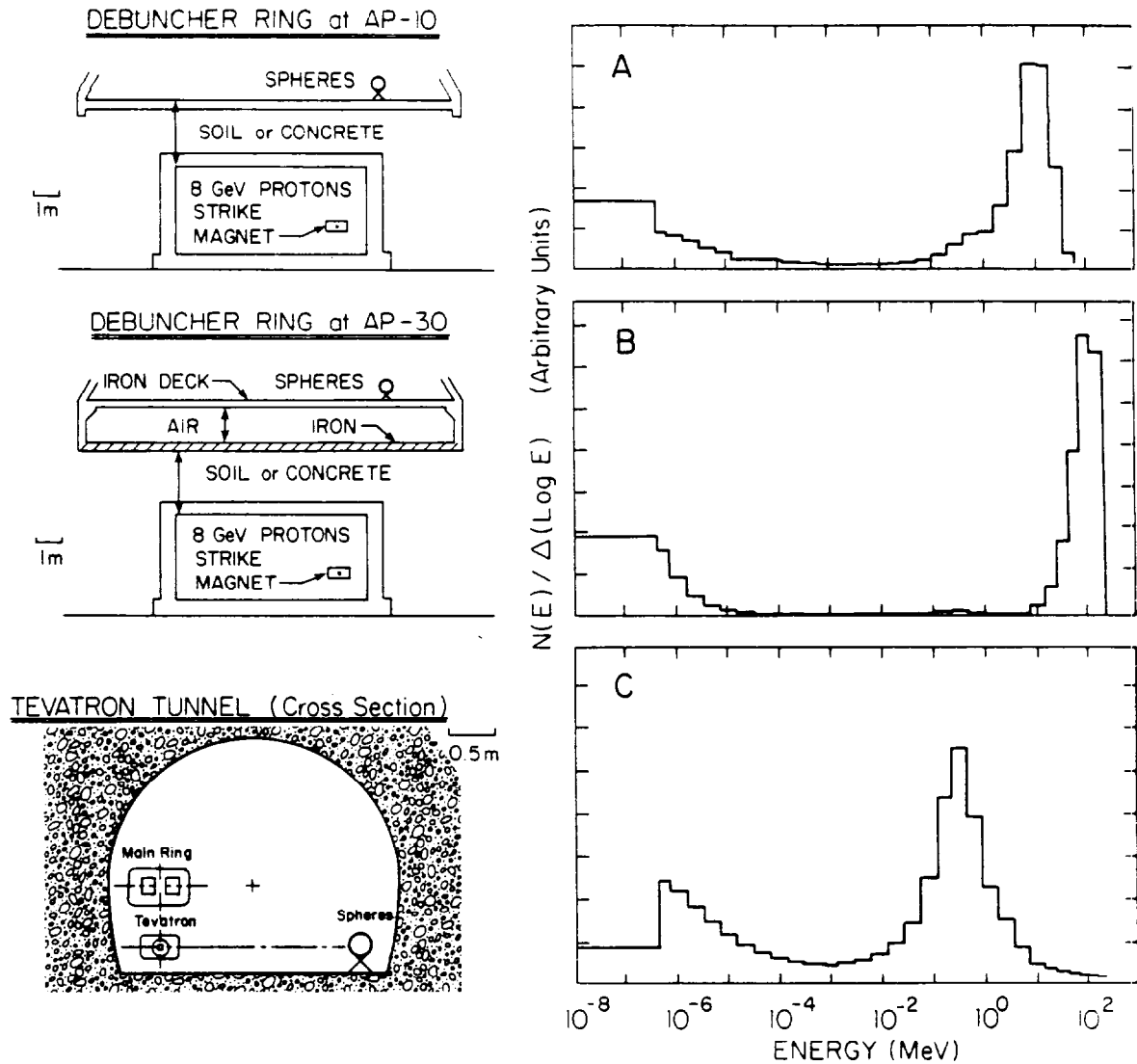


Fig. 3.24 Shielding geometries (left) and corresponding unfolded neutron energy spectra (right) for situations A, B, and C described in (Co88). The ordinate is a linear scale in arbitrary units of fluence per logarithmic energy interval. Spectrum A arose from 8 GeV protons being targeted on a magnet in the Fermilab Debuncher storage ring normally used to store antiprotons for the Fermilab colliding beams physics program. The Bonner spheres were located external to a 671 g cm^{-2} shield of earth and concrete. Spectrum B resulted from 8 GeV protons being targeted on a magnet in a different part of the same Debuncher storage ring. There spheres were located external to a 402 g cm^{-2} shield of earth and concrete plus some iron just below the spheres. Spectrum C was obtained inside the Tevatron tunnel with the spheres located on the wall opposite the accelerator elements. Data were collected using an array of 8 detectors operated primarily by personnel from the Lawrence Berkeley Laboratory. Neutrons were produced from 800 GeV protons interacting with residual gas in the Tevatron vacuum chamber during circulating beam conditions. [Reproduced from (Co88) and references cited therein.]

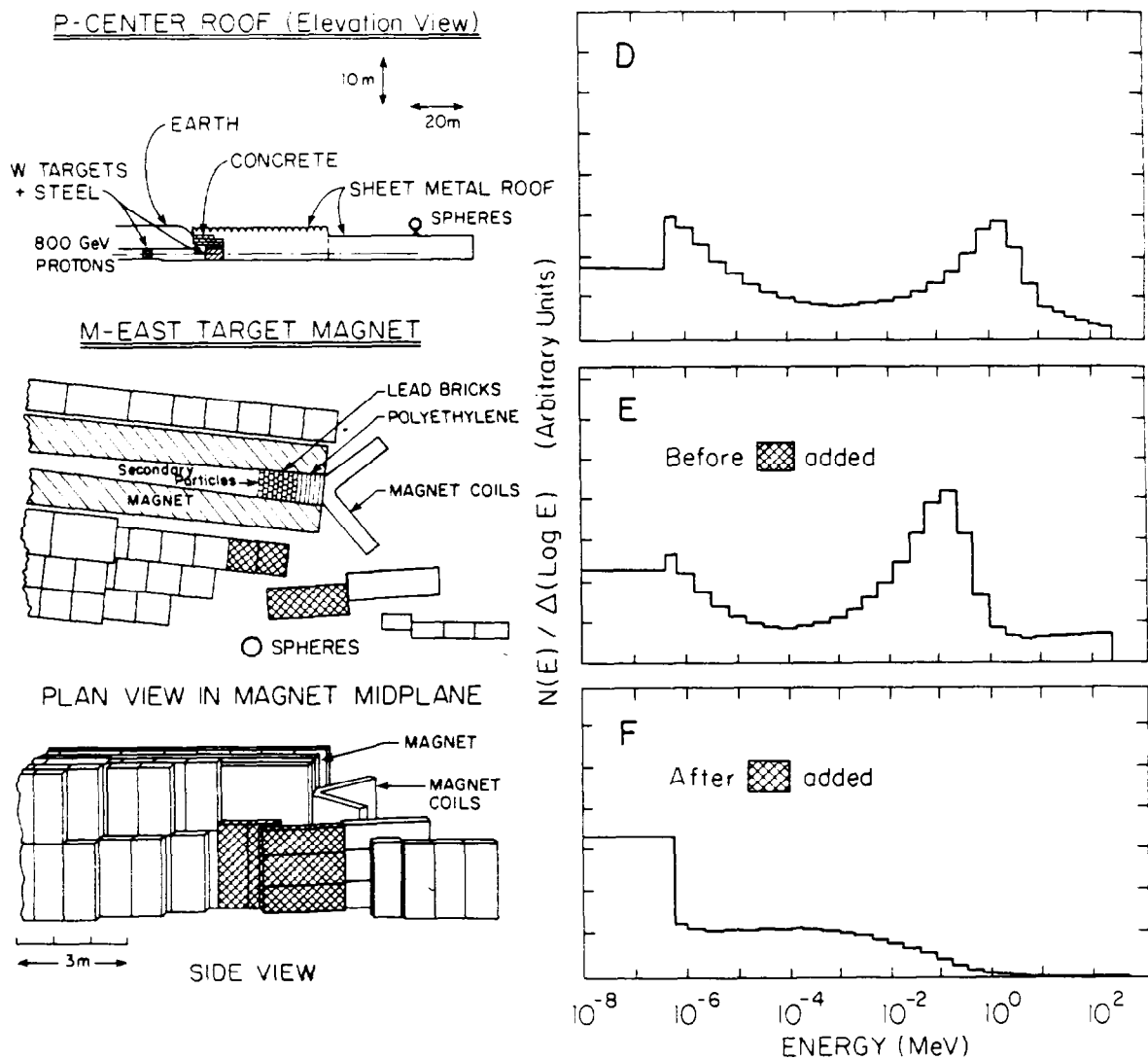


Fig. 3.25 Shielding geometries (left) and corresponding unfolded neutron energy spectra (right) for situations D, E, and F described in (Co88). The ordinate is a linear scale in arbitrary units of fluence per logarithmic energy interval. Spectrum D was obtained relatively far downstream of a large target and beam dump system struck by 800 GeV protons and shielded by iron and concrete. Spectra E and F were obtained laterally to a large electromagnet which contained a beam dump within its gap. This beam dump was struck by 800 GeV protons. For E, the spheres viewed bare iron return yoke while for F the return yoke viewed by the spheres was covered by additional concrete shielding, at least 91.4 cm thick, as shown. [Reproduced from (Co88) and references cited therein.]

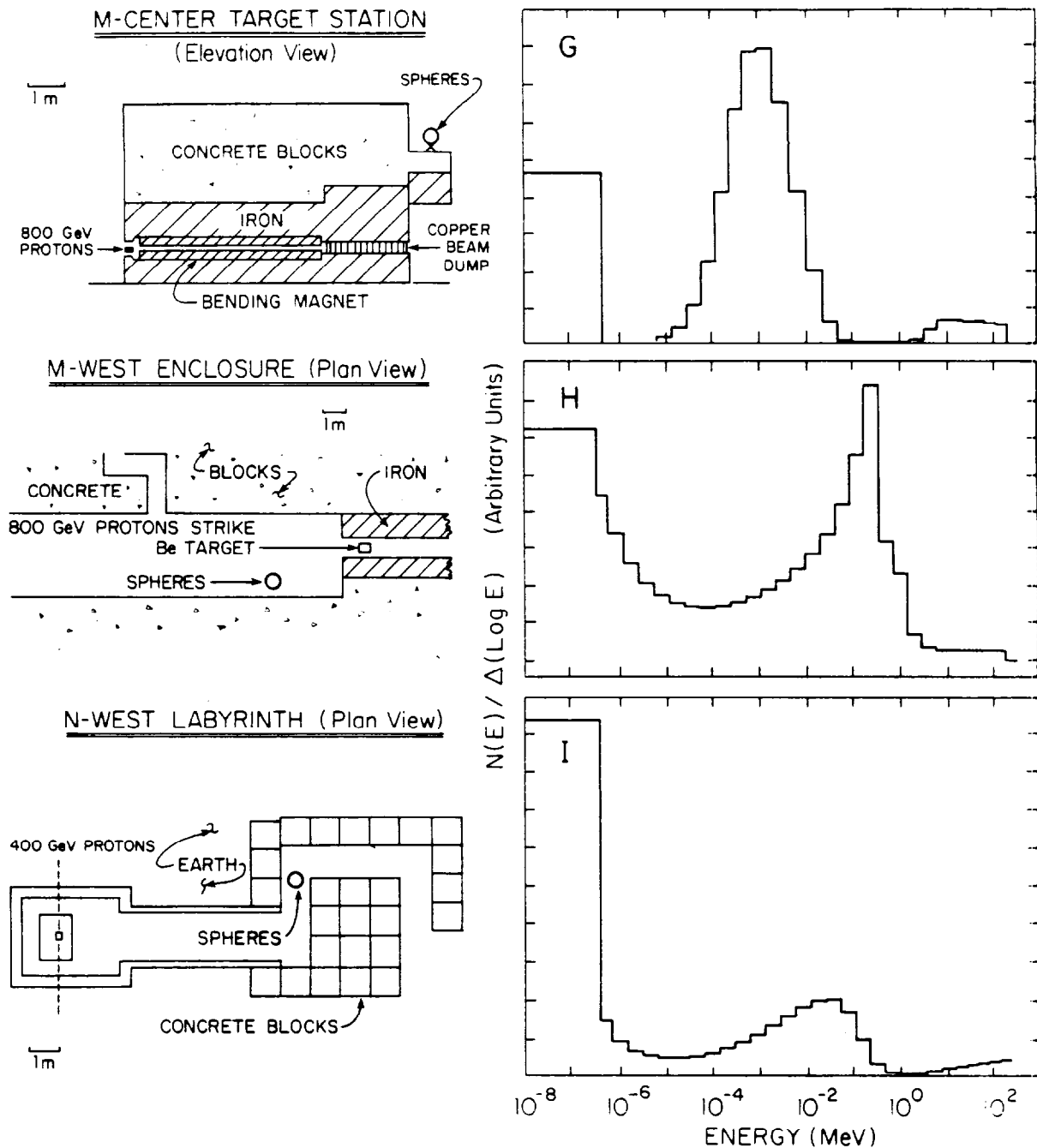


Fig. 3.26 Shielding geometries (left) and corresponding unfolded neutron energy spectra (right) for situations G, H, and I described in (Co88). The ordinate is a linear scale in arbitrary units of fluence per logarithmic energy interval. **Spectrum G** was obtained on top of the downstream end of a beam dump and target assembly involving 800 GeV protons incident on a target followed by bending magnets and a beam dump. The entire assembly was shielded by an inner layer of iron and an outer layer of concrete in the form of large (≈ 91.4 cm thick) blocks. **Spectrum H** was obtained in a beam enclosure in which 800 GeV protons struck a target in an iron cave downstream from the spheres. The detectors thus view "backscatter" from this target. **Spectrum I** was obtained in the second "leg" of labyrinth (see Chapter 4). The neutrons were produced by 400 GeV protons striking an aluminum target inside a large pipe beneath the floor of the main enclosure. [Reproduced from (Co88) and references cited therein.]

One of these peaks which commonly appear in such spectra is particularly important. As discovered by Alsmiller and Barish (Al73), iron has a major deficiency as a shield for fast neutrons. Containing no hydrogen, the primary attenuation mechanism for fast neutrons is by inelastic scattering from the iron nuclei. At energies below the first excited state of any nucleus, inelastic scattering becomes impossible and elastic scattering becomes the only removal process. As will be seen in Chapter 6, elastic scattering is a very inefficient means of energy removal for neutrons scattering off the much more massive iron nucleus. Billiard balls scattering off of bowling balls comes to mind as an analogy. It is intuitive that billiard balls scattering off other billiard balls of equal mass provides for much more efficient energy transfer. Likewise, neutrons scattered by the "free" protons in hydrogenous materials is much more efficient in terms of energy transfer than is the elastic scattering of neutrons from iron nuclei.

The first excited state of ^{56}Fe [the dominant (92%) isotope in natural iron] is at 847 keV. This has the consequence that the neutrons build up below this energy because of the inefficiency of the transfer of energy by means of elastic scattering. Thus neutrons above 847 keV in a given spectrum will be slowed by inelastic scattering only to build up in this region. Amplifying this effect when one considers the dose equivalent external to such shields is the fact that the quality factor for neutrons as a function of energy also has its maximum value at about 700 keV. Thus, pure iron shields are rather ineffective in attenuating neutrons in this energy region.

Spectra E and F in Fig. 3.25 illustrate this phenomena concerning iron shielding. They were both measured at about $\theta = 90^\circ$ from a beam dump struck by secondary particles due to 800 GeV proton interactions far upstream of the beam dump (Co88). One of the spectra is for a bare iron shield while the other is after the iron was covered by a 91.4 cm thick layer of concrete. For the bare iron the dose equivalent rate external to the shield was over 40 times that measured after the concrete was installed. This factor is far in excess of the approximate factor of 10 expected from simple attenuation of the equilibrium cascade neutron spectrum. The concrete also reduced the average quality factor from 5.4 to 2.8. In general, an iron shield "capped" or "backed" by such a concrete shield will be an efficient use of space. It has been determined that 60 cm of concrete is the most efficient thickness to use for this purpose [(Yu83) and (Za87)]. Shielding properties of other elements near iron (chiefly copper and nickel) in the periodic table are comparable.

Finally, one must be concerned with the per cent of fluence and per cent of dose equivalent in specific energy bins. This can affect the potential to produce radioactivity and also guides the designer of shielding. Tables 3.10 and 3.11 taken from (Co88) give these properties for the nine spectra displayed in Figs. 3.24, 3.25, and 3.26. Fig. 3.27 from (Va75) is a plot of cumulative values of the same quantities for 1000 GeV protons incident on the face of a thick cylindrical concrete shield. As determined by Van Ginneken and Awschalom (Va75), the dependence upon incident proton energy of the distributions of fluence and dose equivalent is slight.

Chapter 3 Shielding of Proton and Ion Accelerators

Table 3.10 Percent Fluence in Specific Energy Bins for Unfolded Neutron Spectra [Reproduced from (Co88).]

Spectrum-> Energy	A	B	C	D	E	F	G	H	I
< 1.5 eV	31.5	42	19.5	29	28	55	33.5	42	71
0.0015-100 keV	12.5	4.5	36	39	46	43	62.1	36.2	24
0.1-2 MeV	8.5	1	36	19.5	17.5	2	0	19.4	2
2-25 MeV	40.5	2.5	7	10	4.5	0.1	2.1	1.5	1
> 25 MeV	7	50	1.5	2.5	4	0	2.3	0.9	1.5

Table 3.11 Percent of Dose Equivalent in Specific Energy Bins for Unfolded Neutron Spectra Along with Average Quality Factor [Reproduced from (Co88).]

Spectrum-> Energy	A	B	C	D	E	F	G	H	I
< 1.5 eV	1.5	2	2	3	4	41.5	12.5	9	32
0.0015-100 keV	0.5	0.2	6	6	11.5	37	22.3	11.9	16
0.1-2 MeV	9	0.4	58.5	41	35	17	0.1	59.8	9
2-25 MeV	75	4	26	38	24	3.5	28	11.5	13
> 25 MeV	14	93.5	7.5	12	25	1	37.1	7.9	30
Average Q.F.	5.8	4.2	6.9	6.2	5.4	2.5	3.4	5.7	3.1

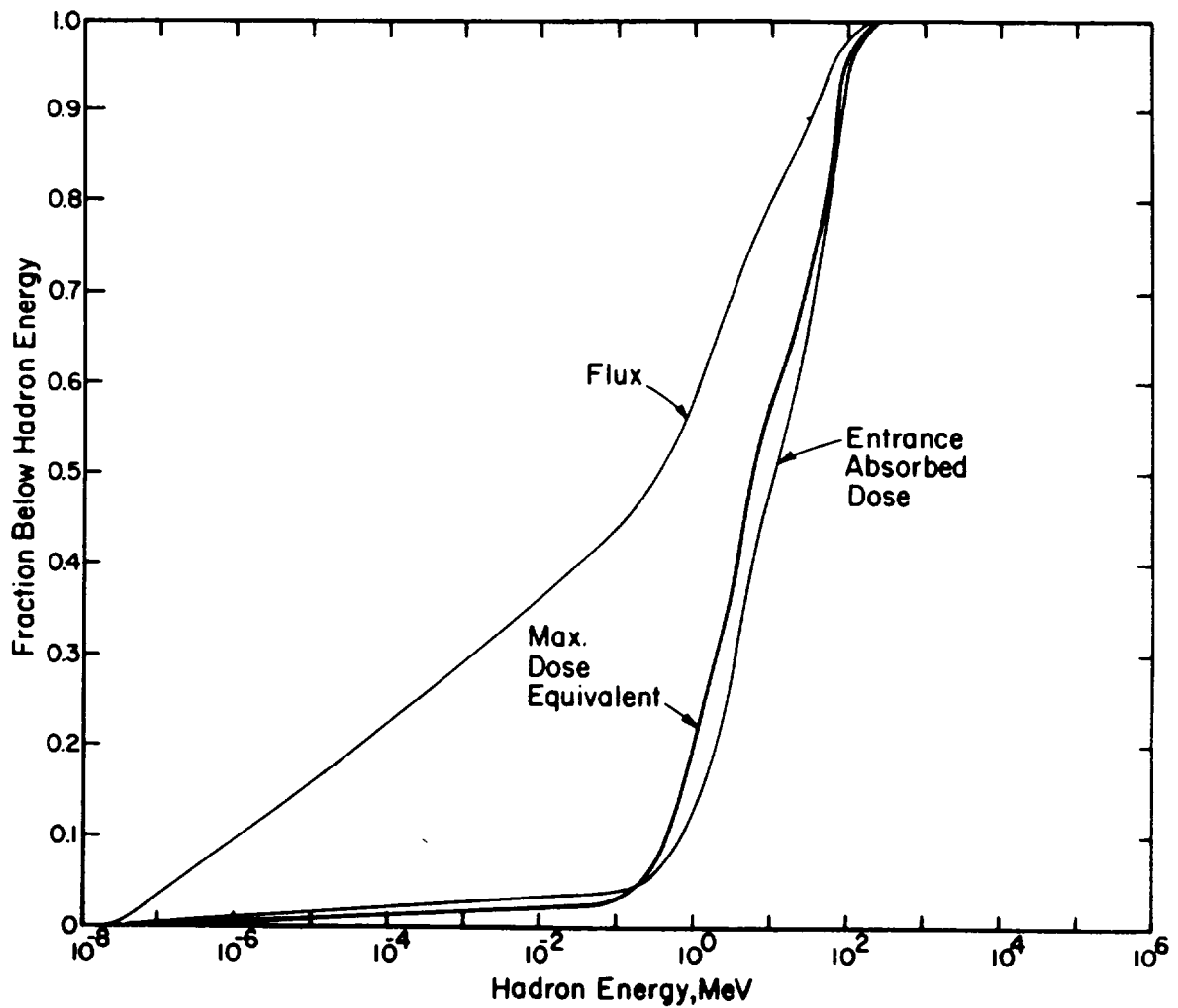


Fig. 3.27 Fraction of the omnidirectional flux, entrance absorbed dose, and maximum dose equivalent below hadron kinetic energy on abscissa (in MeV) for the region between zero and 450 cm depth and between 300 cm and 750 cm radius for 1000 GeV/c protons incident on the face of a solid concrete cylinder. [Reproduced from (Va75).]

References

- (Aa86) P. A. Aarnio, A. Fassò, H. J. Moehring, J. Ranft, G. R. Stevenson, "FLUKA86 users guide", CERN Divisional Report TIS-RP/168 (1986).
- (Al73) R. G. Alsmiller, Jr, and J. Barish, "Shielding against the neutrons produced when 400 Mev electrons are incident on a thick copper target", *Particle Accelerators* 5 (1973) 155.
- (Al75) R. G. Alsmiller, R. T. Santoro,, and J. Barish, "Shielding calculations for a 200 MeV proton accelerator and comparisons with experimental data", *Particle Accelerators* 7 (1975) 1-7.
- (Ar80) T. W. Armstrong, "The HETC hadronic cascade code", in *Computer Techniques in Radiation Transport and Dosimetry*, W. R. Nelson and T. M. Jenkins, editors (Plenum Press, New York and London, 1980), pp. 373-375.
- (Ch84) A. B. Chilton, J. K. Shultis, and R. E. Faw, *Principles of Radiation Shielding* (Prentice-Hall, Englewood Cliffs, New Jersey, 1984).
- (Cl71) F. H. Clark, "Shielding Data, Appendix E, in *Protection Against Neutron Radiation* , NCRP Report No. 39 (Washington, DC, 1971).
- (Co82) J. D. Cossairt, N. V. Mokhov, and C. T. Murphy, "Absorbed dose measurements external to thick shielding at a high energy proton accelerator: Comparison with Monte-Carlo calculations, *Nucl. Instr. and Meth.* 197 (1982) 465.
- (Co85) J. D. Cossairt, S. W. Butala, and M. A. Gerardi, "Absorbed dose measurements at an 800 GeV proton accelerator, comparison with Monte-Carlo calculations, *Nucl. Instr. and Meth.*, A238 (1985) 504.
- (Co88) J. D. Cossairt, A. J. Elwyn, W. S. Freeman, W. C. Salsbury, and P. M. Yurista, "Measurement of neutrons in enclosures and outside of shielding at the Tevatron", *Fermilab-Conf-88/106* (1988) also in *Proceedings of the 22nd Midyear Meeting of the Health Physics; Topical Meeting on Instrumentation*, San Antonio, TX, December, 1988, pp. 190-199.
- (Co89a) J. D. Cossairt, A. J. Elwyn, W. S. Freeman, and S. W. Butala, "A study of the transport of high energy muons through a soil shield at the Tevatron", *Nucl. Instr. and Meth.* A276 (1989) 78.
- (Co89b) J. D. Cossairt, A. J. Elwyn, and W. S. Freeman, "A study of the production and transport of high energy muons through a soil shield at the Tevatron", *Nucl. Instr. and Meth.* A276 (1989) 86.
- (El86) A. J. Elwyn and J. D. Cossairt, "A study of neutron leakage through an Fe shield at an accelerator", *Health Physics* 51 (1986) 723-735.
- (Em75) M. B. Emmett, ORNL Report-4972 (1975).
- (Ga85) T. A. Gabriel, "The high energy transport code HETC", Oak Ridge National Laboratory Report ORNL-TM-9727 (1985).
- (IC78) ICRU, "Basis Aspects of High-Energy Particle Interactions and Radiation Dosimetry", Report No. 28, Washington, DC, 1978.

Chapter 3 Shielding of Proton and Ion Accelerators

- (Ka84) A. N. Kalinovsky, N. V. Mokhov, and Yu P. Nikitin, *Penetration of High Energy Particles Through Matter* (Energoatomizdat, Moscow, USSR, 1984).
- (Li61) S. J. Lindenbaum, "Shielding of high energy accelerators", *Ann. Rev. Nucl. Sci.* **11** (1961) 213.
- (McC85) J. B. McCaslin, P. R. LaPlant, A. R. Smith, W. P. Swanson, and R. H. Thomas, "Neutron production by Ne and Si ions on a thick Cu target at 670 MeV/A with application to radiation protection," *IEEE Trans. on Nucl. Sci.* **NS-32**, No. 5 (1985) 3104.
- (McC87) J. B. McCaslin, W. P. Swanson, and R. H. Thomas, "Moyer model approximations for point and extended beam losses", *Nucl. Instr. and Meth.* **A256** (1987) 418-426.
- (McC88) J. B. McCaslin, R.-K. Sun, W. P. Swanson, J. D. Cossairt, A. J. Elwyn, W. S. Freeman, H. Jöstlein, C. D. Moore, P. M. Yurista, and D. E. Groom, "Radiation environment in the tunnel of a high-energy proton accelerator at energies near 1 TeV," Lawrence Berkeley Report LBL-24640 (1987), presented at the Seventh Annual Congress of the International Radiation Protection Association, Sydney, Australia, April, 1988.
- (Mo86) N. V. Mokhov and J. D. Cossairt, "A short review of Monte Carlo hadronic cascade calculations in the multi-TeV energy region", *Nucl. Instr. and Meth.* **A244** (1986) 349-355.
- (NC96) R. H. Thomas (chair), W. R. Casey, N. Rohrig, J. D. Cossairt, L. A. Slaback, K. O'Brien, G. B. Stapleton, and W. P. Swanson, National Council on Radiation Protection and Measurements (NCRP), NCRP Report 51 (Revised)--in preparation.
- (Pa73) H. W. Patterson and R. H. Thomas, *Accelerator Health Physics*, Academic Press, New York, 1973.
- (Ro76) J. T. Routti and R. H. Thomas, "Moyer integrals for estimating shielding of high-energy accelerators", *Nucl. Instr. and Meth.* **76** (1969) 157-163.
- (Ro83) N. Rohrig, "Plotting neutron fluence spectra, *Health Physics* **45** (1983) 817-818.
- (Sc90) H. Schopper (editor), A. Fassò, K. Goebel, M. Höfert, J. Ranft, and G. Stevenson, *Landolt-Börnstein Numerical Data and Functional Relationships in Science and Technology New Series; Group I: Nuclear and Particle Physics Volume II: Shielding Against High Energy Radiation* (O. Madelung, Editor in Chief, Springer-Verlag, Berlin, Heidelberg, 1990).
- (St82) G. R. Stevenson, L. Kuei-Lin, and R. H. Thomas, "Determination of transverse shielding for proton accelerators using the Moyer model", *Health Phys.* **43** (1982) 13-29.
- (St87) G. R. Stevenson, "Empirical parametrization of the shielding of end-stops at high-energy proton accelerators, CERN Divisional Report TIS-RP/183/CF (1987).
- (Su92) A. H. Sullivan, *A guide to radiation and radioactivity levels near high energy particle accelerators* (Nuclear Technology Publishing, Ashford, Kent, United Kingdom), 1992)
- (Te83) K. Tesch, "Comments on the transverse shielding of proton accelerators", *Health Phys.* **44** (1983) 79-82.
- (Te85) K. Tesch, "A simple estimation of the lateral shielding for proton accelerators in the energy range from 50 to 1000 MeV," *Rad. Prot. Dos.* **11** (1985) 165-172.
- (Th84) R. H. Thomas and S. V. Thomas, "Variation and regression analysis of Moyer model parameter data", *Health Phys.* **46** (1984) 954-957.

Chapter 3 Shielding of Proton and Ion Accelerators

- (Th88) R. H. Thomas and G. R. Stevenson, "Radiological Safety Aspects of the Operation of Proton Accelerators", Technical Report No. 283, IAEA, Vienna, 1988.
- (Va75) A. Van Ginneken and M. Awschalom, "High energy particle interactions in large targets: Volume I, hadronic cascades, shielding, and energy deposition", Fermilab (1975).
- (Va87) A. Van Ginneken, P. Yurista, and C. Yamaguchi, "Shielding calculations for multi-TeV hadron colliders, Fermilab Report FN-447 (1987).
- (Yu83) P. M. Yurista and J. D. Cossairt, "Concrete shielding exterior to iron," Fermilab Report TM-1204, Fermi National Accelerator Laboratory (1983).
- (Za87) J. M. Zazula, "Derivation of accelerator shielding parameters from adjoining high energy neutron transport calculations", in Theory and Practices in Radiation Protection and Shielding, Proceedings of the Radiation Protection and Shielding Division, American Nuclear Society, Knoxville, Tennessee, April 22-24, 1987, Vol 2, pp.434-443.

1. It is asserted that if the assumption is made that the limiting attenuation is simply geometric, with the nucleon radius equal to 1.2×10^{-13} cm, then $\rho\lambda_{\text{atten}} = 38A^{1/3}$ (g/cm²). Show this to be the case using the volume of a nucleus and nucleons along with the cross section.
2.
 - a) Use the Moyer Model to calculate the dose equivalent rate (mrem/hr) lateral ($\theta = 90^\circ$) to a magnet centered in a 1.5 m radius tunnel. The magnet is struck by 10^{12} protons at 100 GeV (per sec). The tunnel walls consist of 1/3 m concrete followed by soil having the same composition [$\rho(\text{concrete}) = 2.5$ g/cm³, $\rho(\text{soil}) = 2.0$ g/cm³]. Perform the same calculation for several thicknesses of soil out to 6 meters of soil radially. Do this for increments of 1 meter from 1 meter to 6 meters of soil.
 - b) Calculate the result if the same beam loss occurs over a 100 meter length of tunnel at the same soil thicknesses as in 2) (use the Tesch approximation). Approximately how many meters of beam loss does it take to cause 90% of the calculated dose equivalent rate at 6 m of lateral soil shield?
 - c) For the point loss in part a), at what value of θ does the maximum dose equivalent rate occur and what is its magnitude outside of 6 meters of soil shield? (Use successive approximations to solve.)
3. For the accelerator and beam delivery conditions of problem 2a, use the results of FLUKA calculations in Fig. 3.16 to determine the approximate dose equivalent rate outside of 1 meter of concrete shielding and compare with a result using the Moyer equation for point loss on a "magnet". Both calculations should be at the location of the dose equivalent maximum. Assume $\rho(\text{concrete}) = 2.5$ g/cm³. Why might there be an explainable disagreement between the two results?
4. Using the results of Monte-Carlo hadron calculations (FLUKA/CASIM) calculate, for solid shields of iron (cylinders), what longitudinal thickness of iron is needed to achieve the same hadron dose equivalent per proton on the beam axis as found at $R = 50$ cm at 10 GeV/c, 100 GeV/c, 1000 GeV/c and 10 TeV/c. Use the maximum value of $H(r = 50 \text{ cm})$. One may need to extrapolate calculations shown in Fig. 3.18.

5. In the Chapter 1, Fig. 1.30 we have calculations of neutron energy spectra for 200 MeV protons incident on various targets, including aluminum. In Fig. 3.12 of this chapter, calculations of dose equivalent values for concrete shielding surrounding aluminum targets @ $E_p = 200$ MeV are given. At shielding thicknesses approaching zero and at forward angles, are the two results in "sensible" (that is, approximate, agreement)? (Hint: "Integrate" crudely over the forward spectrum to obtain the fluence/proton and convert this fluence to dose equivalent.)
- a) Make the comparison for zero shield thickness and in the angular range $0 < \theta < 30^\circ$.
 - b) Now use the shielding calculations to obtain the dose equivalent rate (rem/h) due to a 1 μ A beam incident at 200 MeV on such a thick target at a distance of 4 m from the target with 0, 1, 2, & 3 m of intervening concrete shielding ($\rho = 2.5\text{g/cm}^3$) for $\theta = 15^\circ$ and $\theta = 75^\circ$. (Hint: Use the center of the angular bins.)
6. Assume that a target is struck by 100 GeV protons and that a 10 m long decay space exists for π and K decay. Use the curves in Fig. 3.21 to crudely estimate the muon flux density and dose equivalent rates (mrem/h) at $\theta = 0^\circ$ if 10^{12} p/s are targeted in this manner at 1 km away if:
- a) there is no shielding present (neglect air scattering and in-scattering from the ground). (Hint: The muon yield for this decay space will scale with the length of the decay space.)
 - b) there is 100 meters of intervening shielding of earth ($\rho = 2\text{ g/cm}^3$) (Hint: use Fig. 1.22 range-energy curves to determine the mean energy of muons which will penetrate this much shielding). Neglect multiple scattering and range-straggling.
 - c) If the beam operates for 4000 h/yr, is 100 mrem/yr exceeded? Will multiple scattering increase or decrease this dose equivalent? (Answer both questions for the soil shielded case only.)
 - d) Repeat Part b) of the same calculation using Sullivan's semi-empirical approach. If the disagreement between the results obtained using the two methods is large, please suggest an explanation of a possible cause of the difference.

Chapter 4 Low Energy Prompt Radiation Phenomena

In this chapter two special considerations pertinent to nearly all accelerators are discussed. These are the phenomena of the transmission of photons and neutrons by penetrations and of neutron skyshine. It will be shown that these phenomena are nearly independent of incident particle type and energy. Methods for taking proper account of these two phenomena in the design of accelerator shielding are discussed in detail.

I. Introduction

Accelerators of sufficient energy to produce neutrons copiously (either ion or electron accelerators) exhibit two phenomena involving low energy neutrons which must be addressed. These are the transmission of neutrons by penetrations and the control/prevention of "skyshine". In both cases, the neutrons involved are generally of low energy (compared to the beam particles) and the phenomena are also rather independent of the beam particle energy.

All accelerators evidence the need to control the transmission of neutrons by penetrations since all accelerators have access-ways to permit entry of personnel and equipment as well as cable penetrations. Concerning skyshine, while it is "preventable" through the application of sufficient roof shielding, all major accelerators constructed to date (at least the large ones!) have encountered this problem at some point due to "oversights" or the need to accommodate modifications in the accelerator design or the associated experimental program.

II. Transmission of photons and neutrons by penetrations *[This material largely follows (NC77), (Sc90), and (Th88).]*

Personnel access penetrations will typically have cross-sectional dimensions of 1 meter by 2 meters (door-sized) while utility ducts will generally be much smaller, typically no larger than 0.2 by 0.2 m. Often the utility penetrations are partially filled with cables and other items, and even cooling water in pipes.

Two general rules are advised for such penetrations:

It is an unwise practice to arrange any penetration so that a particle or photon beam is aimed directly toward it. Therefore, one is always primarily transporting *scattered* radiation through the penetrations.

The sum of the wall thickness between the source and the "outside" should be equivalent to that which would be required if the labyrinth were not present.

Before describing the details of penetration design as such, one should review some simple parameterizations of the reflections of photons and neutrons. Photons are being considered here simultaneously because their simple treatment can usefully be done with the same methods, with appropriate **albedo** parameters. These coefficients have applications more general than merely the design of penetrations. They represent the ability of solid materials to "reflect" particles.

Figs. 4.1 and 4.2 adapted from the results of Refs. (NC77), (Ch63), (Ch64), (Ch65a), and (Ch65b) give the reflection coefficients α_x and α_n for monoenergetic photons and neutrons (respectively) incident on flat surfaces of infinite dimensions of concrete, iron, and lead plotted as functions of energy for various conditions of incidence. As is obvious from these curves, the albedo of neutrons is typically larger and somewhat less strongly dependent on energy than is that of photons.

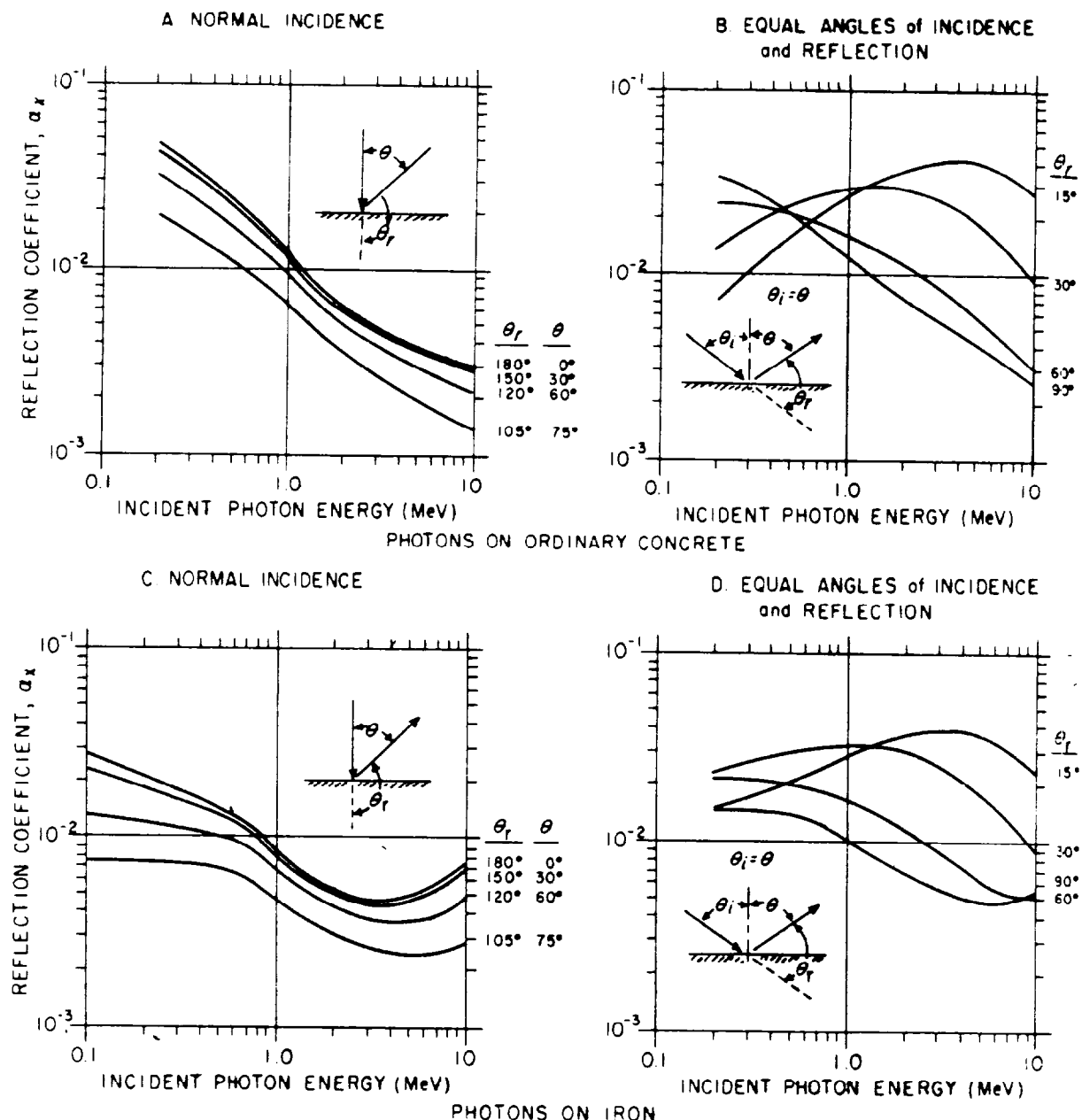


Fig. 4.1 Reflection coefficients, α_x , for monoenergetic photons incident on ordinary concrete, iron, and lead as a function of incident photon energy, for several angles of reflection assuming normal incidence and for equal angles of incidence and reflection. Values are given for ordinary concrete and iron, based on existing available information, both theoretical and experimental. For photon energies higher than 10 MeV, the use of the 10 MeV values of α_x is expected to be conservative. Values of α_x for photons incident on lead are not as readily calculable but a conservative upper limit is 5×10^{-3} for any energy and scattering angle. [Adapted from (NC77) and references cited therein.]

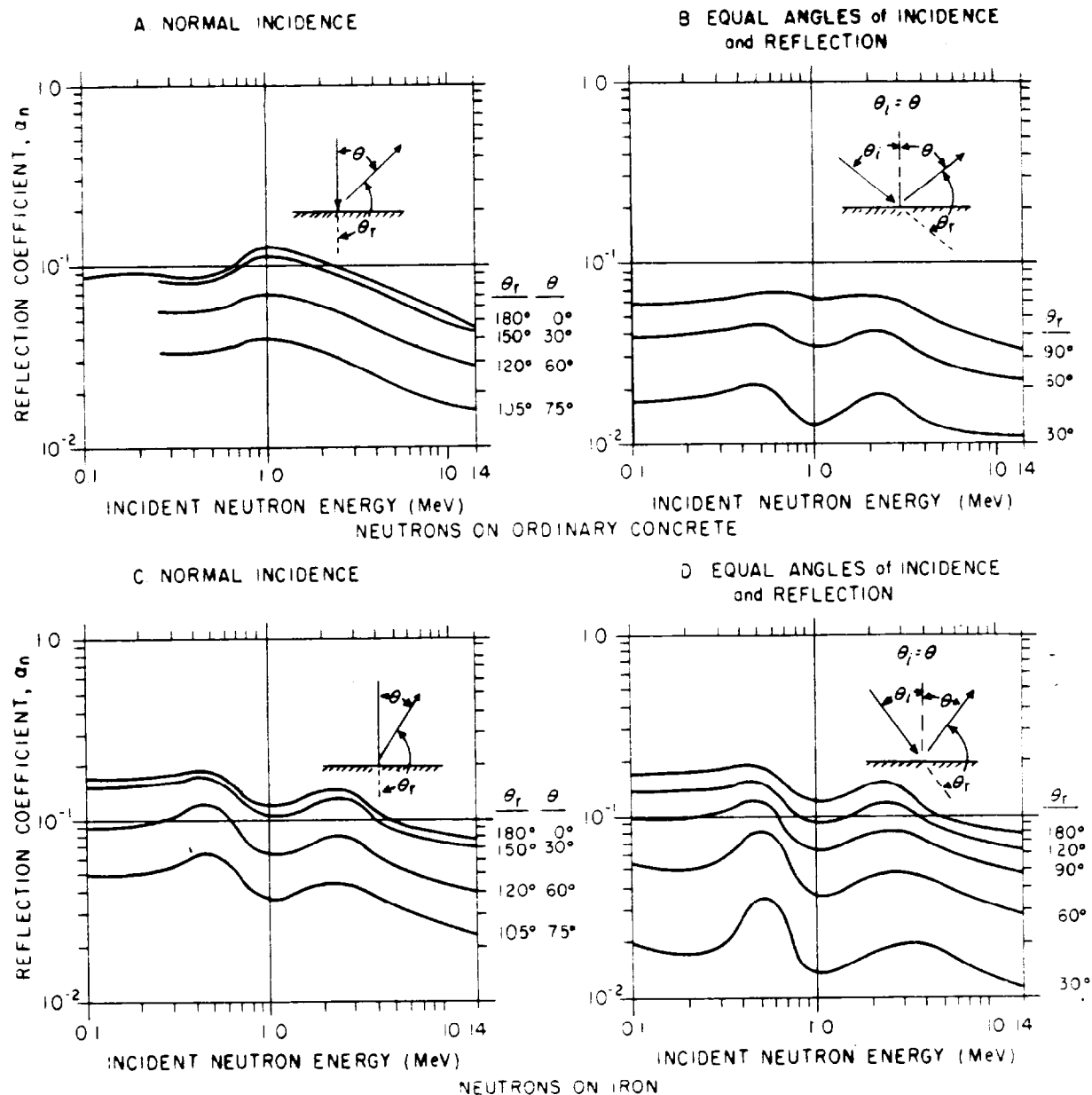


Fig. 4.2 Reflection coefficients, α_n , for monoenergetic neutrons incident on ordinary concrete, iron, and lead as a function of incident neutron energy, for several angles of reflection assuming normal incidence and for equal angles of incidence and reflection. Values of α_n are given for ordinary concrete and iron, based on existing available information, both theoretical and experimental. Values of α_n for neutrons incident on lead are approximately an order of magnitude larger than those given above. [Adapted from (NC77) and references cited therein.]

Photons

A particular application of these coefficients to the design of labyrinths is given here to illustrate the method using these albedo curves. Figure 4.3 taken from (NC77) shows an example of a labyrinth providing access to a collimated **photon** source of some known dose equivalent (or dose equivalent rate), H_0 , at one meter. In general, some knowledge of the photon energy spectrum at this location is also needed. Such a photon "beam" is relevant to the subject of this text because, for example, it could arise from the targetry of a beam from an electron accelerator.

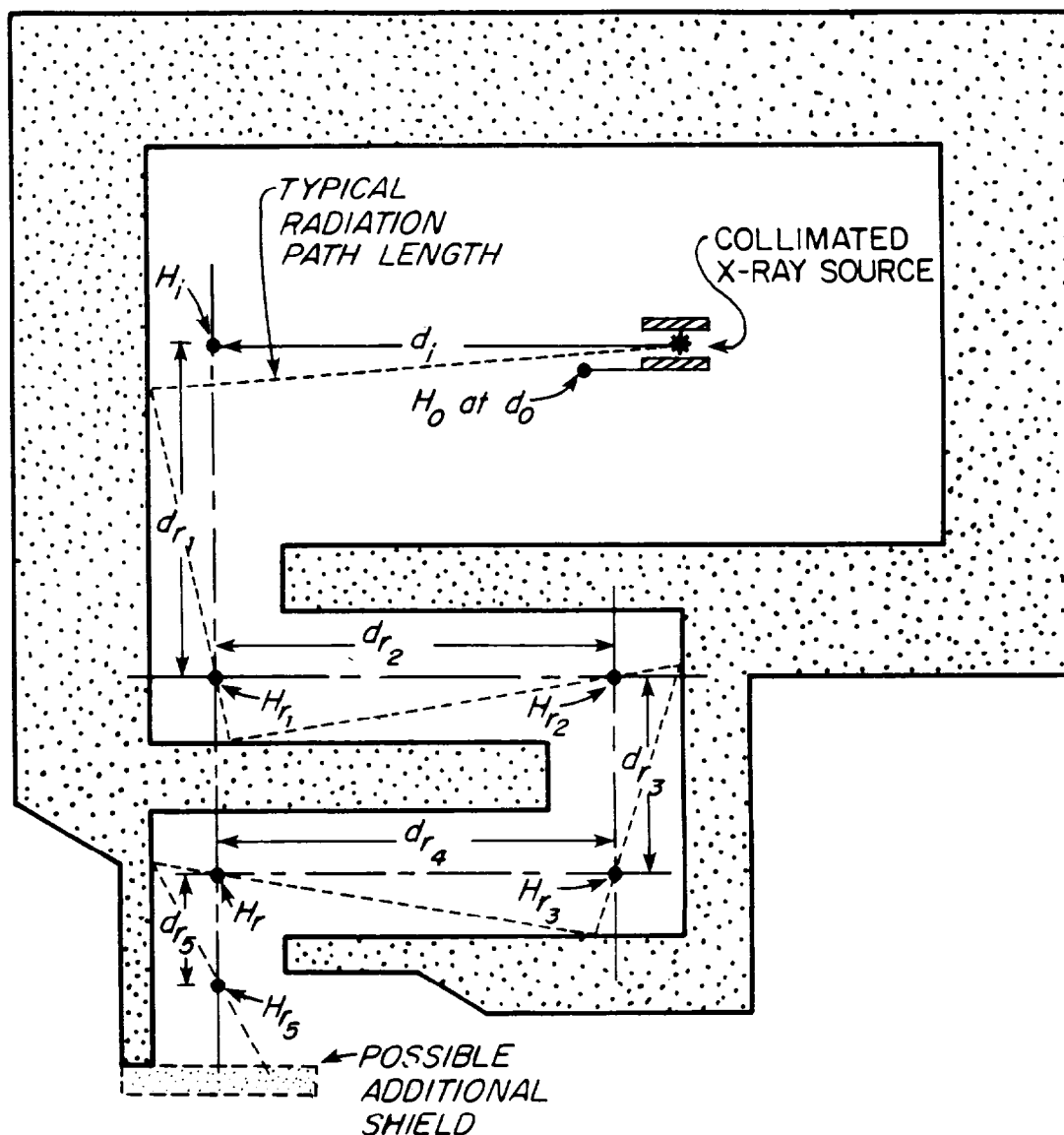


Fig. 4.3 Generalized labyrinth design illustrating successive reflections of photons from a collimated source through the maze. The source could just as well originate from an electron beam incident from the right side of the figure on a target located at the point in space labeled "collimated x-ray source". The various path lengths can be approximated by a sequence of centerline distances, as shown in the diagram. [Reproduced from (NC77).]

With the reflection coefficients α_x , one can use the following formula to obtain a conservative estimate of the dose equivalent (or dose equivalent rate), H_{rj} , after j sections (not counting the initial path length to the wall, d_i) of the maze:

$$H_{rj} = \frac{H_0 \alpha_i A_i \prod_{k=1}^j \alpha_k A_k}{d_i^2 \prod_{k=1}^j d_{rk}^2} \quad j \geq 1. \quad (4.1)$$

In this formula, the coefficient α_i is selected to be representative of the photon energy while A_i estimates the cross sectional area of the wall struck by the initial photons evaluated by projecting the beam cross-sectional area to the wall. For successive legs, taking the value of α appropriate for 0.5 MeV photons is often considered to be a conservative approach. This is substantiated physically because, if E_0 is the initial photon energy in MeV, the photon energy, E_{scatt} , following Compton scattering is given by:

$$E_{scatt} = \frac{E_0}{1 + (E_0/0.511)(1 - \cos \theta)} \quad (\text{MeV}). \quad (4.2)$$

Thus, E_{scatt} has a maximum value after a scatter of 90° of 0.511 MeV for $E_0/0.511 > 1$.

A_k , then, is the cross-sectional area of the k^{th} leg of the maze. If the maze is uniform with cross section A , and has j legs, then the product in the numerator is simply raised to the j^{th} power; $(\alpha A)^j$. Otherwise individual factors for each leg must be used in place of the quantity taken to the j^{th} power. In the denominator, the distances are just those defined in the figure above and, of course, represent the inverse-square law dependence. This formula is more conservative for photon energies exceeding 10 MeV, but at the higher energies the uncertainties are larger. The above formula is probably most accurate if the ratios $d_{rk}/(A_k)^{1/2}$ lie between 2 and 6.

Neutrons

Unfortunately, complications in the transport of **neutrons** discourage the use of a similar formula. The radiation source (or potential radiation source for situations of concern from the standpoint of accidental beam losses) should be evaluated according to the methods described previously. The calculation of the attenuation of penetrations is a difficult one to do in great theoretical detail.

Typical methods employed involve the use of the results of calculations made by sophisticated Monte-Carlo codes. These can be used for both curved and rectilinear labyrinths with the primary practical experience being with the latter type. In this section, the results of such work will be presented in order to give the reader useful information in the evaluation of such penetrations.

An overwhelming conclusion of the body of existing data is that the bombarding particle energy has very little effect upon the attenuation of a labyrinth viewing a source of beam loss other than the increased total yield of "source" neutrons as a function of incident energy and ion type. One can thus estimate the dose, dose equivalent, or neutron fluence at the exit of a labyrinth by using attenuation estimates in conjunction with an estimate of the neutron fluence or dose equivalent at the entrance of the penetration into the beam enclosure. This "factorization" approximation

Chapter 4 Low Energy Prompt Radiation Phenomena

allows attenuation measurements and calculations obtained at proton accelerators to be of rather general utility.

Another general "rule of thumb" is that labyrinth attenuations of neutrons scale with a unit length equal to the square root of its cross-sectional area provided that the height to width ratio does not vary greatly outside of the range 0.5 to 2.0 (Th88).

For penetrations exposed to targets struck by hadrons, we first consider straight penetrations viewing a point of beam loss at 90° to the incident beam. Figures 4.4 and 4.5 taken from (Gi69) show measurements of the relative transmission of an exceptionally long straight tunnel of dimensions 2.8 m high by 1.8 m wide and 100 m long. 14 GeV protons were incident on a target providing a good "point source" 3.2 m from the tunnel entrance. Various activation detectors having different energy thresholds made it possible to obtain some information about the neutron energy spectrum. The experimental conditions did not allow an absolute normalization to beam loss.

Table 4.1 taken from (Th88) gives the thresholds of various reactions used in the measurement summarized in Figs. 4.4 and 4.5 where the number of events above the reaction threshold is used as an indicator of the energy spectrum:

Table 4.1 Detectors and their characteristics as used in the measurements summarized in Figs. 4.4 and 4.5. [Reproduced from (Th88).]

Detector	Reaction	Energy range (MeV)
Bare gold foils	$^{197}\text{Au}(n,\gamma)^{198}\text{Au}$	thermal
Large bare indium foils	$^{115}\text{In}(n,\gamma)^{116}\text{In}^m$	thermal
Moderated gold foils	$^{197}\text{Au}(n,\gamma)^{198}\text{Au}$	0.02 to 20
Kodak Type-B neutron films	Proton recoil	0.5 to 25
Sulphur	$^{32}\text{S}(n,p)^{32}\text{p}$	3 to 25
Aluminium	$^{27}\text{Al}(n,\alpha)^{24}\text{Na}$	6 to 25
Plastic scintillator	$^{12}\text{C}(n,2n)^{11}\text{C}$	> 20
Beta/gamma film and LiF TLD	Gamma and charged particles	

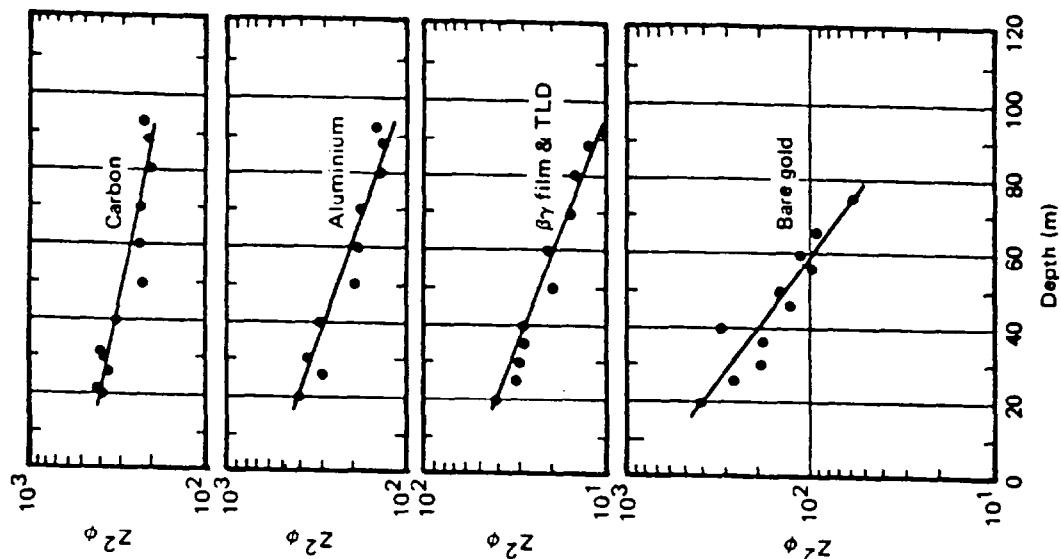


Fig. 4.5 Approximate exponential absorption of neutron flux density and gamma dose rate in a large straight tunnel for a variety of detectors. [Reproduced from (Gi69).]

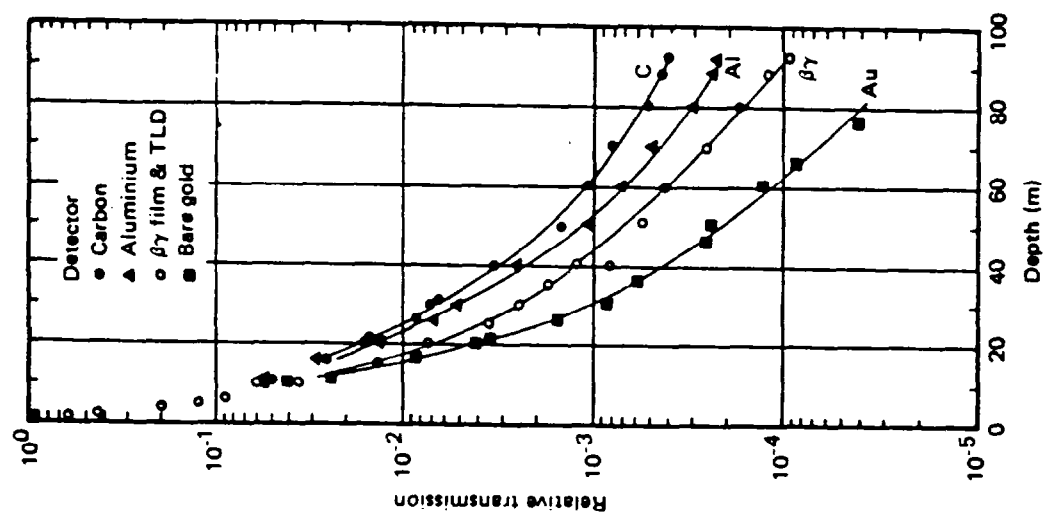


Fig. 4.4 The relative transmission of neutron flux density and gamma dose rate along a large straight tunnel. [Reproduced from (Gi69).]

It is clear that the low energy part of the spectrum attenuates more rapidly by air and wall scattering than do the higher energy neutrons. Also, for short tunnels (< 20 m long) the "attenuation" of the fast neutrons is almost entirely accomplished by inverse-square law considerations. (In these figures, the coordinate "d" or "Z" was used to represent distance along the tunnel.) It is also clear that the transmission, when inverse-square effects are excluded, is approximately an exponential with effective mean free paths, $\lambda(E)$, corresponding to effective, energy-dependent, removal cross sections. These also were determined in (Th88) and *op. cit.* and are given in Table 4.2.

Table 4.2 Mean free paths and removal cross sections for tunnel transmission as exhibited by the measurements summarized in Figs. 4.4 and 4.5. [Reproduced from (Th88).]

Detector	Mean free path (m)	Removal cross-section (b)
Plastic scintillator	100	1.9
Aluminium	60	3.2
Film and TLD	55	3.3
Bare gold	30	6.2

It is of some interest that the effective removal cross sections determined by this measurement are about a factor of 1.5 to 2 "too small" compared to those that would be inferred from the known cross sections for the constituents of air. "In-scattering" of the concrete walls may well provide some explanation since more neutrons were observed at the larger distances into the tunnel.

Of course, details of the source geometry are very important in such a straight penetration. K. Goebel [(Go75) and summarized in (Sc90)] has calculated "universal" curves for "first" legs of labyrinths (i.e., equivalent to such a "straight" penetration). Goebel used and compared results from the codes SAM-CE (Co73), AMC (Ma67), and ZEUS (D'H68). Gollon and Awschalom (Go71) have generated similar curves using the ZEUS code for a variety of geometries. The three conditions of point source, line source, and plane or point source off axis for a straight tunnel displayed as universal dose attenuation curves as a function of the distance into the tunnel in units of the square root of the cross-sectional area as calculated by Goebel are given in Fig. 4.6 taken from (Go75) [also in (Sc90)]. In these results it is obvious that extended, or "off axis", sources are more readily attenuated because the tunnel aperture provides less "acceptance". As a matter of terminology, the "mouth" of a given leg is the innermost opening of the leg under consideration.

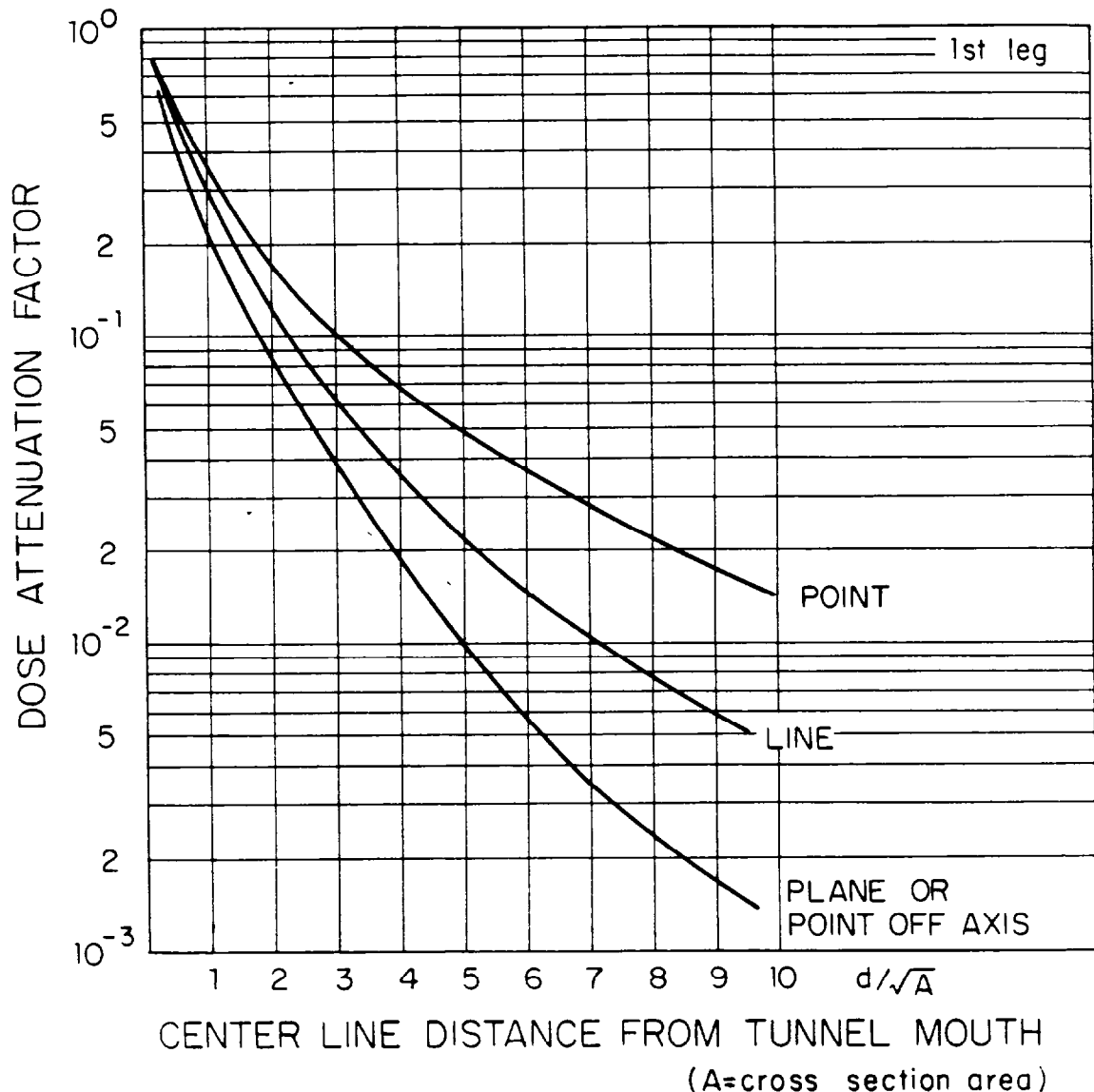


Fig. 4.6 Universal transmission curves for the first leg of a labyrinth. [Reproduced from (Go75).]

Figure 4.7, taken from (St73), shows a two-legged penetration at the NIMROD synchrotron. This penetration was of cross section $2.3 \times 2.3 \text{ m}^2$ and the walls were made of concrete. The target at the mouth of the labyrinth was bombarded by 7 GeV protons.

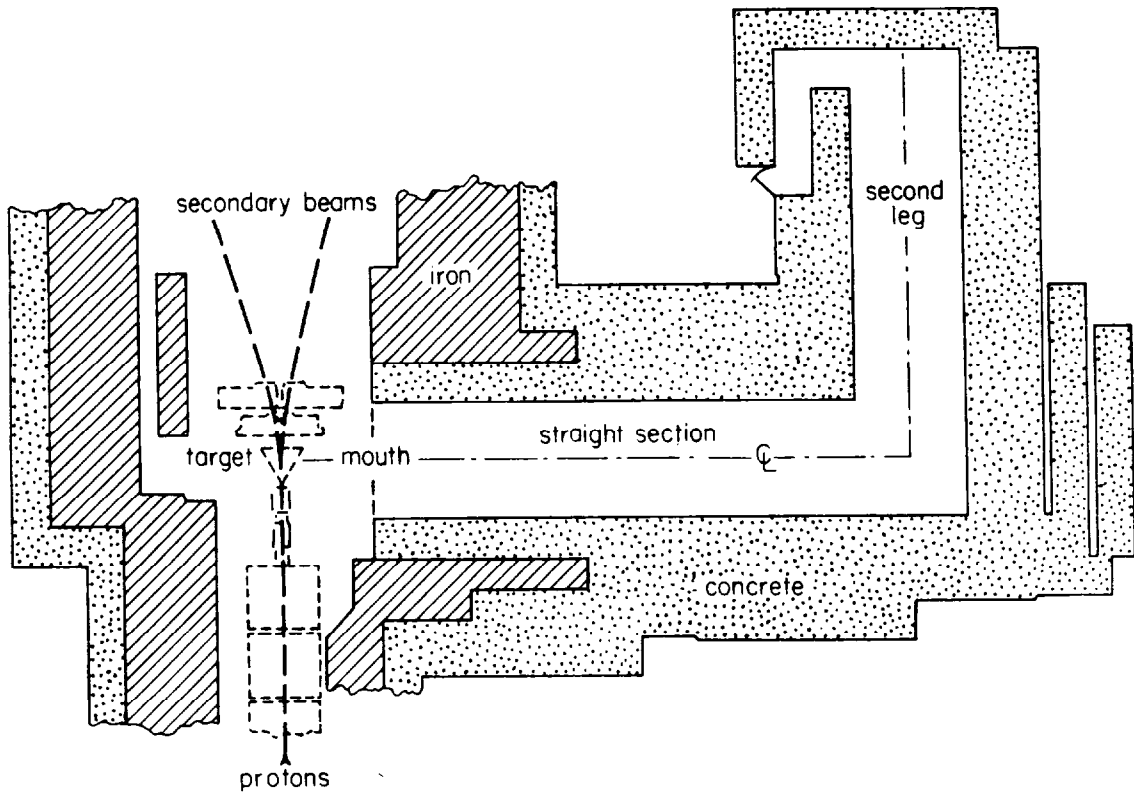


Fig. 4.7 Experimental layout used to study the transmission of neutrons around right angle bends. [Reproduced from (St73).]

Figure 4.8, taken from (St73), is a plot of the transmission of particle flux density along this tunnel for four different nuclear reactions, again used because of their thresholds. One can see that (proceeding from the target outward in the passageway) beyond the abrupt jump which arises because the corner hides the target from view, the fast neutron components are attenuated greatly below the thermal one. Stevenson and Squier (St73) reported changes in the spectrum at a right-handed bend in a labyrinth and a change in attenuation in the second leg of such a labyrinth. [This phenomena was also verified in the results of (Co85a).] The results are illustrated in Fig. 4.8 in the plot of neutron transmission.

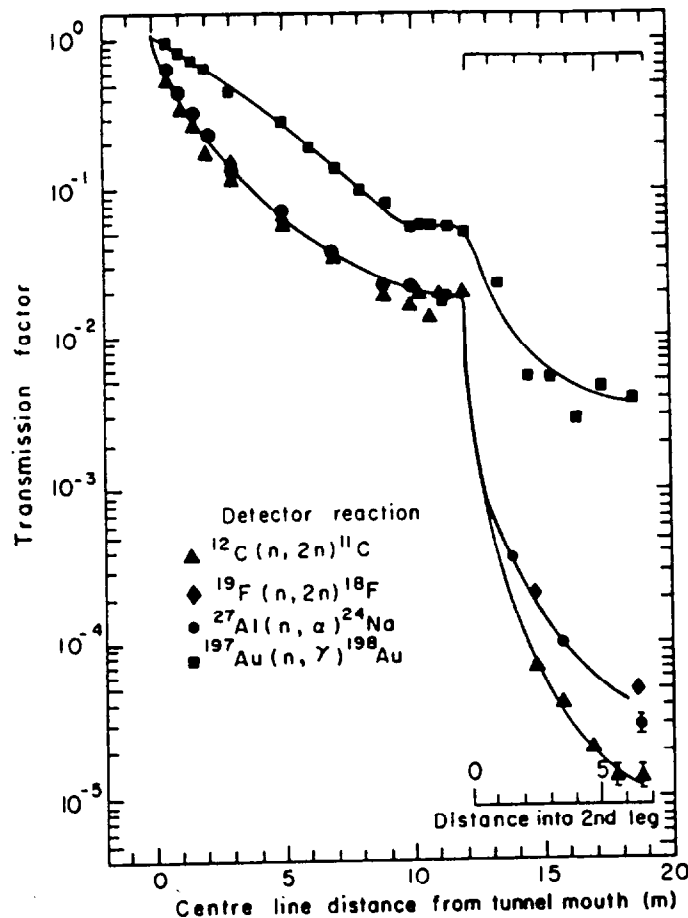


Fig. 4.8 Relative transmission of particle flux density along the tunnel layout shown in Fig. 4.7. [Reproduced from (St73).]

Second and successive legs of such "rectilinear" penetrations thus change the situation dramatically, principally by modifying the spectrum of the transmitted neutrons. Fig. 4.9 taken from (Go75) [also in (Sc90)] is a universal curve for second and succeeding legs which is a companion to that given for the first leg in Fig. 4.6. [In Fig. 4.9, the "distance from tunnel mouth" is the distance from the mouth of a given leg, not from the initial entrance into the passageway from the beam enclosure.] The results using the three codes mentioned previously disagree somewhat. The upper (dot-dashed) curve was obtained using SAM-CE, the middle (solid) curve resulted from the use of AMC, while the bottom (dashed) curve was obtained using ZEUS.

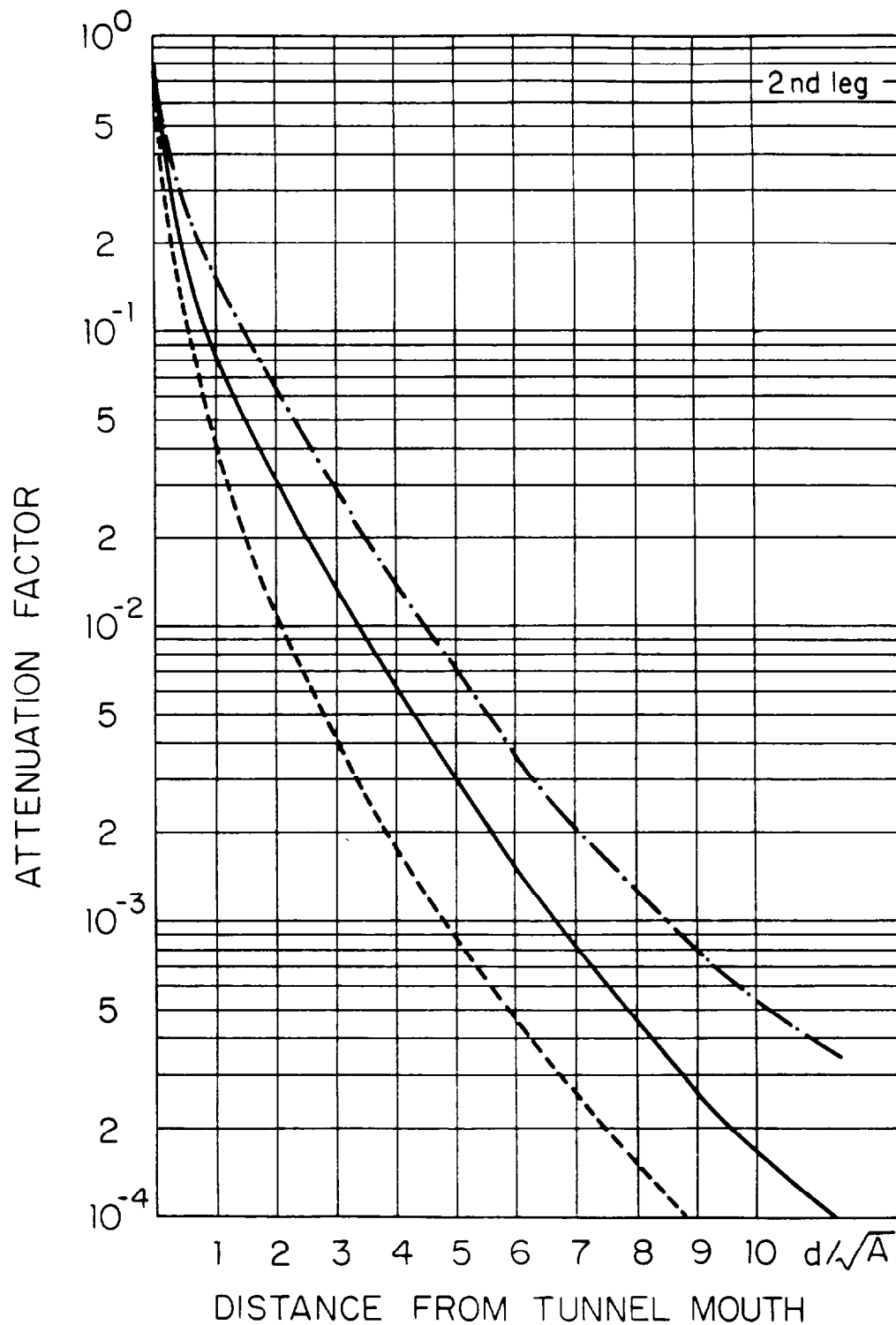


Fig. 4.9 Universal transmission curves for the second and subsequent legs of labyrinths. [Reproduced from (Go75).]

Tesch (Te82) has developed an entirely analytic approach to the problem of dose equivalent rate attenuation by multi-legged labyrinths at proton accelerators. For the first leg (the one directly viewing the point of beam loss) the expression is essentially an inverse-square law dependence with a simple "in-scattering" factor of two included. The expression for succeeding legs is in the form of the sum of two exponentials:

$$H_1(r_1) = 2H_0(r_0)r_0^2r_1^{-2} \quad 1^{\text{st}} \text{ leg} \quad (4.3)$$

$$H_i(r_i) = \left\{ \frac{[\exp(-r_i/0.45) + 0.022A_i^{1.3}\exp(-r_i/2.35)]}{[1 + 0.022A_i^{1.3}]} \right\} H_{i-1} \quad i^{\text{th}} \text{ leg } (i > 1) \quad (4.4)$$

In these formulae, the mouth of the labyrinth is r_0 meters from the source, the coordinate r_1 (meters) is the distance from the source into the first leg and $H_0(r_0)$ is the dose equivalent at the mouth (from a point source). In the formula for the i^{th} leg, H_{i-1} is the dose equivalent at the entrance to it, r_i is the distance into it (in meters), and A_i is the cross sectional area of the enclosure (meters²). Thus the second formula is used "recursively" to determine the dose equivalent at the exit. This formula is easily used on a small calculator, but does not contain the expected scaling with the square root of the tunnel aperture. It is best used for personnel (i.e., "door-sized") labyrinths having cross sectional areas of approximately 2 m².

Figure 4.10 taken from (Co85a) shows a four-legged labyrinth providing entrance to a tunnel above a target stuck by 400 GeV protons from the Tevatron at Fermilab.

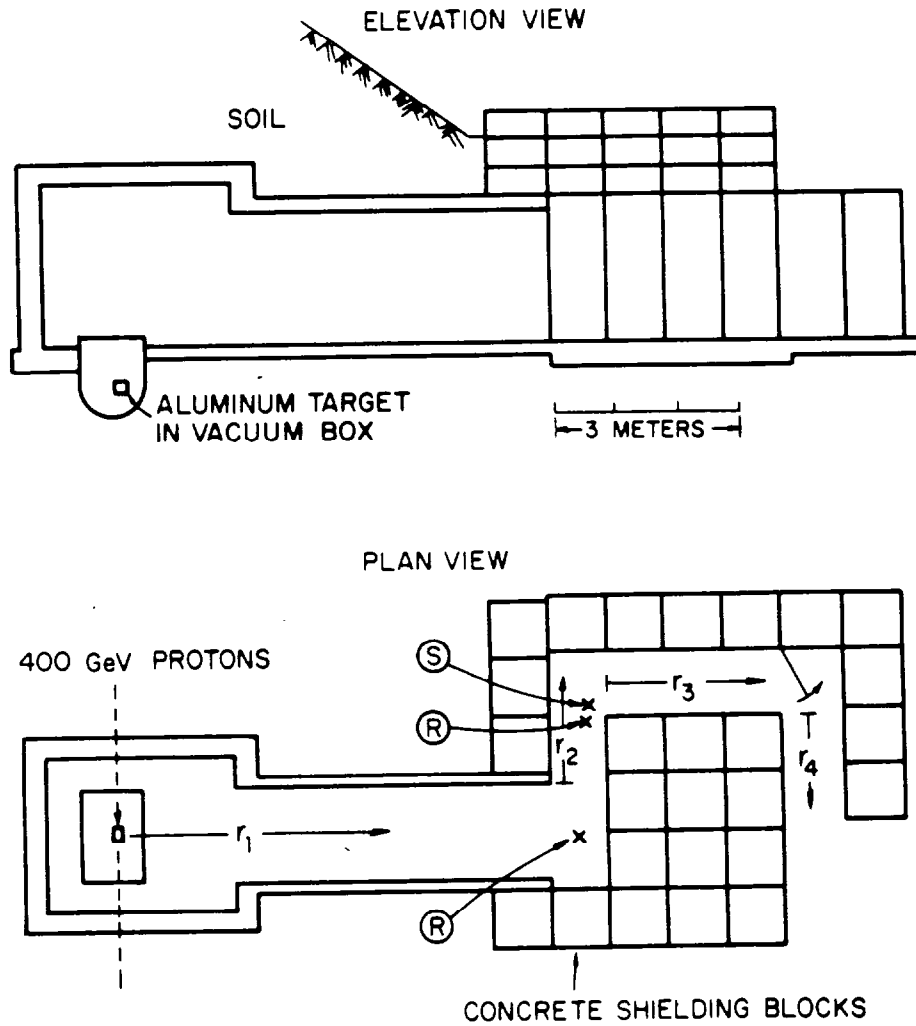


Fig. 4.10 Plan and elevation views of the access labyrinth studied in (Co85a). Coordinates are defined in the figure. Locations of Bonner Sphere (S) neutron spectra and recombination chamber (R) measurements of quality factor are indicated. [Reproduced from (Co85a).]

Figure 4.11 taken from (Sc90) compares experimental results obtained in the Fermilab labyrinth (Co85a) with several methods of calculation. As one can see, all three methods of calculating the attenuation are approximately valid even for this four-legged labyrinth. [As a coincidence, the "transmission factor scale" on the ordinate is also the absolute scale of the Fermilab absorbed dose measurements as indicated.] The assumption that succeeding legs can be considered the same as the second leg is approximately verified.

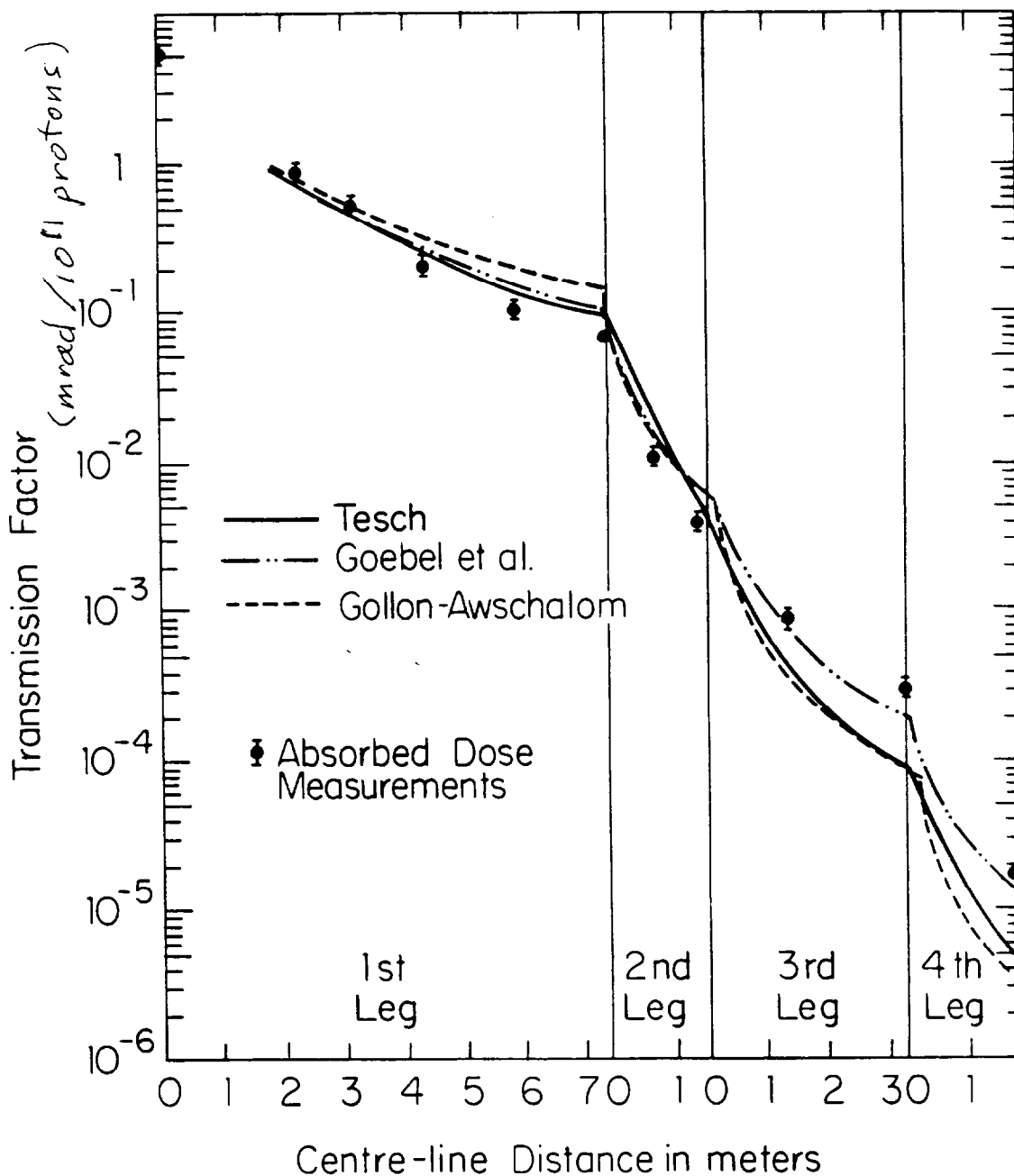


Fig. 4.11 Measurements and predictions of transmission in a tunnel at Fermilab. [Reproduced from (Sc90).]

Chapter 4 Low Energy Prompt Radiation Phenomena

For this labyrinth, a recombination chamber technique (see Chapter 6) was used to measure the neutron quality factor (Q) at two locations, one at the end of the first leg and one in the middle of the short second leg (locations denoted "R" in Fig. 4.10)). The results were $Q = 5.5 \pm 0.6$ and $Q = 3.4 \pm 0.1$, respectively. This indicates a softening of the neutron energy spectrum in the second leg which was further verified by a measurement of the neutron energy spectrum using a multisphere technique (see Chapter 6) which resulted in $Q = 3.1 \pm 0.7$. The measured second-leg spectrum exhibited domination by thermal, or near-thermal neutrons. It is clear that several approaches to the design of labyrinths are equally effective for practical radiation protection work.

Curved tunnels are principally used to provide access for large equipment items that cannot negotiate right-angle bends. These have not been treated in nearly the same detail as have the rectilinear passageways. It appears that the attenuation is effectively an exponential with an attenuation length, λ , a function of only the radius R of the tunnel. Patterson and Thomas (Pa73) determined

$$\lambda = 0.7 (R)^{1/2}, \quad (4.5)$$

where R is in meters and $4 < R < 40$ meters. This appears to fit the extremely sparse available data.

A final piece of information that is needed in practical labyrinth calculations is the answer to the following question: "What happens to the neutrons beyond the "exit" to the passageway?"

Direct observational evidence is that beyond the exit, the neutrons "disappear" rather rapidly. This phenomenon is probably due to the fact that the neutron energy spectrum is heavily dominated by thermal and near-thermal neutrons in all "legs" after the first [(St73) and (Co85a)]. Such neutrons, therefore, having suffered many scatters would not be "collimated in any particular direction". Elwyn (El91) has quantified this phenomena as follows:

Assume that the exit of the labyrinth is a circular disk of area A (equivalent in area to that of the exit opening) and that the neutrons emerge from this disk at all random directions with source strength (neutrons/unit area) S_A . Fig. 4.12 illustrates the geometry.

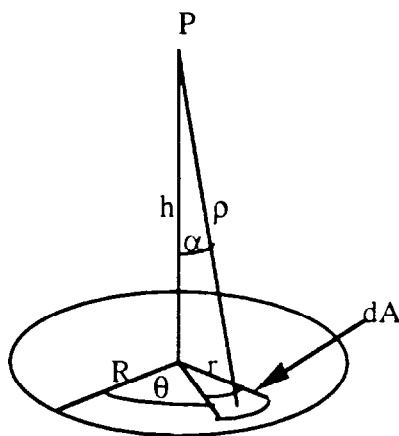


Fig. 4.12 Diagram of labyrinth exit neutron calculation.

Further, assume that there is only emission into the 2π steradian hemisphere outside the exit. Then the differential flux density at P on the axis of the disk is:

$$d\phi = \frac{S_A \cos \alpha \, dA}{2\pi \rho^2} \quad (4.6)$$

where $dA = r \, dr \, d\theta$, $\rho^2 = h^2 + r^2$, and angle α is defined in Fig. 4.12 ($\cos \alpha = h/\rho$). The $\cos \alpha$ factor is present to take into account the area of the source elemental area projected in the direction of point P. Thus,

$$d\phi = \frac{S_A h \, r \, dr \, d\theta}{2\pi \rho^3} \quad (4.7)$$

Integrating,

$$\begin{aligned} \phi(h) &= \frac{S_A h}{2\pi} \int_0^R dr \int_0^{2\pi} d\theta \frac{r}{(r^2 + h^2)^{3/2}} = \frac{S_A h (2\pi)}{2\pi} \int_0^R dr \frac{r}{(r^2 + h^2)^{3/2}} \\ &= h S_A \left[\frac{-1}{\sqrt{h^2 + r^2}} \right]_0^R = S_A \left[1 - \frac{1}{\sqrt{1 + \left(\frac{R}{h}\right)^2}} \right] \end{aligned} \quad (4.8)$$

where attenuation by the air is neglected. Thus one can use this by approximating the area of the exit opening by the area of a disk have an equivalent area. The rapidity of the decrease of fluence is illustrated by the tabulation of a few values in Table 4.3.

Table 4.3 Estimates of relative neutron flux or dose equivalent as a function of scaled distance from the exit of a labyrinth.

h/R	$\phi(h)/S_A$
0.5	0.55
1.0	0.29
2.0	0.11
4.0	0.03
10.0	0.005

At large distances, one can apply a "point source" approximation due to the fact that:

$$\phi(h) = S_A \left[1 - \left(1 + \frac{R^2}{h^2} \right)^{-1/2} \right] \approx \frac{S_A}{2} \left[\left(\frac{R}{h} \right)^2 \right] = \frac{S_A R^2}{2 h^2} \quad \text{for } h \gg R. \quad (4.9)$$

For $h = 0$, $\phi(0) = S_A$ as expected.

To summarize the results of this section so far; one can use a calculation or measurement of the neutron flux density or dose equivalent at the entrance (beam enclosure side) of the labyrinth in conjunction with one of the above methods of calculating the attenuation of the neutrons by the passageway to get an estimate of the dose equivalent or fluence at the exit of the passageway.

Chapter 4 Low Energy Prompt Radiation Phenomena

Generally, the dose at the entrance can be obtained using Monte-Carlo techniques. Approximations that use Moyer Model parameters discussed in Chapter 3 are likely to overestimate the dose equivalent at the entrance. This is due to the fact that the Moyer parameter implicitly assumes development of the shower (a "buildup" mechanism, as seen in Chapter 3) in the enclosure shielding which is, in effect, short-circuited by the passageway.

For high energy proton accelerators, a rule of thumb for the source term which has been found to be very successful for the degree of accuracy generally required for personnel protection purposes has been developed at Fermilab by Ruffin and Moore (Ru76), and recently improved by inclusion of the Moyer energy scaling by Rameika (Ra91). In this model, it is observed that about one fast neutron/GeV of proton beam energy is produced with an isotropic distribution in addition to the much higher multiplicity in the forward direction. The neutrons which will dominate the spectrum and determine the dose equivalent at the entrance to the labyrinth are those around 1 to 10 MeV of kinetic energy. From the fluence to dose equivalent information, 8.3 neutrons/(cm² s) corresponds to 1 mrem/hour. Hence, 3×10^7 neutrons/cm² approximately corresponds to 1 rem.

Thus, at distance R (cm) from the source, Rameika obtains

$$H(\text{rem}) = \frac{E_0^{0.8} N_p}{4\pi R^2 (3 \times 10^7)} = \left(2.65 \times 10^{-9} \right) \frac{E_0^{0.8} N_p}{R^2} . \quad (4.10)$$

where R is in cm, E_0 is in GeV, and N_p is the number of incident protons (This could be generalized to applying to the number of incident hadrons). The constant, 2.65×10^{-9} (rem cm²), turns out to be approximately 1/3 the value obtained by using the Moyer source (see Chapter 3) parameter along with the Moyer angular factor at $\theta = \pi/2$;

$$(2.8 \times 10^{-7} \text{ rem cm}^2) \exp(-2.3\pi/2) = 7.6 \times 10^{-9} \text{ rem cm}^2. \quad (4.11)$$

III. Skyshine

Thin roof shielding represents a "curse" that has plagued a number of accelerators such as the Cosmotron (BNL), the Bevatron (LBL), and the Fermilab experimental areas. This "curse" actually represents situations in which the roof of some portion of the accelerator or an associated experimental facility is shielded more thinly than are the sides of the same enclosure which "directly viewed" the radiation source. The first attempt to calculate the so-called "skyshine" contribution was made by Lindenbaum (Li61). Reference (Sc90) gives a rather complete description of the phenomena. References (Pa73), (Ri75), (St84), and (Co85b) give some specific results.

Figure 4.13 taken from (Sc90) shows a summary of existing measurements of the neutron fluence times the square of the distance from the source, $r^2\phi(r)$. As one can see in this figure, in general, the value of $r^2\phi(r)$ is characterized by a buildup followed by an exponential falloff. As exhibited by the typical skyshine data, λ , the effective attenuation length, has been found to vary between a minimum value of about 200 meters and much larger values which approach one kilometer.

(Pa73) gives a satisfactory formula that can empirically describe such behavior for $r > 50$ meters.

$$\phi(r) = \frac{aQ}{4\pi r^2}(1 - e^{-r/\mu})e^{-r/\lambda}. \quad (4.12)$$

In this equation, the isotropicity of the distribution is obvious, $a = 2.8$ and represents an empirical "buildup" factor, while μ is the effective "buildup" relaxation length and λ is an effective interaction length. From the existing data, typically $\mu = 56$ meters. Q is the source strength which dimensionally must be consistent with $\phi(r)$. Thus, for the standard meaning of $\phi(r)$ as the flux density, Q is in units of neutrons emitted by the source per second.

Values of $\lambda > 830$ meters are possible if very high energy neutrons ($E > 150$ MeV) are present. [Such "apparent" large values can also result from the presence of extended or multiple sources.] Concerning "high energy sources", for example, it was known that high energy neutrons were present in one of the situations examined in (St73), where the shielding was extremely thin. For that situation a value of $\lambda \approx 1200$ meters was obtained. After the addition of more shielding (presumably bringing the energy spectrum into "equilibrium" such that a large number of lower energy neutrons were present), a value of $\lambda = 340$ meters was obtained. A value of 830 m (100 g/cm² of air at STP) corresponds to the interaction of the ≈ 100 MeV neutrons likely to control the propagation of hadronic cascades in air (see Chapter 3). Thus, λ is determined by the neutron energy spectrum present at the thinly shielded location.

The procedure, then, for using the above equation is to:

- A. Estimate the total emission rate of neutrons from the source. This can be done by using a neutron spectrum information to choose an "average" energy. The flux density to dose equivalent rate factor at that energy can then be used in conjunction with a dose equivalent rate survey over the thinly shielded region to determine the total neutron emission rate (Q) by numerically integrating over the area of the top of the shield.

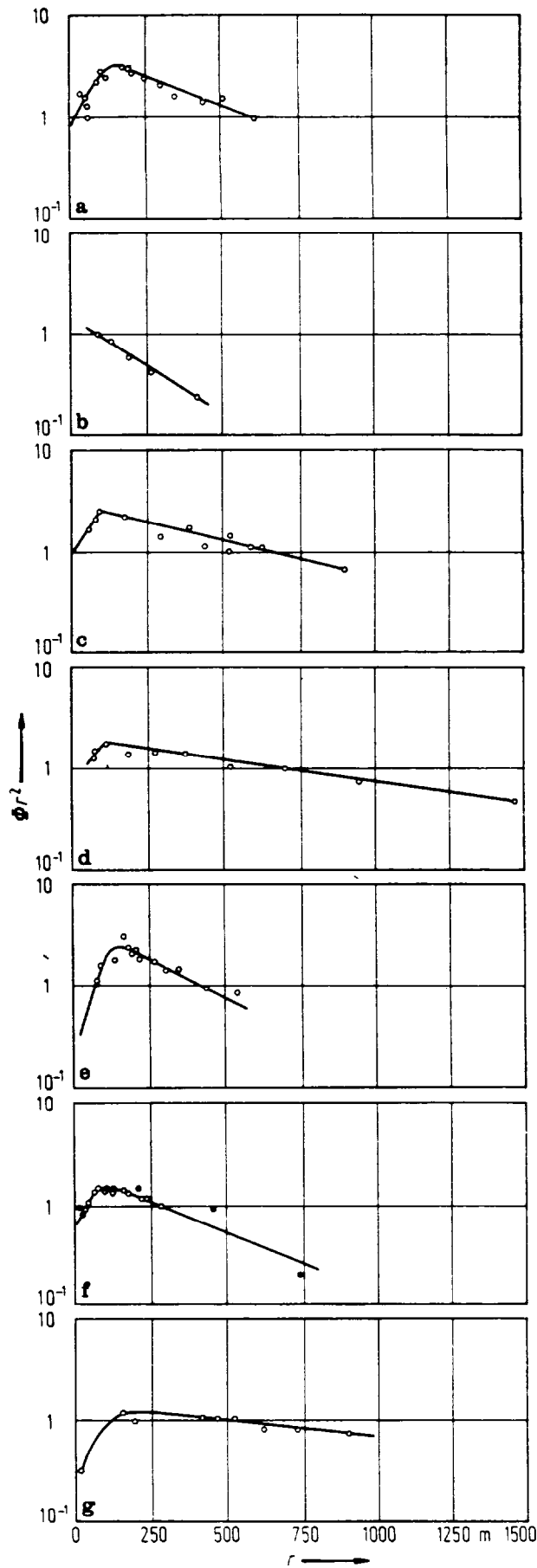


Fig. 4.13 Neutron flux measurements performed around different accelerators. The abscissa is the distance r from the accelerators, the ordinate is the product of the measured neutron flux density ϕ and the square of the distance. In these coordinates, a $1/r^2$ variation is represented by a horizontal line. a) Measurements of the fast neutron flux density performed at the CERN 28 GeV Proton Synchrotron. b) Measurements of the fast neutron flux density performed at the Dubna 10 GeV Proton Synchrotron. c) Measurements of the dose equivalent rate performed at the Brookhaven 30 GeV Proton Synchrotron. d) Measurements of the fast neutron flux density performed at the CERN 600 MeV Proton Synchrotron. e) Measurements of the fast neutron flux density performed at the DESY 7.5 GeV Electron Synchrotron. f) Measurements of the fast neutron flux density performed at the Rutherford Laboratory Proton Linear Accelerator (solid dots for 30 MeV protons, open dots for 50 MeV protons). g) Measurements made at the 12 GeV Proton Synchrotron at KEK. [Reproduced from (Sc90) as adapted from references cited therein.]

- B. Estimate the value of λ from the spectral information.
- C. Apply the above equation to determine the radial dependence.

A somewhat more rigorous treatment has been reported by Stevenson and Thomas [(St84) summarized also in (Sc90)]. Stevenson and Thomas used as a starting point the separate work of Nakamura and Kosako (Na81) and of Alsmiller, Barish, and Childs (Al81). Stevenson and Thomas parameterized the phenomena by the following equation:

$$\phi(r) = \frac{Q'}{4\pi r^2} e^{-r/\lambda}. \quad (4.13)$$

In this equation, the buildup exponential has been suppressed so the formula is valid only at large distances (i.e., $r \gg 56$ meters). In addition, the quantity denoted by Q' ignores the buildup factor of 2.8.

The Nakamura and Alsmiller groups have separately performed extensive Monte-Carlo calculations of the neutrons emitted into cones of small vertex angle. Nakamura and Kosako used the Monte-Carlo code MORSE while Alsmiller, Barish, and Childs used the Discrete Ordinates Transport Code DOT. [Despite the title of Ref. (Al81), the calculations were performed in the context of the design of the 400 GeV accelerator ISABELLE at Brookhaven National Laboratory.] For certain selected distances from the skyshine source, these workers have calculated the dose equivalent as a function of both the source neutron energy and the emission cone's semivertical angle (that is, the half-angle the rotation of which defines the cone). The authors define this quantity, the "neutron importance", as the dose equivalent per neutron. The results are given in Fig. 4.14 taken from (Al81) [also in (Sc90)]. The Alsmiller calculations are for a semivertical angle of 37° .

Stevenson and Thomas (St84) were able to derive an alternative "recipe" for skyshine neutron calculations by making two assumptions:

- A. The neutron spectrum has the $1/E$ form up to the proton energy and zero at higher energies. This likely overestimates the contribution of the higher energy neutrons.
- B. The neutrons are emitted into a cone whose semivertical angle is about 70 - 80° . This may overestimate the doses by up to a factor of three for sources of very small semivertical angles.

Further, they used the results of Fig. 4.14 to estimate the value of λ based upon the upper energy of the $1/E$ spectrum. Fig. 4.15 taken from (St84) [also in (Sc90)] uses the values for several choices of upper energies at the three distances given in Alsmiller's calculation in a plot in which the $1/r^2$ dependence is suppressed. (The curve labeled "BNL" is the result of a measurement at 28 GeV at Brookhaven National Laboratory.) The slopes were, then, used to obtain values of λ as a function of "upper energy" which are plotted in Fig. 4.16.

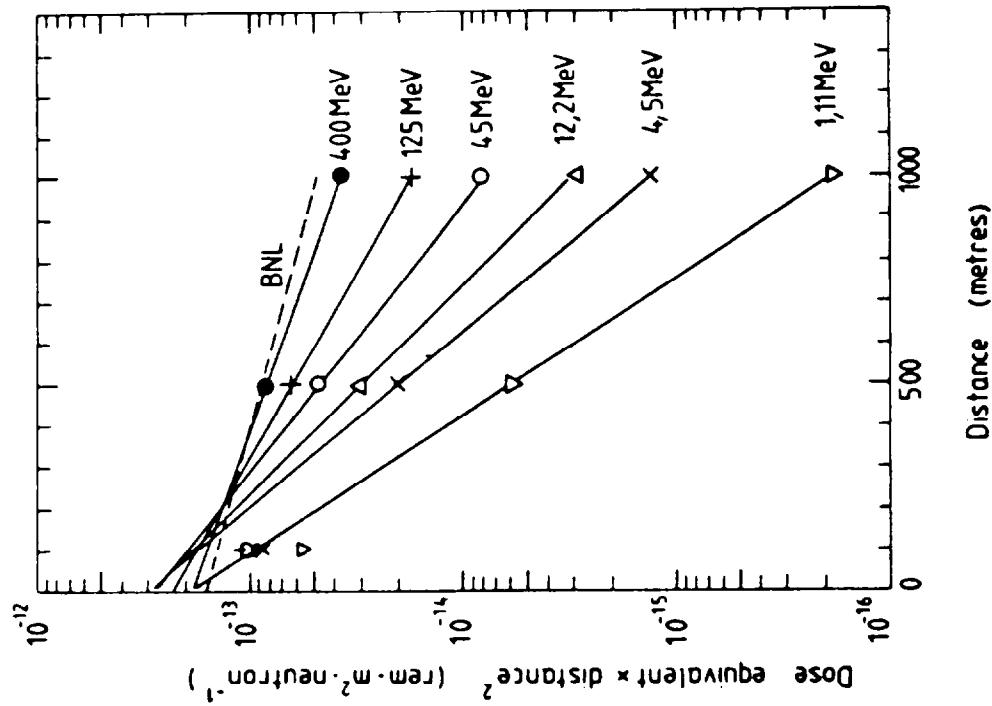


Fig. 4.15 Variation of dose equivalent with distance r for $1/E$ neutron spectra with different upper energies. Ordinate is dose equivalent H times distance squared. The curve labeled "BNL" is a measurement. [Reproduced from (Sc90).]

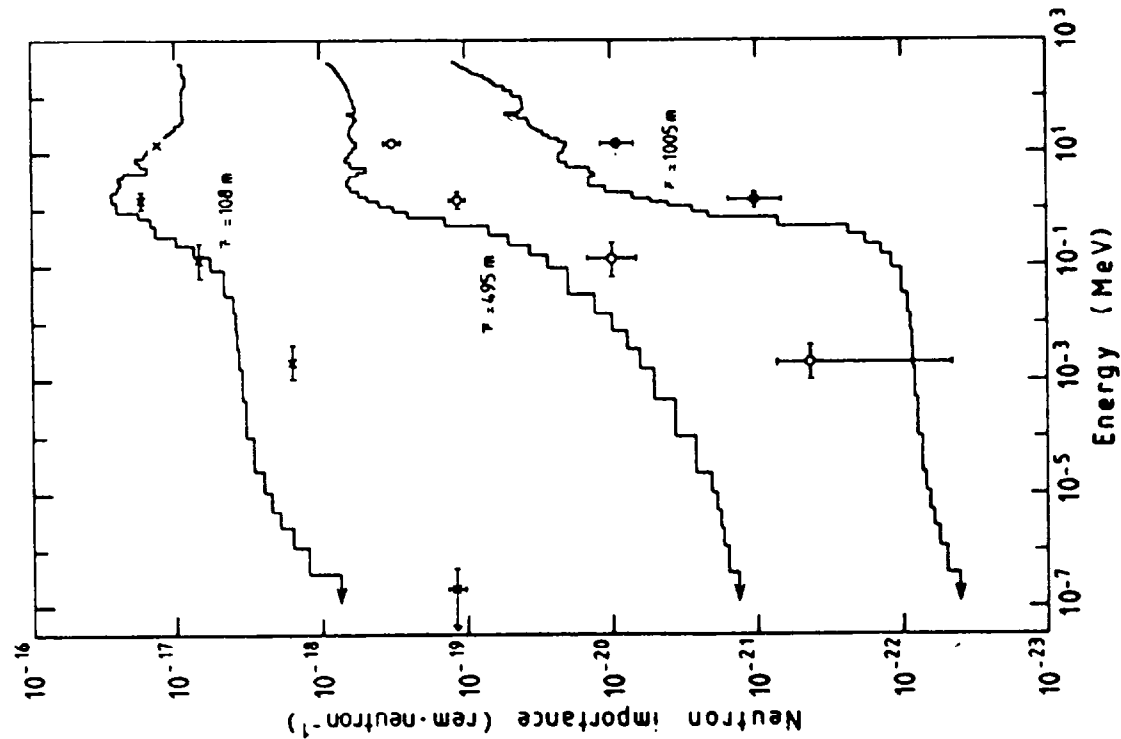


Fig. 4.14 Neutron skyline importance functions for small semivertical cone angles. The histogram gives the results of the calculations of (Al81), the crosses, open circles, and closed circles are from (Na81). [Reproduced from (Sc90).]

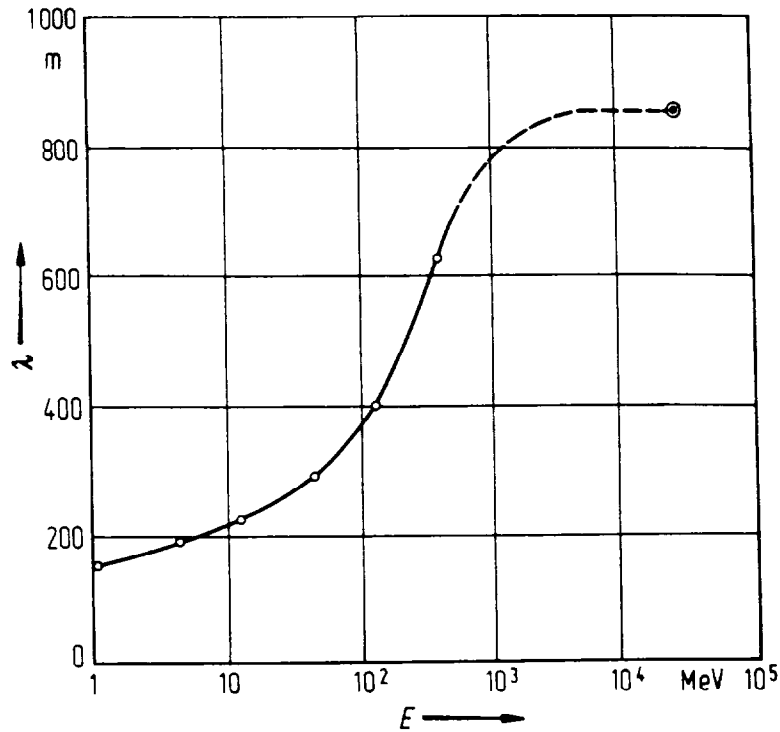


Fig. 4.16 Effective absorption length λ as a function of upper neutron energy E for $1/E$ spectra.

Slopes determined in this way were successfully applied to data taken at 30 and 50 MeV at the Rutherford Laboratory Proton Linear Accelerator (thus demonstrating the lack of sensitivity to proton energy) as shown in Fig. 4.17 taken from (St84) [also in (Sc90).]

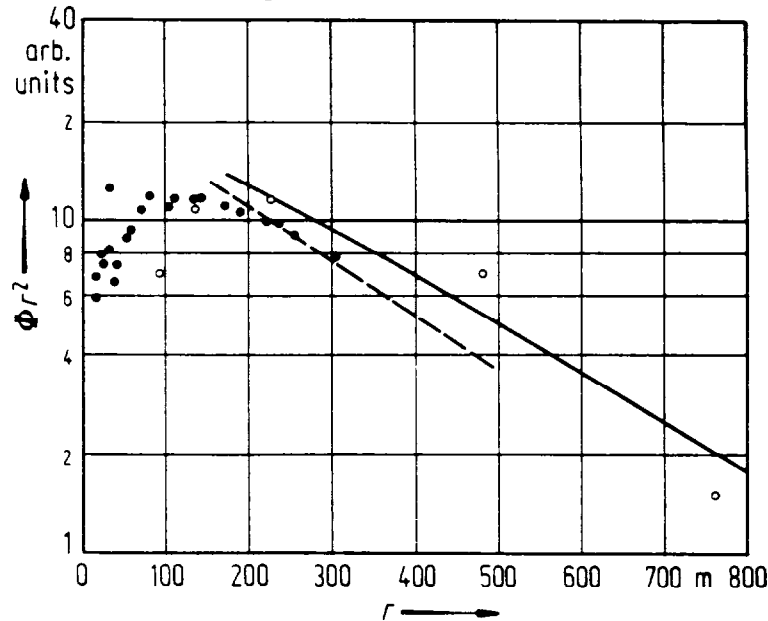


Fig. 4.17 Comparison of the effective absorption lengths for 30 and 50 MeV data obtained at the Rutherford Laboratory Proton Linear Accelerator. The abscissa is the distance r from the source while the ordinate is the flux density times the distance squared in arbitrary units. [Reproduced from (Sc90) as adapted from references cited therein.]

Chapter 4 Low Energy Prompt Radiation Phenomena

To determine the all important source term, the straight lines in Fig. 4.15 (on the semi-logarithmic plot) were extrapolated to zero and used to determine intercepts at $r = 0$ ranging from 1.5×10^{-15} to 3×10^{-15} Sv m²/neutron (1.5×10^{-13} to 3×10^{-13} rem m²/neutron. Note that the BNL data also are in agreement with such a result. Hence, conservatively, Stevenson and Thomas found that

$$H(r) = \frac{3 \times 10^{-13}}{r^2} e^{-r/\lambda} \text{ (rem/neutron, } r \text{ in meters) .} \quad (4.14)$$

Again, one has to determine the total number of neutrons emitted. This can be done as before by measuring the integral of dose equivalent times area over the thinly shielded location and using the reciprocal of the fluence-to-dose equivalent conversion factor to get the total number of neutrons emitted. The use of the above formula will lead to an overestimate of neutrons for values of r less than approximately 100 meters because the extrapolation ignores the observed exponential buildup of the skyshine.

(St84) gives a convenient table of dose-equivalent-to fluence conversion factors derived from data in ICRP Publication 21 (IC73) which is reproduced here as Table 4.4

Table 4.4 Dose equivalent per neutron/cm² for 1/E Neutron Spectra of Different Upper Energies [Reproduced from (Ref. 30).]

Upper Energy (MeV)	Spectrum Averaged Dose Equivalent Conversion (10 ⁻⁹ rem/(n cm ⁻²))
1.6	3.9
2.5	4.8
4.0	5.6
6.3	6.4
10	7.2
16	7.9
25	8.6
40	9.4
63	10.1
100	10.9
160	11.7
250	12.5
400	13.4
630	14.6
1000	16.2
1600	18.4
2500	21.2
4000	25.0
6300	30.0
10000	36.5

Measurements at Fermilab (Co85b) have confirmed this general method for a "source" involving the targetry of 400 GeV protons. Figure 4.18 taken from (Co85b) shows two measured and fitted radial distributions. These fits were made using the formula explicitly showing the buildup factor and employing the source term Q rather than Q' .

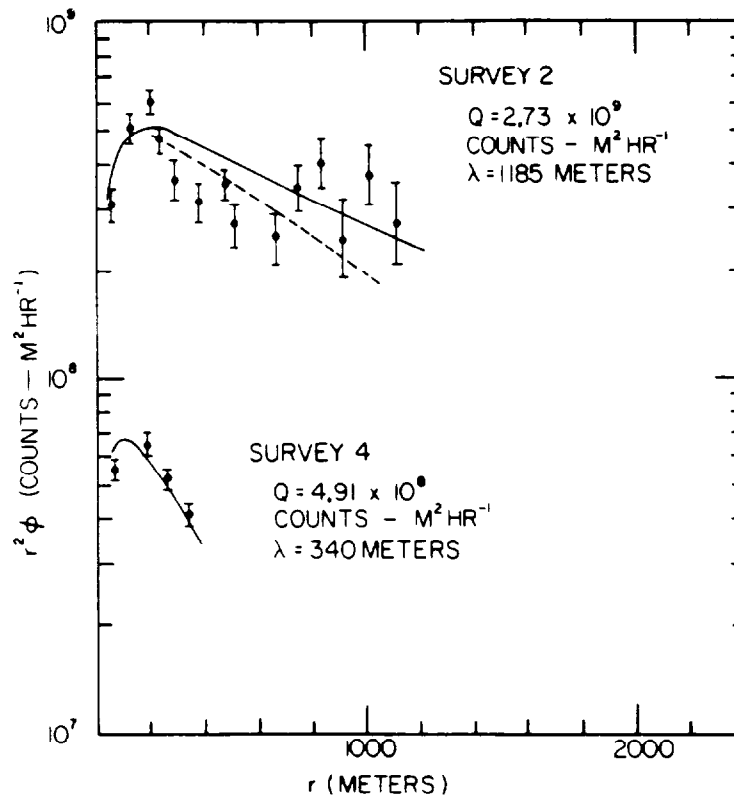


Fig. 4.18 Skyshine data from two different surveys plotted as $r^2\phi$ as a function of distance from the source r . The solid curves are from the least squares fit of Eq. (4.12) to the data points while the dashed curve is the fit if λ is constrained to have a value of 830 m. Error bars represent 1 standard deviation counting statistics. [Reproduced from (Co85b).]

In Fig. 4.18, "Survey 2" corresponds to a shielding configuration where the neutron energy spectrum was inferred to be of very high energy while "Survey 4" was likely to involve a softer spectrum. Survey 4 was made for the same beam and target after the concrete shield thickness was greatly increased compared with the shield present when "Survey 2" was obtained. (The normalization to "counts- m^2/hr " can, for purposes of this discussion, be ignored.) The instrument calibration of "counts/hr" made possible an estimate of dose rates at $r = 200$ meters for the two surveys. If one makes an educated guess that the conditions of "Survey 2" correspond to an upper energy of 1 GeV and that the conditions of "Survey 4" correspond to an upper energy of 100 MeV (again, by making an "educated guess"), one can then apply the conversion factors. Experimentally, the value of Q for the Survey 2 conditions was determined to be 2.5×10^5 mrem m^2/hr (obtained from the measured absorbed dose surface integral of 5×10^4 mrad m^2/hr and assuming a quality factor of 5). For the Survey 4 conditions Q was found to be 4.0×10^4 mrem m^2/hr (again, obtained from the measured absorbed dose surface integral of 8.1×10^3 mrad m^2/hr and assuming a quality factor of 5).

Chapter 4 Low Energy Prompt Radiation Phenomena

Table 4.5 makes a comparison with the prescription of (St84). In the table, H is the dose equivalent in one hour at 200 meters. The prescription of Stevenson and Thomas (St84) is used to calculate the dose equivalent in one hour at 200 meters.

Table 4.5 Comparisons of Fermilab skyshine data with results of parameterizations. The quantities are all for a one hour time period.

Survey	λ (meters)	E_{max} (MeV)	Fluence-Dose Conversion		Q-measured (mrem m ²)	H (200 m) (mrem)	H (200 m) (mrem)
	(Co85b)	(inferred)	(St84)	n m ⁻² /mrem	(Co85b)	calculated (St84)	experiment (Co85b)
Survey 2	1200	1000	16.2 X 10 ⁻⁶	6.17 X 10 ⁸	2.5 X 10 ⁵	1.0	1.6
Survey 4	340	100	10.9 X 10 ⁻⁶	9.17 X 10 ⁸	4.0 X 10 ⁴	0.15	0.15

The agreement is well within all uncertainties involved.

A final illustration comes from (El86) where the thin iron shield was involved. Fig. 4.19 taken from (El86) shows the radial dependence of neutron flux. In this measurement, λ was determined to be 184.4 m by fitting this radial dependence using the formula involving Q rather than Q'. This value is consistent with a neutron spectrum otherwise found to be dominated by neutrons of a few MeV (see above). In fact, the spectrum is dominated by neutrons of energies near 847 keV insofar as skyshine is concerned (i.e., a "thick" iron spectrum, see Chapter 3 and (El86). One can use the parametrization of (El86) to reproduce the measured fluence (normalized to 10¹² incident protons) at, say, r = 200 meters (where Q = 1.75 X 10¹⁰ was determined by fitting the skyshine data):

$$\phi(r) = \frac{aQ}{4\pi r^2} (1 - e^{-r/\mu}) e^{-r/\lambda}; \quad \phi(200) = \frac{2.8(1.75 \times 10^{10})}{4\pi(200)^2} (1 - \exp(-200/56)) \exp(-200/184.4)$$

$$= 3.20 \times 10^4 \text{ n m}^{-2}. \quad (4.15)$$

(Pa73), at 847 keV gives a flux density to dose equivalent rate conversion factor of 10.2 (n cm⁻²)/(mrem hr⁻¹) which is equivalent to 3.67 X 10⁸ neutron m⁻² mrem⁻¹. Thus, taking the measured neutron flux at r = 200 meters and applying this factor gives a dose equivalent per 10¹² incident protons of 8.7 X 10⁻⁵ mrem at r = 200 meters.

(El86) also estimated the total neutron emission of the source to be (3.4 ± 2.0) X 10¹⁰ per 10¹² incident protons. Applying the prescription of (St84):

$$H(r) = \frac{3 \times 10^{-13}}{r^2} e^{-r/\lambda} \text{ (rem/neutron, r in meters) ;}$$

$$H(200) = \frac{3 \times 10^{-13} (3.4 \pm 2.0) \times 10^{10}}{(200)^2} \exp(-200/184.4) \text{ (rem)}$$

$$= (8.6 \pm 5.1) \times 10^{-5} \text{ mrem at this same location.} \quad (4.16)$$

Thus the methodology is verified.

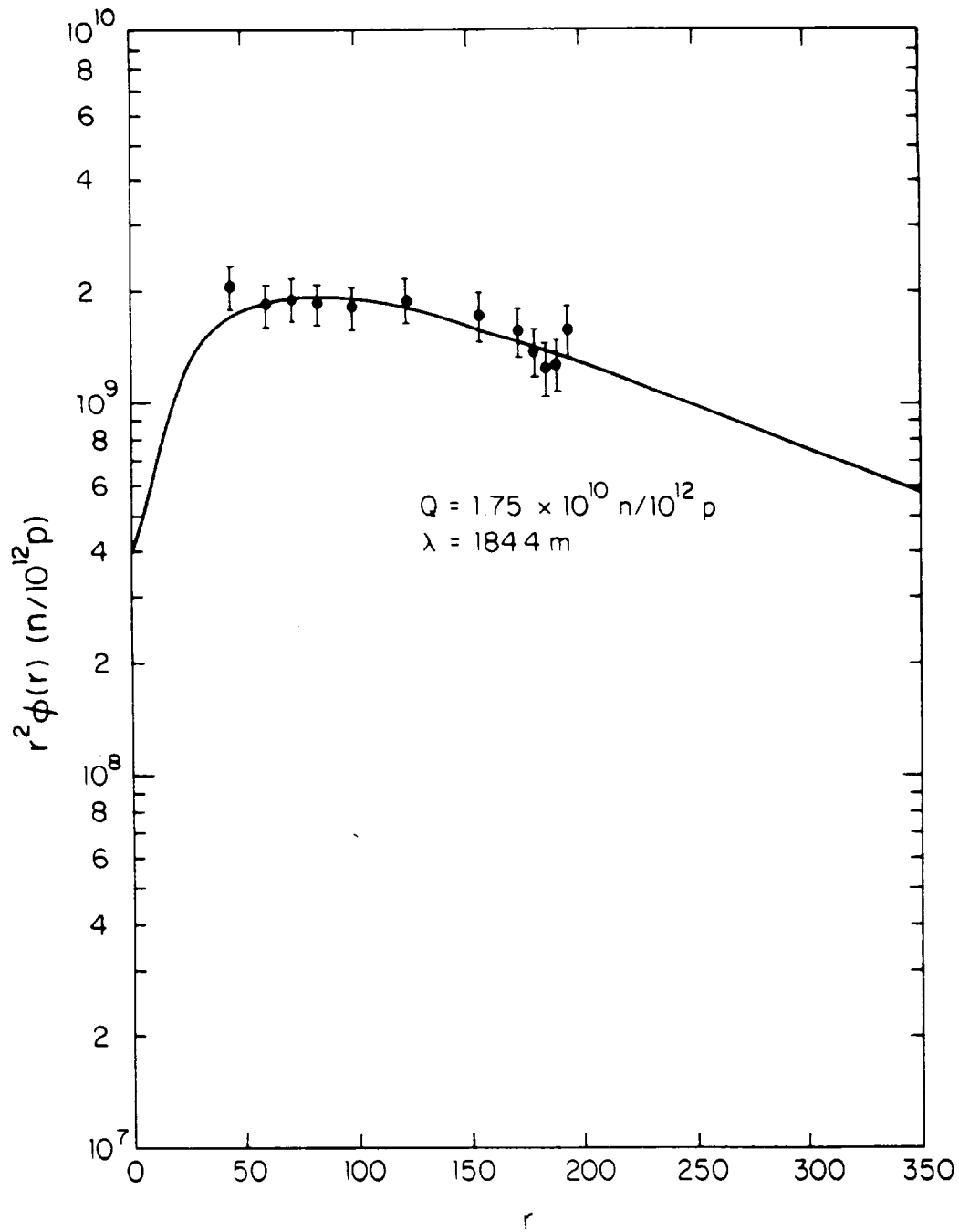


Fig. 4.19 The product of r^2 and the neutron fluence $\phi(r)$ per 10^{12} protons incident on a target as a function of the distance from the source r . The smooth curve is a fit to Eq. (4.12) with parameters $\lambda = 184.4 \text{ m}$ and $Q = 1.74 \times 10^{10}$ neutrons per 10^{12} protons. [Reproduced from (El86).]

References

- (Al81) R. G. Alsmiller, J. Barish, and R. L. Childs, "Skyshine at neutron energies < 400 MeV", Part. Accel. 11 (1981) 131.
- (Ch63) A. B. Chilton and C. M. Huddleston, "A semi-empirical formula for differential dose albedo for gamma rays on concrete", Nucl. Sci. Eng. 17 (1963)419.
- (Ch64) A. B. Chilton, "Backscatter for gamma rays from a point source near a concrete plane surface", Univ. Illinois Eng. Sta. Bull. No 471 (University of Illinois, Urbana, Illinois, 1964).
- (Ch65a) A. B. Chilton, "Backscattering of gamma rays from point sources by an infinite-plane concrete surface", Nucl. Sci. Eng. 21 (1965) 194-200.
- (Ch65b) A. B. Chilton, C. M. Davisson, and L. A. and Beach (1965). "Parameters for C-H albedo formula for gamma rays reflected from water, concrete, iron, and lead", Trans. Am. Nucl. Soc. 8, No. 2, (1965) 656.
- (Co73) M. O. Cohen, W. Guber, E. S. Troubezko, H. Lichtenstein, and H. A. Steinberg, "SAM-CE, a three dimensional Monte-Carlo code for the solution of the forward neutron and forward and adjoint gamma ray transport equations", Rep. DNA-2830-F, Rev. B Defense Nuclear Agency, Washington, DC (1973).
- (Co85a) J. D. Cossairt, J. G. Couch, A. J. Elwyn, and W. S. Freeman, "Radiation measurements in a labyrinth penetration at a high-energy proton accelerator", Health Phys. 49 (1985) 907-917.
- (Co85b) J. D. Cossairt and L. V. Coulson, "Neutron skyshine measurements at Fermilab", Health Physics 48 (1985) 171-181.
- (D'H68) M. M. D'Hombres, C. Devillers, F. Gervaise, B. De Sereville, and P. Tardy-Joubert, "Propagation des neutrons dans les tunnels d'Accès à un accélérateur de haute energie à protons", Rep. CEA-R-3491, Centre d'études nucléaires de Saclay (1968).
- (El86) A. J. Elwyn and J. D. Cossairt, "A study of neutron leakage through an Fe shield at an accelerator", Health Physics 51 (1986) 723-735.
- (El91) A. J. Elwyn to J. D. Cossairt, private communication (1991).
- (Gi69) W. S. Gilbert, "Shielding measurements at the CERN 25 GeV proton synchrotron", Rept. CONF-691101, USAEC 323 (1969)
- (Go71) P. J. Gollon and M. Awschalom, "Design of penetrations in hadron shields", CERN Report 71-16 Vol. 2 (1971) also published in IEEE Trans. Nucl. Sci. NS-18 (1971)741-745.
- (Go75) K. Goebel, G. R. Stevenson, J. T. Routti, and H. G. Vogt, "Evaluating dose rates due to neutron leakage through the access tunnels of the SPS", CERN Report. LABII-RA/Note/75-10 (1975).
- (IC73) International Commission on Radiological Protection, "Data for protection against ionizing radiation from external sources, supplement to ICRP Publication 15", ICRP Publication 21 (Oxford, Pergamon Press, 1973).
- (Li61) S. J. Lindenbaum, "Shielding of high energy accelerators", Ann. Rev. Nucl. Sci. 11 (1961) 213.

- (Ma67) R. E. Maerker and V. R. Cain, "AMC, a Monte-Carlo code utilizing the albedo approach for calculating neutron and capture gamma-ray distributions in rectangular concrete ducts", Rep. ORNL-3964, Oak Ridge National Laboratory, Oak Ridge, Tennessee (1967).
- (Na81) T. Nakamura and T. Kosako, "A systematic study on neutron skyshine from nuclear facilities, Part I: Monte-Carlo analysis of neutron propagation in air-over-ground environment from a monoenergetic source", Nucl. Sci. and Eng. 77 (1981) 168.
- (NC77) E. A. Burrill, Chair, J. R. Beyster, G. L. Brownell, A. B. Chilton, J. Haimson, C. J. Karzmark, W. E. Kreger, J. M. Wyckoff, *Radiation Protection Design Guidelines for 0.1-100 MeV Particle Accelerator Facilities*, National Council on Radiation Protection and Measurements (NCRP), NCRP Report 51 (1977).
- (Pa73) H. W. Patterson and R. H. Thomas, *Accelerator Health Physics*, Academic Press, New York, 1973.
- (Ra91) R. Rameika, "Labyrinths and penetration methodology-Version 1.3", Fermilab Research Division Shielding Assessment (1991), private communication.
- (Ri75) A. Rindi and R. H. Thomas, "Skyshine-a paper tiger?", Particle Accelerators 7 (1975) 23-39.
- (Ru76) P. Ruffin and C. Moore, "A study of neutron attenuation in the E-99 labyrinth", Fermilab Radiation Physics Note # 9 (1976).
- (Sc90) H. Schopper (editor), A. Fassò, K. Goebel, M. Höfert, J. Ranft, and G. Stevenson, *Landolt-Börnstein Numerical Data and Functional Relationships in Science and Technology New Series; Group I: Nuclear and Particle Physics Volume II: Shielding Against High Energy Radiation* (O. Madelung, Editor in Chief, Springer-Verlag, Berlin, Heidelberg, 1990).
- (St73) G. R. Stevenson and D. M. Squier, "An experimental study of the attenuation of radiation in tunnels penetrating the shield of an extracted beam of the 7 GeV proton synchrotron NIMROD, Health Physics 24 (1973) 87.
- (St84) G. R. Stevenson and R. H. Thomas, "A simple procedure for the estimation of neutron skyshine from proton accelerators", Health Physics 46 (1984) 115-122.
- (Te82) K. Tesch, "The attenuation of the neutron dose equivalent in a labyrinth through an accelerator shield", Particle Accelerators 12 (1982) 169-175.
- (Th88) R. H. Thomas and G. R. Stevenson, "Radiological Safety Aspects of the Operation of Proton Accelerators", Technical Report No. 283, IAEA, Vienna, 1988.

1. A 1 μA 100 MeV electron beam is incident on an "optimized bremsstrahlung" target in a shielding configuration and labyrinth like that in Fig. 4.3. Using the facts given in Chapter 1 (Swanson's Rules of Thumb, etc.) about bremsstrahlung, calculate the dose equivalent rate at the exit of a labyrinth having 2 legs. Set all distances, d_i , d_1 , and $d_2 = 3$ meters. If the goal is to get the dose equivalent rate at the exit < 1 mrem/hr, is this a sensible design? The 2 legs are $1 \times 2 \text{ meter}^2$ in cross section and, since no other information is available, use $\alpha = 10^{-2}$ as a "conservative" value. [Hint: One needs to calculate the projected diameter of the beam at the wall where the first scatter occurs. This can be done using Eq. (1.28).]
2. A 500 GeV proton beam (10^{11} protons/second) strikes a magnet 2 m from the mouth of a 3-legged labyrinth. Each of the 3 legs is 4 meters long and $1 \times 2 \text{ m}^2$ in cross section. Using Goebel's "universal" curves ("point source" for first leg and AMC calculation for legs after the first) and Rameika's source term, what is the dose equivalent rate at the exit expressed in rem/hr. Based on the results of Elwyn, how far away from the exit does the value of dH/dt fall to 10 mrem/hr. (Assume point source and "on-axis" conditions.)
3. A high energy accelerator has a section of beamline which was poorly designed. Beam losses and skimpy shielding have resulted in a region of roof 10 meters wide and 50 meters long where a neutron dose equivalent rate averaging 100 mrem/hour (averaged over the surface of the weak shield) is found. A spectrum measurement indicates the spectrum to be approximately $1/E$ with an upper end point of ≈ 500 MeV. Calculate the dose equivalent rate due to skyshine at distance $r = 50, 100, 200, 500,$ & 1000 m using both formulae presented.

This page is intentionally left blank.